REVIEW ARTICLE | FEBRUARY 05 2026

Recent progress and applications of III–V quantum dots in quantum technologies FREE

Zhikai Ma ; Shiyao Wu ; Hancong Li ; Xiqing Chen ; Kai Peng ; Chenjiang Qian ; Kuijuan Jin ; Qihuang Gong; Xiulai Xu

Appl. Phys. Rev. 13, 011313 (2026)
https://doi.org/10.1063/5.0291094

Applied Physics Reviews REVIEW pubs.aip.org/aip/are

Recent progress and applications of III–V quantum dots in quantum technologies

Cite as: Appl. Phys. Rev. **13**, 011313 (2026); doi: 10.1063/5.0291094
Submitted: 15 July 2025 · Accepted: 22 January 2026 ·
Published Online: 5 February 2026

Zhikai Ma,[1] Shiyao Wu,[2] Hancong Li,[1] Xiqing Chen,[1] Kai Peng,[3,a)] Chenjiang Qian,[4,b)] Kuijuan Jin,[4] Qihuang Gong,[1] and Xiulai Xu[1,5,c)]

AFFILIATIONS

[1]State Key Laboratory for Mesoscopic Physics and Frontiers Science Center for Nano-optoelectronics, School of Physics, Peking University, Beijing 100871, China
[2]Beijing Academy of Quantum Information Sciences, Beijing 100193, China
[3]State Key Laboratory of Semiconductor Physics and Chip Technologies, Institute of Semiconductors, Chinese Academy of Sciences, Beijing 100083, China
[4]Beijing National Laboratory for Condensed Matter Physics, Institute of Physics, Chinese Academy of Sciences, Beijing 100190, China
[5]Collaborative Innovation Center of Extreme Optics, Shanxi University, Taiyuan, Shanxi 030006, China

[a)]**Electronic mail**: pengkai@semi.ac.cn
[b)]**Electronic mail**: chenjiang.qian@iphy.ac.cn
[c)]**Author to whom correspondence should be addressed:** xlxu@pku.edu.cn

ABSTRACT

III–V quantum dots (QDs) grown by epitaxy are a typical zero-dimensional semiconductor confining electrons and holes with discrete energy levels. Charges, spins, and excitons in QDs can be used to implement qubits for quantum information processing. The radiative recombination of an exciton (electron–hole pair) in a single QD yields coherent single-photon emission. The presence of a resident carrier allows for the deterministic mapping between the stationary spin state and the flying photon polarization, enabling an efficient spin–photon interface. Moreover, QDs can be integrated into on-chip nanophotonic structures, including cavities and waveguides. Owing to these features, III–V QDs have shown great potential for the scalable quantum network. In the past two decades, substantial progress in QD growth techniques, exciton modulation methods, and nanophotonic device fabrication has led to the development of high-performance quantum photonic devices. However, several key challenges still exist, such as the growth of high-quality QDs operating at the telecom band, precise control and enhancement of cavity–QD coupling strength, and deterministic integration of QDs into photonic circuits. This review explores recent progress and applications of III–V QDs, including state-of-the-art growth techniques, advanced exciton control schemes such as resonance fluorescence, investigations of cavity quantum electrodynamics, and single-photon routing through waveguides. In the end, the prospects for realizing a QD-based quantum photonic network for practical applications are also discussed.

TABLE OF CONTENTS

I. INTRODUCTION . . . 2
II. GROWTH OF QDS AND OPTIMIZATION . . . 2
A. Growth methods . . . 3
B. Optimization of qualities . . . 4
C. Site-controlled QDs . . . 5
D. Other III–V QDs . . . 7
III. EXCITON CONTROL IN SINGLE QDS . . . 8
A. Exciton states and distinct features . . . 8
B. Exciton decay dynamics and pure dephasing . . . 11
C. Resonance fluorescence and optical coherent control . . . 12
D. External field modulation . . . 14
IV. QUANTUM LIGHT SOURCES AND QUBITS BASED ON QDS . . . 16
A. Single-photon sources . . . 16
B. Entangled photon pairs . . . 17
C. Solid-state qubits based on QDs . . . 17
V. CAVITY QUANTUM ELECTRODYNAMICS . . . 19
A. Coupling theory . . . 20
B. Photonic cavities . . . 21
C. Quantum devices and applications . . . 23
VI. ON-CHIP INTEGRATION . . . 28
A. Nanophotonic waveguides . . . 28

B. Integration technologies 29
VII. SUMMARY AND OUTLOOK 32

I. INTRODUCTION

Semiconductors with electrons and holes are the bedrock of modern information technology. The manipulation of their electronic and optical properties has been a long-standing central focus in the study of condensed matter physics. Compared to bulk semiconductors, low-dimensional semiconductors provide a platform for exploring the physics of nanosystems governed by quantum confinement, which is the basis for the interaction between single particles, such as excitons and photons, at the quantum limit. Semiconductor quantum dots (QDs) are a typical quasi-zero-dimensional optoelectronic material with a pyramid-shaped structure approximately 5 nm in height and 20 nm in width.[1] The quantum confinement effect in all three dimensions results in discrete energy levels for the electrons and holes, along with monochrome single-photon emission from the dipolar-allowed transition between them. The high luminescence efficiency of QDs has been applied to improve diverse technologies, including laser,[2,3] next-generation display,[4,5] high-resolution bioimaging,[6] and efficient photoelectric conversion.[7] Furthermore, quantized energy states and bright single-photon emission of QDs have enabled the revolutionary development of quantum information processing.[8–10]

In 1982, Arakawa and Sakaki proposed the concept of a multidimensional quantum-well laser.[11] By analyzing carriers confined in three dimensions, they showed that such a QD-like active region yields an almost temperature-independent threshold current, a result widely regarded as the first conceptual realization of a QD laser. Around the same time, early indications of three-dimensional (3D) carrier confinement in epitaxial structures were reported,[12,13] and by the 1990s, epitaxial techniques for growing QDs had been developed.[14–17] In 1983, Brus *et al.*[18] reported the chemical synthesis of colloidal QDs. Since then, different types of QDs have been developed, and the 2023 Nobel Prize in Chemistry was jointly awarded for the discovery of QD synthesis. However, although colloidal QDs have simple synthesis methods, their optoelectronic properties are limited by defects, surface traps, and interface imperfections, leading to low stability and broad emission linewidth.[19] In contrast, in 1990, Eaglesham *et al.*[14] and Guha *et al.*[15] used molecular beam epitaxy (MBE) to grow epitaxial QDs. This method gives a much lower defect density in the QDs. In particular, after decades of optimization, III–V QDs grown by epitaxy have been demonstrated with high luminescence efficiency, telecom-band emission, narrow emission linewidth, near-zero fine structure splitting (FSS), and low phonon sideband noise, where these properties establish them as near-ideal quantum emitters. The discrete energy structure of QDs supports diverse excitonic states. While the neutral exciton transition serves as a two-level system for single-photon generation, encoding quantum information in the spin of a resident carrier necessitates a multi-level configuration, typically a three-level Λ-system. The optical transitions of charged excitons provide spin-selective access to long-lived electron or hole spin states, making the QD a promising candidate for the deterministic spin–photon interface in the solid state.[20] As a result, until now, III–V QDs exhibit the best performance regarding quantum light sources among various types of quantum emitters[21] and have shown practical potential for quantum information processing.

Moreover, III–V QDs can be embedded in solid-state optical cavities, providing an ideal platform to investigate cavity quantum electrodynamics (cQED). The cavity–QD system enables devices such as Purcell-enhanced quantum light sources with high efficiency and high operation speed exciton–photon interfaces.[1] In recent years, the study of the cavity–QD system has mainly focused on the distributed Bragg reflector (DBR) cavity and the 2D slab photonic crystal (PHC) cavity.[22] The cavity has two central parameters, i.e., the quality factor (Q-factor) and the mode volume V. The Q-factor corresponds to the photon loss rate that describes the ability of the cavity to confine the photons, and V refers to the spatial size of the photon confinement. The cavity–QD system is in the weak or strong coupling regime, determined by whether the cavity–QD coupling strength g (related to V) exceeds the system decay rate (related to Q-factor and exciton lifetime) or not.[23] Cavity–QD system has currently achieved remarkable performance, including a second-order correlation function at zero time delay $[g^{(2)}(0)]$ of 0.001,[24] an indistinguishability of 0.9956,[25] and a Purcell factor of 43.[26] Manipulation and enhancement of the cavity–QD coupling remain long-standing topics in the study of cQED.

To realize scalable quantum photonic circuits, a promising approach involves integrating multiple cavity–QD systems on a single chip interconnected by low-loss photonic waveguides. These nanophotonic circuits will enable the integrated implementation of complex quantum networks,[27] supporting functionalities such as on-chip multi-channel coherent single-photon sources (SPS) and multi-photon interference. The waveguide systems, with the exploitation of slow light modes and chiral quantum optics, have been developed to achieve Purcell-enhanced and spin-momentum locked single-photon routing, laying the foundation for photon transport from QDs with high coupling efficiency.[28] However, the experimental realization of large-scale on-chip integration with multiple resonant QDs remains a challenge. The solution to this problem relies on optimizing the QD growth method toward deterministic spectral energy and spatial positions, and the external field modulation schemes also play an important role.

In this review, we provide a comprehensive overview of the latest progress and applications of the III–V QDs in quantum technologies. Section II summarizes the growth methods of III–V QDs and the optimizations for achieving low-stress, highly symmetric, and telecom-band QDs. Section III introduces the fundamental properties of excitons and the manipulation of them through multiple physical degrees of freedom, such as optical methods and external field modulation. Section IV focuses on the principle of the generation of single photons and entangled photon pairs as well as the qubit states in the QD. Section V introduces the cavity–QD system, along with the physics of cQED and applications in quantum devices. Waveguides coupled with single QDs, providing the basis of active quantum photonic network, are discussed in Sec. VI. Section VII concludes the review, discussing the challenges and emerging opportunities of III–V QDs for future development.

II. GROWTH OF QDs AND OPTIMIZATION

Fabrication methods for QDs primarily include chemical synthesis and epitaxy growth. Chemical synthesis method is a relatively cost-effective and simple approach for fabricating colloidal QDs. By manipulating the reaction temperature and duration, the size and shape of colloidal QDs can be precisely controlled. This growth method has been successfully used to produce numerous colloidal QDs based on semiconductors and metal halide perovskites, which have found wide

applications in classical optoelectronic devices (e.g., displays) and have also demonstrated their potential in non-classical light emission.[16,29,30]

In contrast, the epitaxial growth method typically utilizes bottom-up techniques in a vacuum environment to fabricate high-quality epitaxial QDs. These nanostructures have already demonstrated promising applications in various fields, such as optical fiber communication, optoelectronic circuits, and ultrahigh-efficiency solar cells, and serve as a critical platform for quantum light sources.[31]

Although the first demonstrations of antibunching involving QDs were performed using colloidal nanocrystals, and significant progress has been made in eliminating defects and surface states in these systems, quantum light sources currently rely largely on epitaxial QDs.[10,32] In Secs. II A–II D, we focus primarily on QDs grown by the epitaxial method. The main modes of epitaxial growth, the optimization of III–V semiconductor QDs, and their influence on the performance of QDs will be systematically described. This will provide a basis for discussing the physical properties of QDs and their coupling to optical cavities in the subsequent chapters.

A. Growth methods

The growth techniques for semiconductor QDs directly govern their parameters, such as size, morphology, composition, density, distribution, crystallinity, and defect states, which are critical in determining the optoelectronic properties of these nanostructures.[10] Since the 1980s, epitaxial techniques have been developed to advance from quantum wells toward stronger confinement structures (e.g., quantum wires and dots).[14–17,33,34] To the present day, the growth technology of III–V semiconductor QDs has evolved from early spontaneous growth to the current stage of precise control, promoting progress from random distribution toward a deterministic growth arrangement. Here we mainly focus on III–V semiconductor QDs (e.g., InAs, GaAs, InGaAs, InP) grown by the epitaxial growth method. The main growth technology and mode of the epitaxial method will be discussed in the following paragraphs, respectively.

MBE and metal–organic vapor phase epitaxy (MOVPE) are representative epitaxial growth technologies that rely on single-crystal substrates to achieve epitaxial growth.[35,36] MBE can precisely control the growth of single-crystal films and nanostructures at the atomic scale with a low and well-controlled growth rate.[37] The directional incidence of molecular beams on a heated substrate in an ultrahigh vacuum environment suppresses contamination during growth. Because of its accurate control of composition and structure while minimizing impurities and defects, the MBE technique is particularly well-suited for growing III–V semiconductor QDs with atomically sharp and clean interfaces and uniform sizes.[38,39] These characteristics allow MBE-grown QDs to exhibit narrow and stable emission spectra, which are ideal for applications in quantum technology.[40,41] By comparison, MOVPE utilizes a carrier gas to deliver metal–organic compounds and reactant gases to the heated substrate surface, usually operating at a higher temperature.[42] MOVPE is a highly versatile technique that can be used to fabricate a wide range of materials. Precise control of the growth process enables the strain balancing and compensation, as well as the fabrication of complex structures. Furthermore, the growth rates of the thin film and nanostructures are high, resulting in lower costs. Therefore, MOVPE is more suitable for the large-scale production of III–V semiconductor QDs. Generally, MBE and MOVPE each have their respective merits for specific applications.

Common modes of epitaxial growth are the Frank–van der Merwe (F–M) growth mode, the Volmer–Weber (V–W) growth mode, the Stranski–Krastanov (S–K) growth mode, and the droplet epitaxy (DE) growth mode, as shown in Fig. 1. The F–M growth mode

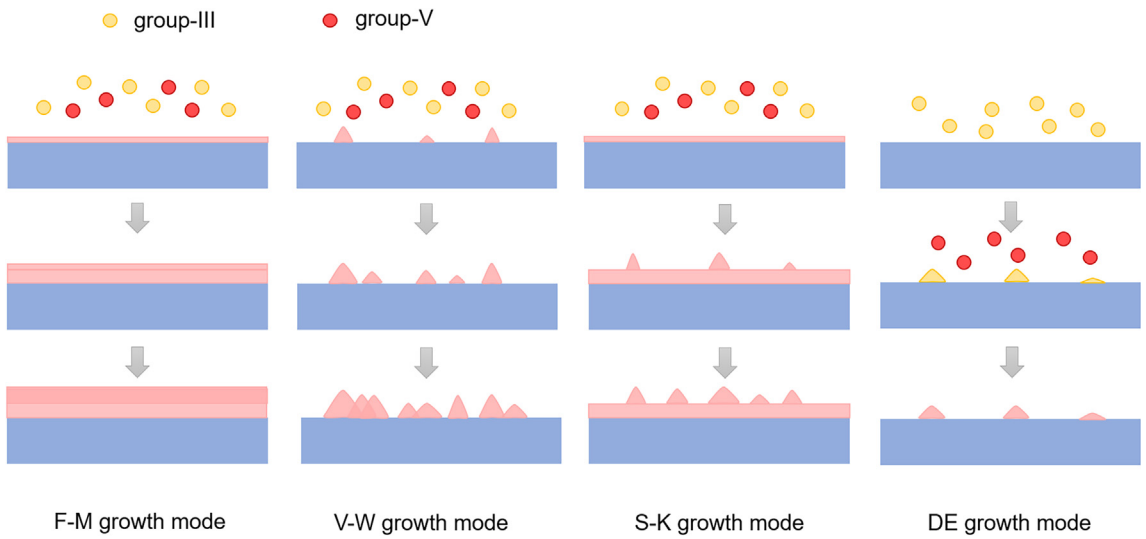

FIG. 1. Schematic illustration of four distinct modes during MBE growth. The diagrams show the sequential evolution of surface morphology under group III elements (yellow circles) and group V elements (red circles) deposition. (a) Frank–van der Merwe (F–M) growth mode exhibits layer-by-layer growth with smooth surface progression (do not directly grow QDs). (b) Volmer–Weber (V–W) growth mode demonstrates three-dimensional island formation from initial deposition stages. (c) Stranski–Krastanov (S–K) growth mode shows initial wetting layer (WL) formation followed by three-dimensional island nucleation. (d) Droplet epitaxy (DE) growth mode illustrates metal droplet formation followed by crystallization into QD structures upon group V supply. The blue substrate and pink epitaxial layers represent the semiconductor heterostructure, with arrows indicating the temporal progression of each growth mechanism.

relies on a stronger bonding force between the deposited atoms and the substrate to form layered structures, which is used mainly in the initial deposition of the wetting layer (WL) and buffer layers.[43–45] The V–W mode, based on stronger inter-atomic bonding, prefers to form island structures that eventually produce a non-uniform thin film.[45] The V–W growth mode features a simple preparation process but yields QDs with poor quality, suitable for broad spectral applications.[45,46] In the S–K growth mode, an epitaxial layer referred to as a WL is first formed, and the lattice mismatch between it and the substrate induces elastic strain energy.[44,47] As the WL approaches a critical thickness, typically a few monolayers,[48] the accumulated strain energy exceeds the energy barrier for three-dimensional island nucleation, prompting spontaneous formation of self-assembled three-dimensional islands that serve as QDs. This strain-driven process effectively relaxes the elastic energy while maintaining epitaxial growth at the interface, resulting in QDs with suitable density, well-defined size distributions, and high optical performance. In addition, the WL plays a crucial role in facilitating carrier injection and extraction,[49] making QDs grown by the S–K growth mode particularly suitable for optoelectronic and quantum technology applications. However, while the S–K mode relies on strain to form QD, strain-free QDs are highly demanded to suppress FSS, as discussed later in Sec. IV. In contrast, the DE growth mode, which can be traced back to the early 1990s, involves the formation and crystallization of metallic droplets to form QDs rather than relying on lattice mismatch, thereby greatly suppressing the strain in QDs.[50–53] In the DE growth mode, the group III and V fluxes are separated, leading to the initial formation of group III droplets. These droplets subsequently crystallize in the presence of group V flux, resulting in the formation of QDs.[54,55] As group V elements are introduced, these droplets react to form semiconductor QDs. The DE growth mode enables precise control of the geometric parameters, density, and composition distribution of QDs, allowing the fabrication of QDs with low density, high symmetry, and almost no FSS, illustrating its significance in applications requiring highly symmetric QD structures.[8]

B. Optimization of qualities

Key properties of QDs, such as density, emission wavelength, fluorescence linewidth, and FSS, are crucial for enhancing the performance of QD-based optoelectronic devices and advancing the practical deployment of QDs in quantum communication and quantum computing. Various growth regulation strategies have been developed to optimize these key properties of QDs, mainly including the surrounding environment, structural symmetry, chemical composition, and strain distribution.

Linewidth: The spectral linewidth of a QD is affected by the surrounding environment, including the surface states at the top and the WL states at the bottom. The surface states significantly broaden the linewidth of QDs, especially when QDs are less than 40 nm from the surface.[82] Passivation technologies can mitigate this effect by eliminating surface dangling bonds, reducing the surface state density, and suppressing their influence on carriers in QDs, thereby improving the optical and electrical properties of QDs.[83,84] In 2025, Zhao *et al.* demonstrated a 46.77 % reduction in resonant fluorescence (RF) linewidth through a synergistic approach combining surface passivation technology with a distributed Bragg reflector (DBR) and circular Bragg grating (CBG) structure, offering a reference for passivation techniques in thin-film quantum devices.[85] In addition, the WL state exists at the bottom of QDs grown by the S–K method, resulting in continuous energy levels of WL states proximate to QD excitonic levels. This induces multi-electronic states suppression and spectral linewidth broadening via state hybridization, exciton scattering, decoherence, Rabi oscillation damping, and the Auger effect.[86–90] These issues can be radically altered by modifying the S–K growth mode: overgrowing QDs with a monolayer of AlAs.[91,92] By introducing AlAs, the energy level of the WL electronic state is shifted above the exciton energy level, enabling multi-electron states while achieving a narrow spectral linewidth.[92]

Fine structure splitting: The structural asymmetry and inhomogeneous strain of QDs can lead to an increase in in-plane anisotropies and the exchange interaction between electrons and holes. This exchange interaction generates an energy splitting in the neutral exciton state, i.e., FSS.[93,94] Eliminating FSS is a critical requirement for on-demand photon-pair sources with near-unity degrees of entanglement,[95] which will be discussed in Sec. IV B. In comparison with the S–K growth mode, QDs prepared by the DE growth mode, especially high-temperature DE (HT-DE) and local DE, exhibit a smaller FSS due to the low strain growth environment.[59,60,96] The high-temperature environment in HT-DE facilitates the uniform relaxation of strain accumulated during growth and enhances atomic migration capabilities. This allows for more ordered atomic arrangements during QD growth and a notable reduction in FSS (4.5 μeV).[60,97] The local DE growth mode, which involves filling nanoholes, is another approach to forming highly symmetric QDs with low strain, which further reduces the FSS to 2.5 μeV.[96]

Emission wavelength: The intrinsic band structure of the QD material, along with its size and shape, influences the emission wavelength of QDs, thereby determining the practical applications of QDs. For example, GaN and InGaN QDs are well suited for the ultraviolet–visible emission wavelength range of approximately 240–490 nm, largely due to their wide bandgap structure, as shown in Table I.[56–58] Typically, the emission wavelength of GaAs QDs grown via epitaxial deposition of an AlGaAs buffer layer on a GaAs substrate covers the visible and near-infrared (NIR) spectral ranges.[59–61,98,99] Similarly, InAs QDs directly grown on a GaAs substrate naturally emit in the NIR spectral region.[62,63,100]

In addition, QDs with emission in the telecom band are highly demanded for low-loss integration with fiber or on-chip waveguides.[103] The commonly used telecom bands are primarily the Original band (O-band) and the Conventional band (C-band). The O-band is typically defined as spanning 1260–1360 nm, while the C-band covers 1530–1565 nm, which corresponds to a larger QD size compared to that used for emission in the near-infrared bands. Several approaches have been investigated to enable QDs with emission directly within the O- and C-bands, including the application of a strain-reducing capping layer (SRL),[65,66] the design and growth of metamorphic buffer layers (MBL),[68–70,104–107] and the modification of QD and substrate materials.[62,74–77,80,81,108–110] These approaches allow for the reduction of the mismatch between QDs and the growth substrate to form larger QDs, and achieve a suitable bandgap of the QD material for exciton emission covering the telecom band. For instance, growing InAs/GaAs and InGaAs/GaAs QDs with an InGaAs MBL enable the emission wavelength to shift to 1100–1600 nm.[68–70,104–106] Moreover, by tuning the indium content within the MBL, the strain

TABLE I. Comparison of QD parameters for different growth methods. HT-DE: high-temperature DE; SRL: strain-reducing capping layer; MBL: metamorphic buffer layers.

QD material	Wavelength range (nm)	Growth method	Linewidth (μeV)	FSS (μeV)	Dot density (cm^{-2})	Specialized techniques
GaN/AlN[56]	244	MBE (SK)	···	1.4×10^4(300 K)	1.0×10^{10}	···
GaN/AlGaN[57]	330–350	MOVPE (SK)	87	1100	···	···
InGaN/GaN[58]	420–480	MOVPE (DE)	2200	···	3.0×10^8	···
GaAs/AlGaAs[59,60]	670–780	MBE (DE)	9	4.5	8.0×10^8	HT-DE
GaAs/AlGaAs[61]	740–800	MBE (DE)	<20	3.6 (1.7)	···	Local DE
InAs/GaAs[62]	900	MBE (DE)	···	31	···	···
InAs/GaAs[63]	918–935	MBE (SK)	···	39	2.0×10^7	···
InGaAs/GaAs[64]	950	MBE (SK)	30	30.5 (1)	1.0×10^9	Si carrier
InAs/GaAs[65]	1300	MBE (SK)	···	···	4.0×10^9	SRL
InGaAs/GaAs[66]	1220–1380	MOVPE (SK)	66	···	4.6×10^6	SRL
InAs/GaAs[67]	1300	MBE (DE)	250	16	1.0×10^7	MBL
InAs/GaAs[68]	1550	MOVPE (SK)	···	<10	···	MBL
InAs/GaAs[69,70]	1400–1600	MBE (SK)	270	<25	1.0×10^9	MBL
InGaAsP/InP[71]	1250–1350	MOVPE (SK)	···	···	1×10^9	···
InAs/InP[72]	1277	MOVPE (SK)	···	···	1.8×10^{10}	Double-cap
InAs/InP[73]	1300–1550	MOVPE (SK)	200	···	1.8×10^{10}	Double-cap
InAs/InP[74]	1200–1700	MOVPE (SK)	700	44	$< 1.0 \times 10^9$	···
InAs/InP[75]	1500–1700	MBE (SK)	···	···	5.0×10^{10}	InAlGaAs cap
InAs/InP[76]	1550	MBE (SK)	35	3.9 (1.8)	2.0×10^9	···
InAs/InP[62]	1550	MOVPE (DE)	···	29	···	···
InAs/InP[77]	1550	MOVPE (DE)	140	···	···	···
InAs/InP[78]	1530	MOVPE (SK)	119 (7)	88 (2)	2.8×10^9	Si carrier
InAs/InP quantum dashes[79]	1526	MBE (SK)	220	···	10^9	···
GaSb/AlGaSb[80]	1470	MBE (DE)	···	···	···	Local DE
GaSb/AlGaSb[81]	1470	MBE (DE)	55	12	2.6×10^7	···

environment and the indium composition of the QDs can be further regulated, allowing precise control over the emission wavelength of the QDs in the telecom band.[107]

Altering the QD and substrate material offers another approach for wavelength regulation. For example, InAs/InP material systems naturally support emission in the telecom C-band,[62,74–78,108,109,111] as shown in Table I. O-band emission can also be achieved by intentionally reducing the QD size.[71–73,112,113] Driven by surface lattice anisotropy, the MBE growth of InAs/InP material systems tends to yield elongated quantum dashes, which typically exhibit high density.[79,114,115] GaSb-based materials possess suitable bandgaps, enabling access to technically significant telecommunication wavelengths and even extending into the mid-infrared region.[80,81,110] The GaSb material is also compatible with the integration of silicon photonics. It is important to note that the linewidth of QDs is influenced by the excitation method. Therefore, the data presented in Table I should be considered for reference only, and absolute values should not be directly compared to assess the performance of individual QDs.

Density: The density of QDs, as an important characteristic, plays a pivotal role in determining their optical performance. The density of QDs modulates the coupling between QDs, thereby regulating the non-radiative loss process. This not only impacts the carrier recombination efficiency of QD ensembles but also affects the recombination efficiency of individual QDs and their single-photon purity. Therefore, controlling the density of QDs is crucial for optimizing the performance of QD-based optoelectronic devices. Commonly adopted approaches for density control usually involve optimizing the growth process, such as precisely regulating the growth rate,[63,116] indium content,[117] and temperature.[118] Additionally, the utilization of a patterned deposition layer (PDL) is a new method that can induce changes in surface roughness, in turn influencing the nucleation probability of QDs and enabling density modulation.[101] As demonstrated in Figs. 2(a)–2(c), this approach has successfully achieved a density modulation ranging from 1 to 10 μm^{-2} across the entire wafer surface. In addition, this approach is effective for different semiconductor material systems, including GaAs, AlAs, and AlGaAs, which offers great potential for large-scale integration. Another approach to density regulation is to use a machine learning (ML)-controlled MBE growth system.[102] This method employs real-time reflection high-energy electron diffraction (RHEED) monitoring to accurately control the substrate temperature and utilizes an automatic feedback mechanism for precise adjustment of QD density, as illustrated in Figs. 2(d) and 2(e).

C. Site-controlled QDs

The deterministic site-control of QDs is critical for QD-based optoelectronic devices and quantum technologies. However, due to strain-driven spontaneous nucleation of the S–K growth mode and the

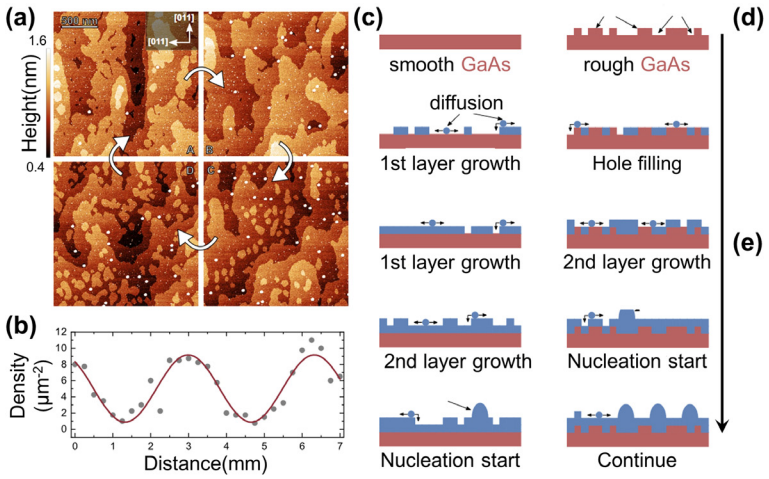

FIG. 2. New approaches for QD density control during MBE growth. (a)–(c) Improvement by growing QDs on rough surface. (a) AFM images of surface QDs along the pattern defining layer (PDL) GaAs gradient direction. (b) Quantitative analysis of QD densities extracted from AFM measurements along the PDL direction, with a sinusoidal function (red line) fitted to experimental data points (gray dots). (c) Schematic illustration of InAs QD formation mechanisms comparing smooth vs rough GaAs surface (red). The diagrams show progressive InAs layer development (blue) with increasing deposition, where adatom diffusion (blue dots) occurs on the surface and QD nucleation (blue domes) initiates earlier on rough surfaces compared to smooth surfaces due to enhanced nucleation sites. Reproduced from Bart *et al.*, Nat. Commun. **13**, 1633 (2022); licensed under a Creative Commons Attribution (CC BY) license.[101] (d) and (e) Machine learning (ML)-assisted growth of QDs. (d) Experimental setup for machine learning-controlled MBE growth system, featuring real-time RHEED monitoring, substrate temperature control, and automated feedback mechanisms for precise QD density regulation. (e) Demonstration of ML-assisted growth targeting low QD density, showing substrate temperature profile during the growth process (upper panel) and corresponding evolution through RHEED imaging: frame 1 captured at the 200th frame after growth initiation, frame 2 before QD formation, frame 3 after QD nucleation, and frame 4 showing the final AFM characterization of the resulting low-density QD distribution. Reproduced from Shen *et al.*, Nat. Commun. **15**, 2724 (2024); licensed under a Creative Commons Attribution (CC BY) license.[102]

random formation of metal droplets of DE growth mode, the traditional epitaxial growth technique usually results in a random spatial distribution of QDs. Conventional QD positioning technologies primarily rely on lithography methods to define nanoscale regions as exclusive nucleation sites prior to QD growth, e.g., using nanohole arrays or inverted pyramids as nucleation centers for localized QD growth.[119,125–131] Figure 3(a) shows the schematic sample structure and the self-assembled GaAs nanohole formed by $AsBr_3$ etching,[119] and the GaAs QDs fill the nanohole to form QDs. Although these approaches enable QD control and spatial alignment of single QDs for device integration, they require substrate pretreatment before QD growth, typically introducing defects and interface states that enhance non-radiative recombination and compromise the optical quality of the grown QDs.[127,128]

The integration of direct laser interference patterning (DLIP) combined with MBE presents an alternative paradigm for site-controlled QD growth.[120,121,132,133] Using *in situ* DLIP, periodic nano islands on semiconductor surfaces are fabricated, eliminating the need for complex lithographic and etching procedures that typically introduce contaminants and defects.[120] A representative process schematic for QD synthesis through the DLIP-MBE hybrid technology is illustrated in Fig. 3(b). QDs produced by this methodology exhibit precise spatial ordering with tunable periodicity at 205–300 nm, as shown in the right panel of Fig. 3(b), providing high-quality building blocks for quantum photonics and nanodevices.[121]

Another promising technical platform for achieving site-controlled QDs in planar sample geometries is based on the buried stressor method.[122,137–143] The buried stressor generates a local strain field to allow the deterministic nucleation of QDs in the tensile strain extreme region (directly above the aperture) on the surface, allowing the number of site-controlled QDs to be precisely regulated by the diameter of the aperture.[139,141] The growth surface is completely separated from the stressor, ensuring the high optical quality of local QDs, such as high single-photon purity and indistinguishability.[138,140] Furthermore, this technology allows the fabrication of photonic cavity self-aligned to the number and site-controlled QDs, as shown in Fig. 3(c), through which high-intensity QD light sources can be realized.[122,137]

Substrate-encoded size-reducing epitaxy (SESRE), which allows the fabrication of three-dimensional confined nanostructures through precise substrate patterning, is another approach of growth method to achieving a site-controlled QD array.[123,124,144] The process involves creating ordered nanomesa arrays on GaAs (001) substrates via electron-beam lithography and wet etching, with mesa dimensions typically ranging from 50 to 600 nm laterally and 180 to 565 nm in depth.[124,144] The [100]-oriented mesa edges induce surface stress gradients that drive the migration of adatoms (Ga/In) from the sidewalls to the top of the mesa, facilitating the reduction of the lateral size during epitaxy, as illustrated in the top panel of Fig. 3(d). As the mesas shrink to the nanoscale, QDs nucleate exclusively at the mesa tops, evident in the red box of the top panel and the white arrow of the left bottom panel shown in Fig. 3(d). By designing the initial nano-mesa array, spatially ordered QD arrays are realized,[123,124] with each mesa hosting a single QD, as shown in the right panel of Fig. 3(d). SESRE-grown QDs exhibit exceptional spectral uniformity (standard deviation <8 nm) and single-photon emission purity >98% [$g^{(2)}(0) < 0.01$], which provides a great platform for quantum technologies.[124]

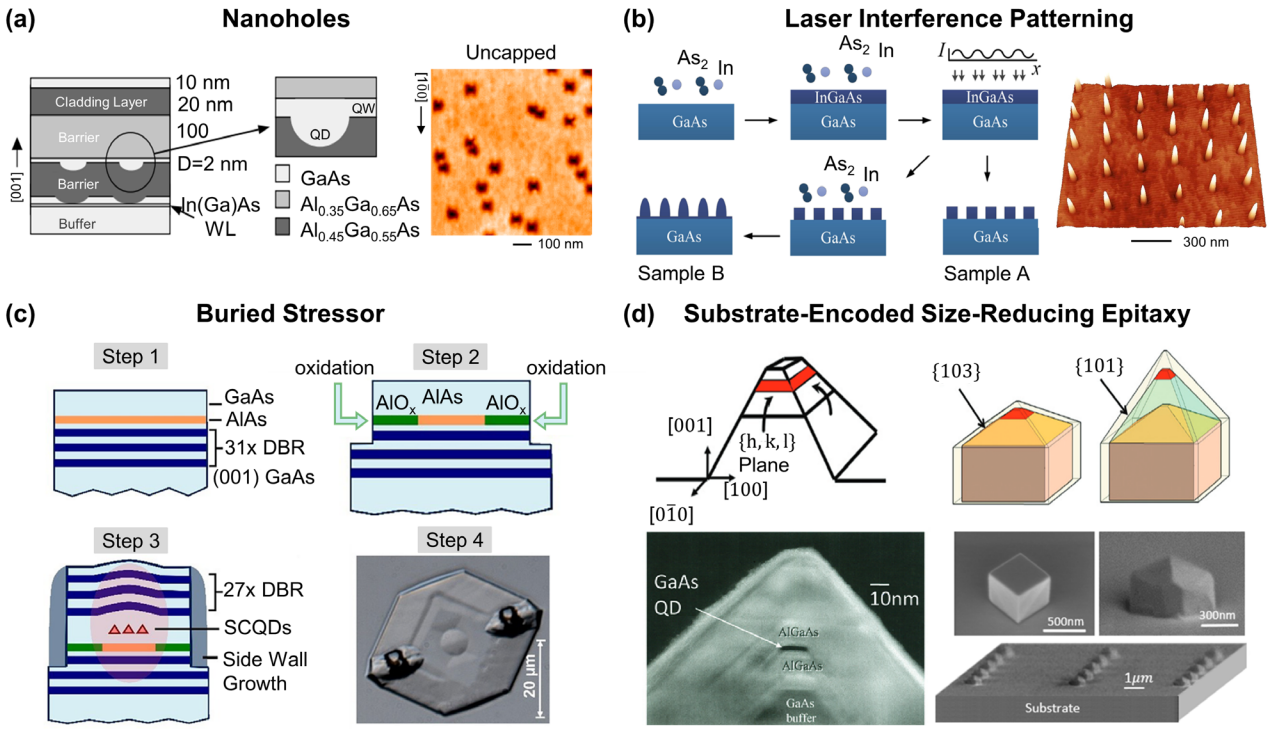

FIG. 3. Approaches for the site-controlled growth of QDs. (a) *In situ* etching method by introducing $AsBr_3$ during MBE. Left panel: The schematic sample structure and magnification of the active layer and nanohole. Right panel: AFM images of etched GaAs nanoholes. Reproduced from Astelli *et al.*, Phys. Rev. Lett. **92**, 166104 (2004); licensed under a Creative Commons Attribution (CC BY) license.[119] (b) *In situ* DLIP growth method utilizing spatially modulated laser irradiation to control QD nucleation sites on semiconductor substrates. Reproduced from Zhang *et al.*, Appl. Phys. Lett. **112**, 153108 (2018), with the permission of AIP Publishing.[120] Left panel: Diagram of the experimental procedure. Right panel: AFM image of a regular array of single GaAs/AlGaAs QDs grown by DLIP. Reproduced from Wang *et al.*, Nanophotonics **12**, 1469–1479 (2023); licensed under a Creative Commons Attribution (CC BY) license.[121] (c) Buried stressor growth method with the fabrication of photonic cavity self-aligned to site-controlled QDs. Step 1: Growth of bottom cavity and oxidation template. Step 2: Patterning and lateral wet-oxidation to enable surface strain modulation. Step 3: Overgrowth with strain-induced site-controlled QDs (SCQDs) and curved upper cavity. Step 4: A photonic cavity is formed and self-aligned to the SCQDs as shown by optical microscope image. Reproduced from Shih *et al.*, Laser Photonics Rev. **18**, 2301242 (2024); licensed under a Creative Commons Attribution (CC BY) license.[122] (d) Schematic diagram of SESRE growth method. Top panel: Schematic of a (001) top square mesa with ⟨100⟩ edge orientation and h, k, l sidewalls. The arrows indicate atom migration from the sidewalls to the top leading to size-reducing epitaxy, and the red box shows the QDs. Bottom panel: Cross-sectional TEM images of a SESRE grown AlGaAs/GaAs/AlGaAs QDs (left); Reproduced from Zhang *et al.*, J. Appl. Phys. **120**, 243103 (2016), with the permission of AIP Publishing.[123] SEM images of mesa top single QDs grown on mesas (right). Reproduced from Zhang *et al.*, APL Photonics **5**, 116106 (2020); licensed under a Creative Commons Attribution (CC BY) license.[124]

D. Other III-V QDs

Rapid development in quantum information, high-speed optical communication, and highly sensitive detection technologies makes research on QDs based on III–V materials other than InGaAs of great significance. III-nitride QDs, with their wide bandgap, present a promising system for the realization of single-photon sources in the ultraviolet and visible ranges. GaN QDs [Fig. 4(a)], with a bandgap of 3.4 eV, demonstrate a high PL efficiency in the ultraviolet-blue spectral range and non-classical light emission.[56,58] Through suitable variation of the In/Ga ratio in InGaN QDs, the emission wavelength of both single-photon sources and entangled photon sources can be further tuned to cover the visible range [Fig. 4(b)]. GaSb QDs grown on GaAs substrate via MBE exhibit a uniform size distribution with a diameter of approximately 50 nm,[151] as shown in Figs. 4(c) and 4(d). With a 0.72-eV bandgap, GaSb QDs can emit photons directly in the telecom S-band and exhibit a drop of correlated count-events at zero delay time, making them ideal single-photon sources for telecom wavelengths.[81,110] InSb QDs also provide another alternative system with emission in the near-infrared and mid-infrared regions due to their narrow bandgap.[135,152–154] InSb QDs grown on (100)-oriented GaAs substrates by MBE [Fig. 4(e)] exhibit rectangular morphology elongated along the (100) direction, with evident anisotropy arising from the 14.6% lattice mismatch between InSb and GaAs and the weak InSb binding energy.[135] In contrast, van der Waals (vdW) epitaxy of InSb QDs on 2D materials (e.g., hBN and MoS_2) breaks the limitations of lattice matching [Fig. 4(f)], allowing precise control over size uniformity (±5%) and density (10^8–10^{12} cm^{-2}) of InSb QDs.[136] These as-grown InSb/MoS_2 QDs demonstrate a broadened near-infrared photoresponse due to the efficient charge transfer channels at vdW interfaces.

Unlike planar growth, nanowires (NWs) enable efficient relaxation of strain induced by lattice mismatch, thus allowing the growth of a richer set of material combinations and the more symmetric structure of QDs, which results in a lower FSS of the exciton state.[155] The

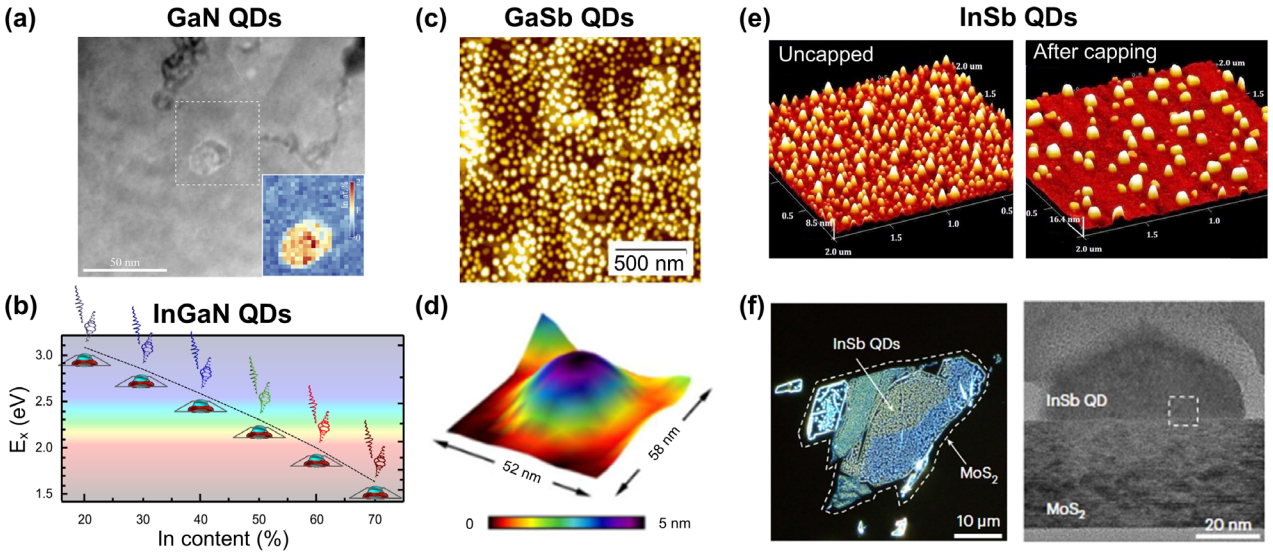

FIG. 4. QDs based on III–V materials other than $In_xGa_{1-x}As$. (a) STEM image of a GaN QD. Reproduced from Holmes *et al.*, APL Mater. **9**, 061106 (2021); licensed under a Creative Commons Attribution (CC BY) license.[58] (b) Exciton emission energy plotted as a function of indium composition of InGaN QDs. Reproduced from Tomic *et al.*, ACS Photonics **2**, 958–963 (2015); licensed under a Creative Commons Attribution (CC BY) license.[134] (c)-(d) GaSb QDs. Reproduced from Phienlumlert *et al.*, Phys. Status Solidi A **216**, 1800499 (2019); licensed under a Creative Commons Attribution (CC BY) license.[110] (c) AFM image of GaSb QDs with a growth rate of 0.18 MLs^{-1}, with magnified 3D perspective AFM images of a GaSb QD showing in (d). (e) SPM images of InSb QDs grown on (100) GaAs substrate, the left panel shows the morphology and density of uncapped InSb QDs, and right panel shows those of InSb QDs after capping. Reproduced from Ahia *et al.*, AIP Adv. **8**, 075004 (2018); licensed under a Creative Commons Attribution (CC BY) license.[135] (f) InSb QDs grown on Van der Waals (VdW) surface. Left panel A dark-field optical image of InSb QDs on MoS_2, where black represents flatness and the colors indicate bulges. Right panel shows a cross-sectional TEM image of an InSb QD on MoS_2. Reproduced with permission from Nature Syn. **8**, 1176–1183 (2024). Copyright 2024, Springer Nature.[136]

one-dimensional waveguide structure of NWs exhibits efficient light field manipulation and precise site-control.[146,147,156] The carrier confinement of QDs in NWs endows them with rich exciton states,[146,157] making them ideal platforms for quantum communication and computing.[155] For example, a site-controlled GaN QD embedded in a GaN/AlGaN core/shell NW, as shown in Fig. 5(a), demonstrates single-photon emission with a short wavelength (~280 nm) at room temperature, due to its wide bandgap, strong exciton binding energy, and tailored photonic NW structure.[145,158] Furthermore, InAsP QDs grown in InP NWs fabricated via two-step growth also show an order array, as shown in the left panel of Fig. 5(b). These as-grown InAsP QDs in NWs exhibit bright and clean emission in the telecom band with a linewidth of 30 μeV and single-photon purity $g^{(2)}(0) = 0.02$.[146,147] Moreover, with an appropriately designed photonic NW, the emission wavelength of InAsP QDs can be tailored in the range of 880–1550 nm, as shown in the right panel of Fig. 5(b).[147] GaAs QDs in GaAsP NWs fabricated through self-catalyzed vapor–liquid–solid growth and surface engineering show a width of ~30 nm and a height of 15 nm, as shown in Fig. 5(c). They can emit red light at 677 nm with high polarization (~82.5 %) and demonstrate photon antibunching up to 160 K, suggesting a potential solution for high-temperature applications.[148] The QDs formed at the zinc-blend/wurtzite phase interface in NWs are termed crystal phase QDs [Fig. 5(d)], which enable three-dimensional carrier confinement via the type-II band offset, allowing multiple exciton formation.[150,159] Exciton emission in such crystal phase QDs demonstrates autocorrelation for excitons and biexcitons and cross-correlation between them, illustrating the potential of crystal phase QDs in NWs for applications in quantum technologies.[150]

III. EXCITON CONTROL IN SINGLE QDs

Understanding the fundamental properties and coherence of excitons in single QDs is necessary for the application of solid-state quantum photonic technologies. Exciton coherence directly impacts the quality of single-photon emission, where both the excitation schemes and dephasing mechanisms play critical roles. This chapter provides a comprehensive overview of exciton state composition, typical excitation methods, decay and dephasing dynamics, and RF techniques. To further achieve tunable coupling with optical nanostructures and scalable quantum applications, we also discuss external field modulation strategies that offer versatile tools for tailoring QD emission properties and exciton behavior. These foundational insights support a coherent control framework for the deterministic preparation and active tuning of QDs at the single-particle level.

A. Exciton states and distinct features

An exciton is a bound electron–hole (e–h) pair formed via Coulomb attraction. While excitons in bulk semiconductors have low binding energies and large Bohr radii, QDs impose strong spatial confinement, localizing carriers and producing discrete energy levels through the quantum confinement effect in both the conduction and valence bands. Represented by InAs/GaAs QDs with a flat in-plane profile and a smaller dimension along the growth axis, their

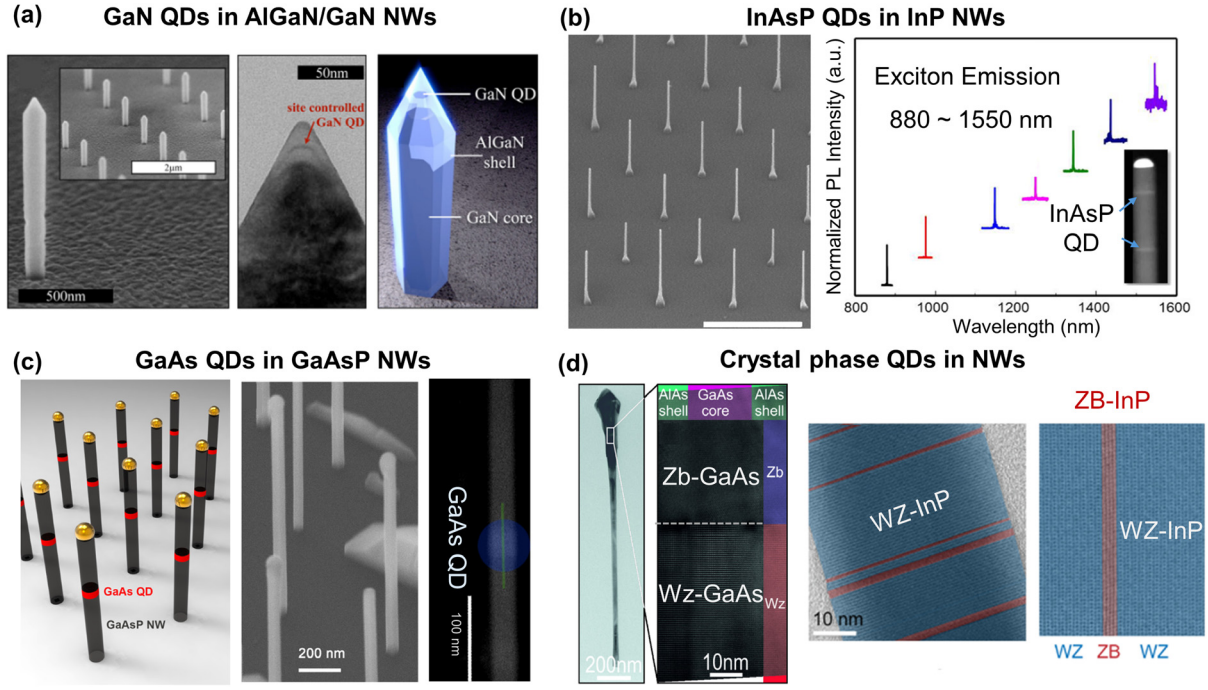

FIG. 5. QDs grown in NWs. (a) GaN QDs in AlGaN/GaN core/shell NWs. Left panel shows the SEM image of a single NW grown on patterned SiO_2 substrate by selective area MOCVD with an inset showing an arrow of NWs separated by 2 μm. Center panel shows the TEM image of a single QD near the tip of a single NW. Right panel shows the schematic of a NW containing a single QD. Reproduced with permission from Nano Lett. **14**, 982–986 (2014). Copyright 2014 American Chemical Society.[145] (b) InAsP QDs in InP NWs. Left panel shows the SEM image of an array of NW cores with scale bar indicating 1 μm. Reproduced with permission from Nano Lett. **12**, 5919–5923 (2012). Copyright 2012, American Chemical Society.[146] Right panel shows the normalized PL spectra of single InAsP/InP NW quantum-dot emitters in tailored photonic waveguides, with bottom inset showing the TEM image of a double-dot nanowire core with an 18 nm diameter. Reproduced with permission from Nano Lett. **18**, 3047–3052 (2018). Copyright 2018, American Chemical Society.[147] (c) GaAs QDs in GaAsP NWs. Left panel shows schematic of the self-catalyzed GaAsP/GaAs NWQDs grown on Si(111) substrates, with center and right panel illustrating SEM and low magnification TEM image of a GaAs QD embedded in a GaAsP NW with the scale bar of 200 and 100 nm, respectively. Reproduced with permission from ACS Nano **13**, 13492–13500 (2019). Copyright 2019, American Chemical Society.[148] (d) Crystal phase QDs in NWs. Left panel shows the bright field TEM image of the NW (left) and high resolution TEM image of the WZ–ZB GaAs interface (right). Reproduced from Geijselaers *et al.*, Appl. Phys. Lett. **119**, 263102 (2021); licensed under a Creative Commons Attribution (CC BY) license.[149] Right panel shows the EM of InP NWs showing short segments of ZB (red) in a WZ (blue) NW (left), and a high-resolution TEM image of the zinc blende segment in the otherwise wurtzite lattice (right). Reproduced with permission from Nano Lett. **16**, 1081–1085 (2016). Copyright 2016, American Chemical Society.[150]

heterostructure potentials enable efficient optical excitation and exciton formation. It is noteworthy that spin–orbit coupling, together with strain, lifts the degeneracy of the valence band, resulting in three bands. The heavy-hole band lies at the top of the valence band, followed by the light-hole band and a split-off band. The e–h pair wavefunction picture under Hartree–Fock approximation, which assumes separable electron and hole wavefunctions, is valid in relatively symmetric systems. While light-hole heavy-hole band mixing cannot be neglected in structures exhibiting substantial strain or geometric anisotropy.[162–165] Instead of flat QDs, elongated QDs along the growth axis can host light-hole states at the top of the valence band[166,167] where the light-hole states carry spin $\pm 1/2$.

For the widely investigated QDs with a much larger lateral than vertical size, excitonic properties are typically described by a band model consisting of the conduction band and the heavy-hole valence band. In this picture, exciton formation is dominated by the heavy-hole states with spin $\pm 3/2$, which dictate the optical selection rules. Only considering the ground energy levels first, various excitonic species can form, including the neutral exciton (X^0), trion (X^-/X^+), and biexciton (XX^0), each distinguished by their electron and hole composition and spin configuration, as illustrated in Fig. 6(a). For example, the bright state X^0 with spin configuration $|\uparrow\Downarrow\rangle$ or $|\downarrow\Uparrow\rangle$ are dipolar-allowed due to optical selection rules, corresponding to a total angular momentum projection of ± 1. In contrast, the dark states $|\uparrow\Uparrow\rangle$ or $|\downarrow\Downarrow\rangle$ possess a total spin of ± 2, and their radiative recombination is forbidden. A trion is a charged exciton state, formed by an e–h pair with an additional electron or hole, while a biexciton consists of two e–h pairs. The existence of biexciton introduces additional possibilities for the study of exciton transitions. For the self-assembled InAs/GaAs QD grown along the [001] direction, structural asymmetry in the growth plane induces anisotropic e–h exchange interaction, giving rise to the FSS of the X^0 exciton. In an ideal symmetric QD, the bright exciton spin states $|\uparrow\Downarrow\rangle$ and $|\downarrow\Uparrow\rangle$ are degenerate and emit circularly polarized photons. However, the structure asymmetries lift this degeneracy, resulting in linearly polarized eigenstates: $|X_H\rangle = \frac{1}{\sqrt{2}}(|\uparrow\Downarrow\rangle + |\downarrow\Uparrow\rangle)$, $|X_V\rangle = \frac{1}{\sqrt{2}}(|\uparrow\Downarrow\rangle - |\downarrow\Uparrow\rangle)$, where H and V denote orthogonal linear polarizations with respect to crystallographic axes [110]/[1$\bar{1}$0]. The FSS leads to two bright exciton states split by an energy δ_{FSS}, typically

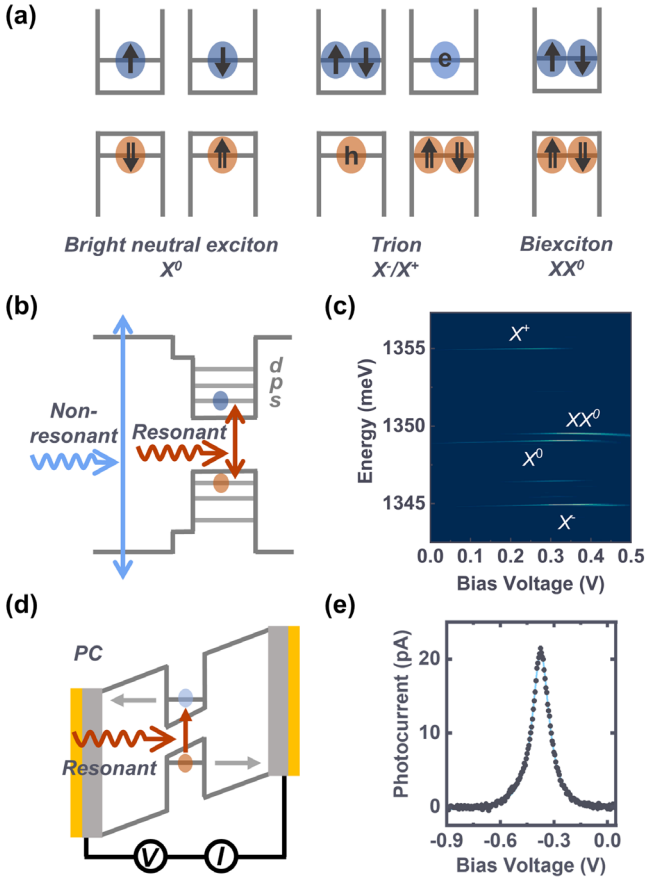

FIG. 6. Overview of exciton states and typical excitation and detection schemes for single QDs. (a) Energy-level configurations of various exciton complexes in a QD, including the bright neutral exciton (X^0), negatively and positively charged trions (X^-/X^+), and the biexciton (XX^0). (b) Schematic of non-resonant and resonant excitation pathways: non-resonant excitation populates the bulk bands, while resonant excitation directly addresses the s-shell exciton levels. (c) PL spectral map under non-resonant excitation as a function of bias voltage, showing multiple excitonic transitions including X^0, X^-, X^+, and XX^0. Reproduced from Peng *et al.*, Phys. Rev. Appl. **11**, 024015 (2019); licensed under a Creative Commons Attribution (CC BY) license.[160] (d) Schematic of PC detection under resonant excitation, where photo-excited carriers tunnel out of the QD and are subsequently collected. (e) PC spectrum of a single exciton resonance as a function of bias voltage, showing a sharp peak that indicates high-resolution resonant absorption. Reproduced from Peng *et al.*, Appl. Phys. Lett. **114**, 091109 (2019), with the permission of AIP Publishing.[161]

ranging from several tens to hundreds of μeV,[62,93,94,168,169] where the FSS can be measured through polarization and energy discrepancy of the neutral excitons. Consequently, the XX^0 state exhibits two distinct radiative decay paths due to the FSS splitting of the intermediate X^0 states.

The complete energy levels in a QD consist of a ground state (*s*-shell) and a series of excited states (e.g., *p*-shell), analogous to atomic orbitals, with typical inter-level spacings on the order of tens of meV, as depicted in Fig. 6(b). Common optical excitation schemes distinguished by different excitation energies include: (i) non-resonant (above-band) excitation into the bulk material or the WL, where the excited carrier will relax into the ground excitonic state in the QD,[170] which is convenient for QD characterization due to straightforward laser rejection via spectral filtering. (ii) Quasi-resonant excitation, in which the laser targets an excited state (e.g., the *p*-shell exciton), reducing relaxation processes compared to non-resonant excitation.[171,172] (iii) Resonant excitation, where the laser energy matches the exciton transition precisely, enabling the study of RF (further discussed in Sec. III C). However, isolating the RF signal from the residual laser background raises a significant experimental challenge. The photon emission of exciton could occur during the whole excitation process due to the re-excitation. While all continuous-wave (cw) excitation methods tend to increase the multi-photon component in photoluminescence (PL) emission, pulsed excitation naturally suppresses it, with the effect further influenced by pulse duration.

We take an example of a bias-controlled QD to illustrate different exciton complex configurations. Figure 6(c) shows a typical PL spectrum pumped non-resonantly from a single QD embedded in a n–i-Schottky device.[160] Each emission peak corresponds to the recombination transition of a certain excitonic state.[173] On one hand, applying the electric field allows for precise tuning of the exciton transition energy through the quantum-confined Stark effect. On the other hand, the bias voltage tunes the electrostatic environment, carrier tunneling, and exciton charging conditions with the assistance of the Coulomb blockade effect.[40,174] At lower voltages, the emission is dominated by X^0 and X^+. With a preceding X^0 state, the electron tunnels out more rapidly than the exciton recombines, leaving behind a residual hole. The subsequent capture of the photo-generated e–h pair results in the X^+ complex. As the bias voltage increases, the X^+ complex disappears, and the XX^0 emerges. When another single electron tunnels into the QD with a stronger electric field, the X^- appears. It is notable that the transition energy is modified due to the charge carrier Coulomb interaction within X^+ and X^- complexes compared to X^0, and the XX^0 complex features an anti-binding energy within this small-sized QD.[175] The well-defined exciton states in QDs offer versatile platforms for implementing spin qubits, spin–photon interfaces, and quantum light sources, which have driven the booming progress of QD-based quantum technologies and the study of profound phenomena in light–matter interactions over the past two decades.

In addition to the commonly used PL method, photocurrent (PC) detection presents an alternative technique for effectively probing and controlling single QDs in electrically tunable devices. Unlike PL methods, which rely on radiative recombination, PC directly measures tunneled charge carriers generated through optical absorption. In a typical diode structure under applied bias, as illustrated in Fig. 6(d), the electric field enables photo-generated exciton complexes to tunnel out before recombination, producing a measurable current. A typical bias-dependent PC spectrum for a single exciton under fixed-energy laser excitation is shown in Fig. 6(e), exhibiting a clear Lorentzian resonance profile.[161] PC detection thus enables laser-background-free resonant high-resolution spectroscopy[176] to observe coherent optical phenomena, though it requires careful electrical device engineering to ensure efficient carrier extraction and compatibility with integrated optical nanostructures. Beyond PC readout, QDs can be electrically pumped in diode structures that inject carriers directly. This all-electrical excitation removes the need for external lasers, enables compact single-photon diodes,[177,178] and is fully compatible with photonic

integration. Nevertheless, electrical operation, which can be regarded as a non-resonant pumping scheme, often suffers from time jitter and excitation-induced charge noise, leading to reduced exciton coherence.[179,180]

B. Exciton decay dynamics and pure dephasing

Decay dynamics: The decay dynamics of excitons in QDs play a central role in determining their optical properties and coherent photon emission. As illustrated in the top panel of Fig. 7(a), exciton recombination generally proceeds via two primary channels: radiative decay, which results in spontaneous photon emission and directly contributes to single-photon generation; and nonradiative decay, where the exciton energy is dissipated into the surrounding solid-state environment without photon emission. The time-resolved PL spectrum reveals a typical decay curve for an InAs/GaAs QD in bulk, exhibiting an exciton lifetime of ∼900 ps. The radiative lifetime is governed by Fermi's golden rule, which correlates with the transition dipole moment (oscillator strength) and the local optical density of states (LDOS). The latter LDOS can be engineered by photonic nanostructures. In contrast, non-radiative mechanisms such as phonon emission,[184] carrier tunneling, dark-state admixture,[185] lattice defects or surface-states induced carrier trap,[186] surface recombination, and Auger process[187] lead to blinking and energy loss, which would reduce the emission brightness. The exciton states of QDs in nanostructures can be considerably perturbed by surface states, especially when in close proximity to a sidewall.

In particular, Auger recombination is a carrier-assisted process in which the recombination energy is transferred to an additional carrier and can proceed through both non-radiative and radiative channels. As shown in Fig. 7(b), for a negatively charged trion (X^-) with transition energy ω_1, non-radiative Auger recombination transfers the recombination energy to a third carrier, which could suppress quantum efficiency and broaden spectral linewidths.[187] Recent studies have presented radiative Auger recombination at the single-photon level,[188] where a redshifted photon ($\omega_2 = \omega_1 - \varepsilon$) is emitted alongside the energy ε transferred to the Auger carrier. These processes are governed by Coulomb interactions and QD symmetry breaking.[189] Spinnler *et al.*[181] observed satellite peaks in the PL spectra of X^- states under resonant excitation, as shown in Fig. 7(c), confirming radiative Auger signatures. For GaAs/AlGaAs QDs with dense hole states,[190] Yan *et al.*[182] reported multiple radiative Auger peaks from X^+ transitions

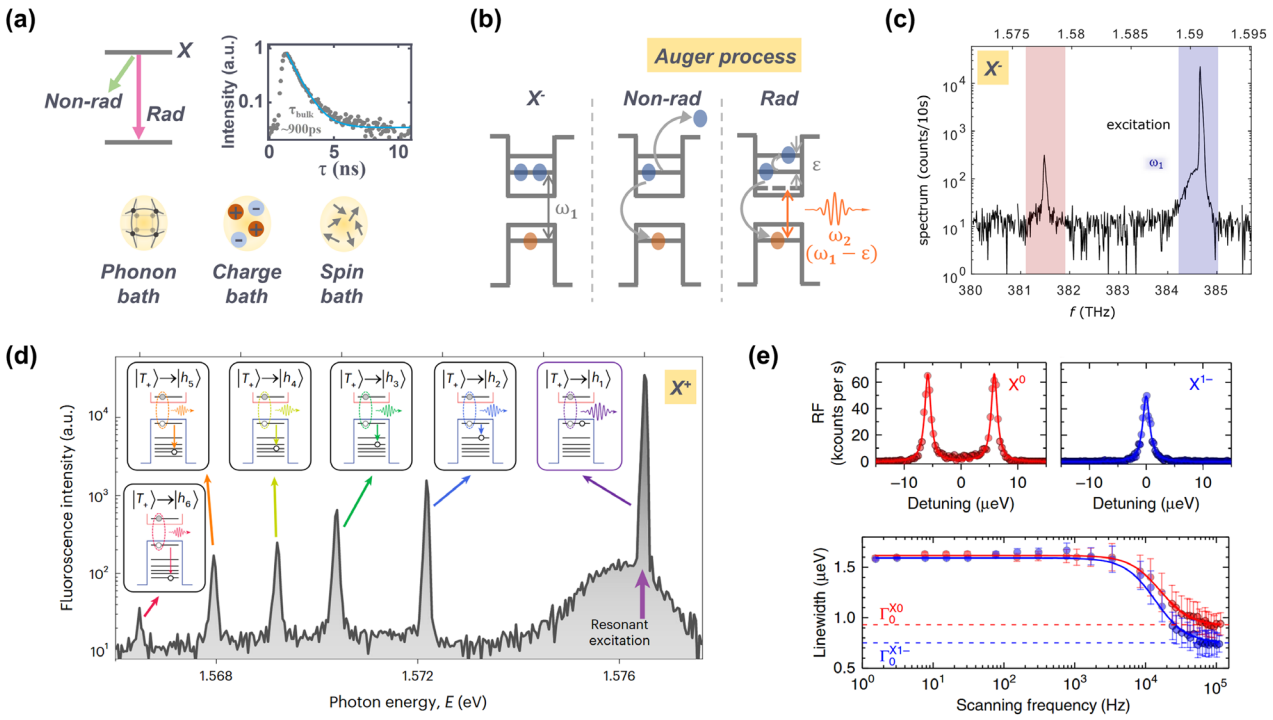

FIG. 7. Typical QD exciton decay behaviors and their spectral signatures. (a) The schematic illustrates radiative and non-radiative channels for an exciton and a time-resolved PL decay of single exciton indicating a typical exciton lifetime of InAs/GaAs QD in bulk matrix (top). The interactions with phonon, charge, and spin baths will contribute to the pure dephasing process (bottom). (b) Possible Auger recombination process for a X^- trion with transition energy of ω_1, including a non-radiative path occurring via carrier–carrier scattering, ejecting an excited electron instead of photon emission, whereas radiative recombination yields photon emission with reduced energy of $\omega_1 - \varepsilon$. (c) Emission spectrum showing both the fundamental trion transition (ω_1) and a red-shifted satellite peak, attributed to a radiative Auger process involving single excited electron. Reproduced from Spinnler *et al.*, Nat. Commun. **12**, 6575 (2021); licensed under a Creative Commons Attribution (CC BY) license.[181] (d) PL under resonant excitation of a positively charged exciton, revealing a set of radiative Auger transitions involving excited single hole. Reproduced with permission from Nat. Nanotechnol. **18**, 1139–1146 (2023). Copyright 2023, Springer Nature.[182] (e) Upper panels: High-resolution RF spectra of X^0 and X^- excitons under resonant excitation. Lower panel: Extracted exciton RF linewidths as a function of scanning frequencies. Reproduced from Kuhlmann *et al.*, Nat. Commun. **6**, 8204 (2015); licensed under a Creative Commons Attribution (CC BY) license.[183]

involving high-orbital hole states [Fig. 7(d)], offering an approach for the coherent control of excited carriers.

Dephasing process: As a promising candidate for the generation of highly indistinguishable single photons, the decoherence of QD arising from the complex solid-state environment poses a major obstacle. The non-resonant exciton pump is not ideal for generating indistinguishable single photons. Stochastic carrier capture introduces time jitter, which prevents the temporal determinism of the emitted single photons. Moreover, the relaxation process creates excess charges, additional excitonic complexes, and an increased phonon population in the QD surroundings, all of which induce exciton pure dephasing. Pure dephasing processes[191] could modify the state of the exciton and shift the transition energy slightly without energy relaxation, thereby degrading the indistinguishability of emitted photons. Therefore, within a simplified Markovian framework, the coherence time T_2 of a QD is determined jointly by the radiative decay time T_1 (governing spontaneous emission) and pure dephasing processes characterized by a timescale T_2^*, following the relation $1/T_2 = 1/(2T_1) + 1/T_2^*$.

As depicted in the bottom panel of Fig. 7(a), key decoherence channels include coupling to phonon baths,[192] charge baths,[193] and spin baths.[183,194] The surrounding charges, such as those trapped at material interfaces, defect sites, or in nearby QDs, will give rise to an energy shift through the electrostatic Stark effect and contribute to the spectral diffusion at the millisecond scale. Here the spectral diffusion refers to the random wandering of an exciton's optical transition frequency over time due to fluctuations in its surroundings. The randomly oriented nuclear spins of atoms lead to hyperfine interaction via fluctuating magnetic fields known as the Overhauser field on nanosecond timescales,[195] which dominates the T_2^*. Therefore, spin and charge noise typically introduce slow dephasing; this permits a finite temporal window during which the high coherence of emitted photons can be maintained, but not at a long delay time. To improve the exciton coherence, applying an electric field also helps stabilize the surrounding charge noise and an external magnetic field could stabilize the nuclear spin fluctuations.[196,197] The resonant excitation scheme helps reduce the time jitter and minimize environmental noise, where the active stabilization scheme may require extra setups.[198,199] The exciton linewidth in high-resolution resonant spectra can reflect dephasing properties, where pure dephasing manifests as the spectral broadening. Figure 7(e) presents the typical spectra of neutral and negatively charged excitons, X^0 and X^-, in a gated QD. Under varying scan rates, Fourier-transform-limited linewidths are observed when the scanning frequency is above 50 kHz.[183] When the gate voltage of the QD is scanned at a sufficiently high frequency, such that environmental fluctuations appear to be frozen out,[194] the resulting narrow RF emission linewidths indicate that the excitonic transition approaches the radiative lifetime limit and undergoes minimal pure dephasing and spectral diffusion. This behavior is close to the ideal coherence limit and reflects the high intrinsic optical quality of the exciton recombination process.

In contrast, the coupling with the phonon bath, dominated by longitudinal acoustic (LA) phonons, introduces a rapid dephasing mechanism that strongly affects QD coherence on the timescale of picoseconds.[200–202] This phonon-induced dephasing originates from inevitable interactions with the underlying crystal lattice vibrations, especially coupling through the deformation potential mechanism, which is inherently a non-Markovian process. Spectroscopically, such interactions manifest as the asymmetric broadening of phonon sidebands (PSB, spanning several meV) with a central zero-phonon line (ZPL), where the ZPL offers an ideal channel for deriving coherent photons. The impact of phonon dephasing increases significantly with temperature, owing to the thermally enhanced phonon population, which leads to the broadening of the ZPL.[203,204] Understanding and modeling exciton–phonon interactions are therefore essential for optimizing QD-based quantum devices and solid-state quantum photonics. When further incorporating the photonic structures, the PSB could be suppressed, with the coupled cavity acting as a spectral filter.[205–207] However, the existence of the phonon reservoir will intrinsically bring a trade-off between the brightness and indistinguishability of the single-photon sources (SPSs), even with a coupled cavity or waveguide.[208]

C. Resonance fluorescence and optical coherent control

QDs offer a solid-state platform with large dipole moments that is ideal for exploring RF.[212] Beyond their fundamental interest in quantum optics, the resonant driving of a single QD provides a prototypical setting for strong coherent exciton–photon coupling, which underpins fast, high-fidelity control of excitonic and spin qubits, as well as the generation of highly coherent single photons and nonclassical light for quantum information processing. As illustrated in Fig. 8(a), we begin with the two-level system with $|0\rangle$ and $|1\rangle$ states of transition energy ω excited by a resonant laser field. The Rabi frequency Ω represents the coupling strength between the electric field and the exciton, and $\gamma = 1/T_1$ denotes the exciton spontaneous emission rate. In the weak excitation regime with $\Omega \ll \gamma$, the elastically scattered light, dominated by coherent scattering with negligible inelastic contribution, inherits the spectral and temporal properties of the excitation laser. This enables an alternative pathway for single-photon generation beyond spontaneous emission. As the Rabi frequency increases ($\Omega \gtrsim \gamma$), the system enters the strong driving regime. In this case, incoherent emission dominates due to dressed exciton states, giving rise to the sideband of Mollow triplet[213] at $\omega \pm \Omega$ in the cw condition.

Weak excitation limit: In the limit of weak excitation, the elastic scattering of laser enables single-photon emission with a subnatural linewidth vs the QD radiative linewidth limit[214–216] and enables the waveform map from the laser to the scattered photon.[217] When embedded in an optical cavity, coherent Rayleigh scattering can be enhanced.[218] With decoherence playing an essential role,[219,220] the coherent scattering of QD deviates from the ideal atom behavior.[209,221] The RF emission exhibits a sharp ZPL and accompanying PSB are shown in Fig. 8(b), where the inset presents the high-resolution spectrum with the coherent and incoherent scattered fractions, which occur with the LA-phonon mediated Stokes or anti-Stokes scattering. Nevertheless, the brightness of the scattered photons in this regime is fundamentally limited by the requirement for stringent weak excitation. It is noteworthy that Raman scattering processes can produce spectrally narrow emission with a tunable energy range.[222–224] Such subnatural-linewidth and spectrally engineered photons are particularly attractive as building blocks for time-bin and frequency-encoded photonic qubits in quantum communication protocols.

Strong excitation limit: Extensive research has been devoted to exploring the behavior of the Mollow triplet formed by dressed exciton states in QD under cw resonant excitation[225–230] as well as the

Autler–Townes splitting observed in the three-level system.[231–234] Two Mollow sidebands enable narrow-band single-photon emission with a temporally ordered cascade process.[235] From a quantum-information perspective, the dressed-state picture and Mollow triplet provide a versatile toolbox for tailoring multi-photon correlations, generating frequency-multiplexed quantum channels, and engineering nonclassical light states that can be interfaced with quantum memories or used in few-photon nonlinear optics. In the context of the solid nature, phonon bath coupling would cause sideband emission dephasing[236,237] and the renormalization of the Rabi frequency.[238] Much more intricate quantum optical phenomena have been investigated within the Mollow region, including the interference effects from doubly dressed excitonic states under bichromatic driving,[239] simultaneous dressing of exciton and biexciton states,[240] the Mollow triplets in double Λ

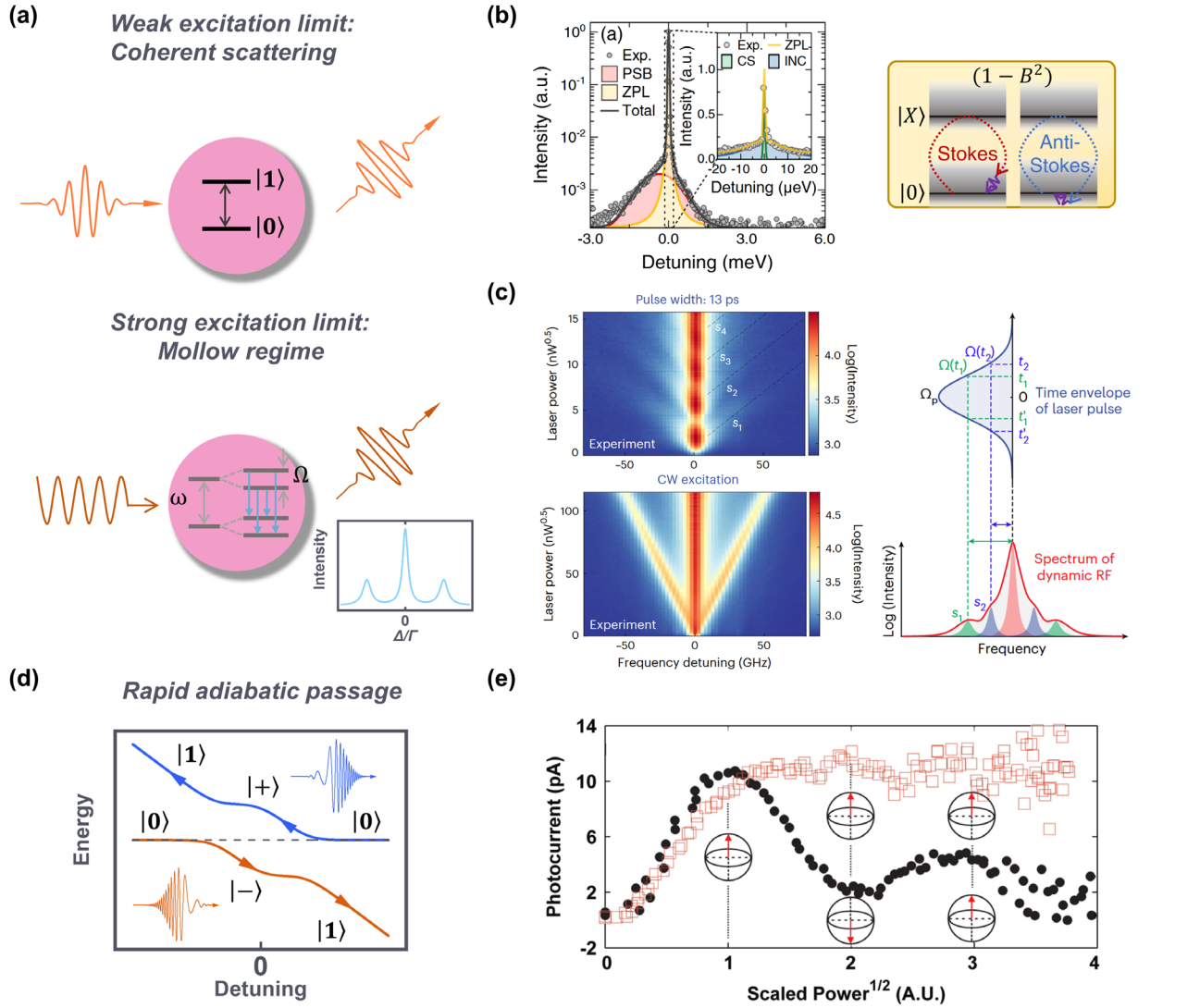

FIG. 8. RF in QDs under various excitation regimes. (a) Schematics illustrating the weak excitation limit (top), where coherent scattering dominates, and the strong excitation limit (bottom), where the system enters the Mollow regime, exhibiting incoherent sideband emission with cw pump. (b) RF spectra in the coherent scattering regime showing decomposition into the zero-phonon line (ZPL) and phonon sideband (PSB). Inset: High-resolution RF signal with fitted coherent (CS) and incoherent (INC) scattering components (left). The schematic diagram of inelastic scattering process mediated by LA-phonons through coupling with vibrational modes (right). Reproduced from Brash *et al.*, Phys. Rev. Lett. **123**, 167403 (2019); licensed under a Creative Commons Attribution (CC BY) license.[209] (c) RF results in the Mollow regime showing the dynamic RF using excitation pulses and static RF using cw excitation (left), with a schematic illustrating dynamic RF components governed by the time-dependent Rabi frequency (right). Reproduced with permission from Nat. Photonics **18**, 318–324 (2024). Copyright 2024, Springer Nature.[210] (d) Rapid adiabatic passage (RAP) for robust population transfer, illustrated through system energy evolution under negatively (blue) and positively (orange) chirped pulse excitation. (e) PC measurement of exciton population as a function of scaled pump power, revealing Rabi oscillations and robust RAP-based excitation. Reproduced from Wu *et al.*, Phys. Rev. Lett. **106**, 067401 (2011); licensed under a Creative Commons Attribution (CC BY) license.[211]

system,[241] and the few-photon excitation level.[242] Attention has turned toward the realization of dynamically dressed exciton states[243,244] under ultrafast pulsed resonant excitation (shorter than the exciton lifetime). In 2024, comprehensive studies were reported by Boos *et al.*[245] and Liu *et al.*[210] Figure 8(c) illustrates the power-dependent spectral features under both cw and pulsed resonant excitation, revealing characteristic signatures of the static and dynamic Mollow regimes.[210] Under pulsed excitation, the emergence of side peaks is attributed to interference between temporally separated Mollow components satisfying specific phase relations. Altogether, these phenomena illustrate how strong coherent exciton–photon coupling under resonant driving can be harnessed to sculpt the spectrum and statistics of emitted photons in a highly controllable manner, which is essential for implementing advanced photonic protocols in quantum information processing.

π-pulse excitation technique: Beyond coherent photon scattering, a widely adopted tool for deterministic coherent population control of a two-level excitonic system is resonant excitation using a π-pulse,[246] whereby bright on-demand single-photon emission is viable upon radiative decay.[229] A π-pulse indicates a time-integrated Rabi frequency area of π in the ideal two-level approximation. It could coherently drive the exciton from $|0\rangle$ to $|1\rangle$ with near-unity probability, experimentally manifested as Rabi oscillations in the PL emission intensity that peak at the π-pulse condition.[225,247] Early demonstrations of Rabi oscillations also employed differential transmittance[248,249] and PC detection,[176] with subsequent studies revealing damping effects induced by LA phonon interactions.[202,250–252] Compared to non-resonant cw excitation, RF under π-pulse suppresses re-excitation and avoids stochastic relaxation dynamics, thereby enabling deterministic single-photon emission with unprecedented high purity and indistinguishability.[253,254] This leads to the prosperous development of quantum light sources suitable for scalable photonic quantum computing and quantum networking. Simultaneously, fascinating quantum optical phenomena have been observed with π-pulse RF, including quadrature-squeezed photons[255] and intensity squeezing below the shot-noise limit,[256] as well as the generation of two-photon bound states,[257] photon-number superposition states,[258] and entangled states[259] under $2\,\pi$ or $4\,\pi$ pulse excitation. In turn, as a highly coherent process, RF could reflect the fluctuation of the exciton state[194] and the corresponding spectral diffusion.[260]

While the main technical challenge for RF still lies in the laser filtering. Although confocal microscopy with a cross-polarization scheme is commonly employed to suppress laser background based on the trion with intrinsic circular polarization, e.g., using a high-quality polarizer to filter the highly linearly polarized photons from the excitation laser and only collecting photons in the other polarization channel from the QD. Polarization filtering methods inevitably incur at least 50% signal loss. Alternative approaches, such as spatial separation of excitation and collection paths,[225,229,247] have been explored, albeit with additional demands for their alignment, while a phase-locked dichromatic excitation scheme[261] offers a promising solution.

Rapid adiabatic passage technique: On the other hand, rapid adiabatic passage (RAP) provides a robust approach for exciton population control that is insensitive to fluctuations in laser pulse intensity and detuning.[211,266–269] As depicted in Fig. 8(d), RAP enables reliable population transfer from state $|0\rangle$ to $|1\rangle$ using frequency-chirped pulses. Thus, the Rabi frequency $\Omega(t)$ and instantaneous detuning vary over time, and the laser frequency is swept through the exciton resonance. In the rotating-frame Hamiltonian, the optical driving creates dressed states $|+\rangle$ and $|-\rangle$, whose energies exhibit an avoided crossing. When the adiabatic condition is satisfied, the system state evolves by following a single instantaneous dressed state throughout the avoided crossing, which is $|-\rangle$ or $|+\rangle$ for positively or negatively chirped pulses, respectively. This ensures the population inversion from the ground state to the excited state, particularly effective in the high pulse area region with decoupling carrier–phonon,[270] outperforming π-pulse excitation in stability and reproducibility. However, negatively chirped pulses are susceptible to phonon-emission-induced $|+\rangle \rightarrow |-\rangle$ relaxation, which can degrade or even break the RAP process in practice.[266] In contrast, positively chirped pulses provide a more robust RAP implementation.[267,271] This makes RAP a powerful tool for deterministic exciton preparation and high-quality single-photon generation, and its robustness against pulse-area and detuning fluctuations is particularly appealing for implementing stable qubit initialization and control in solid-state quantum information processing architectures.

RAP has enabled robust collective manipulation of QDs[272,273] and high-resolution far-field imaging,[274] with recent progress[275,276] reviewed in reference.[277] Figure 8(e) presents the typical coherent exciton control behaviors using the PC method under π-pulse excitation (black dots) and RAP-based preparation (orange squares).[211] By exploiting non-resonant coupling to the PSB,[278] LA phonon-assisted pulsed excitation enables efficient laser background rejection and supports robust exciton preparation similar to RAP via phonon relaxation,[190,279–282] without significant degradation of single-photon quality due to time jitter.[283] Recently, a novel excitation scheme called swing-up of quantum emitter population has been developed.[284] This approach achieves deterministic and coherent exciton preparation through two red-detuned laser pulses, where the pulse beating effect is exploited.[285] As a purely off-resonant excitation scheme, it shows great potential for high-brightness single-photon emission in single QDs.

D. External field modulation

To tailor the electronic and optical properties of QD for practical quantum photonic devices, various external perturbations have been employed to modulate QD behavior in a controllable and reversible manner. The universal toolbox includes electric fields, magnetic fields, strain fields, and surface acoustic waves (SAWs), each providing distinct mechanisms for manipulating QD states.

Applying a static electric field, typically through a p–i–n diode, enables energy tuning of QD emission via the quantum-confined Stark effect[286] with modified electron–hole spatial overlap. That is, when the field is applied along the growth direction, precise energy tuning can be realized following a quadratic dependence on the field strength F, given by $E(F) = E(0) + pF + qF^2$, where $E(0)$ is the exciton energy at zero field, p is the permanent dipole moment, and q is the polarizability. Energy of X^0 and X^+ states under varying bias voltages extracted from PL and PC measurements are shown in Fig. 9(a), redrawn from reference.[262] Large DC Stark shifts of several tens of meV are attainable in QDs.[287] A vertical electric field can also tune the FSS because the two bright-exciton eigenstates possess different z-projected permanent dipole moments in an asymmetric QD[288,289] with FSS value as low as 0.4 μeV recently achieved.[290] A lateral electric field provides an alternative route to cancel the FSS with limited Stark

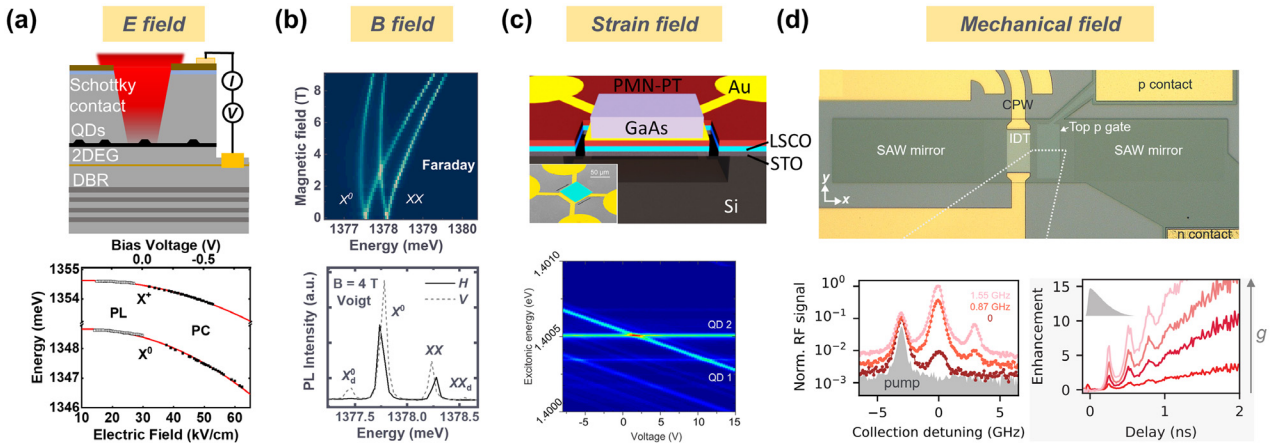

FIG. 9. External field control of QD properties via electric, magnetic, strain, and mechanical fields. (a) Electric field: A Schottky diode structure enables tunable QD emission via the quantum-confined Stark effect, as shown in the PL and PC spectra under different bias voltages. Reproduced from Wu *et al.*, Phys. Rev. Appl. **14**, 014049 (2020); licensed under a Creative Commons Attribution (CC BY) license.[262] (b) Magnetic fields: Applied *B* fields in Faraday geometries lift spin degeneracy, showing the Zeeman splitting and diamagnetic shift (top). PL spectra present the mixing of bright and dark states of X^0 and XX^0 under *B* fields in Voigt geometries (bottom). Reproduced from Peng *et al.*, Phys. Rev. Appl. **8**, 064018 (2017); licensed under a Creative Commons Attribution (CC BY) license.[263] (c) Strain field: the schematic and SEM image of a nano piezoelectric actuator consisting of a GaAs QD nanomembrane bonded to a PMN–PT/LSCO/STO/Si structure, with patterned Au electrode (top). The excitonic transitions of spatially separated QDs can be brought into spectral resonance by sweeping the piezo voltage (bottom). Reproduced with permission from Nano Lett. **16**, 5785–5791 (2016). Copyright 2016, American Chemical Society.[264] (d) Mechanical field: SEM image of the device generating surface acoustic waves (top), enabling coherent control of QD dynamics. Spectra under red-detuned cw pump at the detuning of $-\omega_{SAW}$ and time-resolved population enhancement under gradually decreasing pump pulses with varying optomechanical coupling rates *g* (bottom). Reproduced from DeCrescent *et al.*, Optica **11**, 1526 (2024); licensed under a Creative Commons Attribution (CC BY) license.[265]

shifts.[291–293] Meanwhile, charge occupancy can be controlled with the different configuration of the bias-dependent band and Fermi level, confirmed by various exciton plateaus when sweeping voltage.[173] With recent studies extending to GaAs QDs, electric field control is beneficial for suppressing charge noise[294,295] and realizing resonance conditions of single QD and an optical resonance mode and energy matching for distinct QDs.[296,297] In addition to the DC Stark effect, driven by a detuned laser, the AC Stark effect enables a contact-free tuning of excitonic energy through an optical method.[234,298,299]

Magnetic fields offer the basic tool to lift the spin degeneracy of QD states and promote coherent spin manipulation. As shown in Fig. 9(b) for X^0 and XX^0 states in a gate-controlled QD,[263] the magnetic field in the Faraday geometry (vertical field parallel to the growth axis) induces Zeeman splitting between spin-polarized excitonic states.[300] Circular polarization of the neutral exciton is recovered with a strong Zeeman effect vs the exchange interaction.[93,301] In addition, the exciton energy shows a diamagnetic blue-shift caused by the shrinking carrier wavefunction.[302,303] While the magnetic field of Voigt geometry (lateral magnetic field perpendicular to the growth direction) enhances spin–flip transitions and the coherent mixing of bright and dark exciton states, the dark state is observable with polarization-resolved *H* and *V* states separated by the FSS, where the FSS can also be reduced via transverse magnetic field.[289,304] The Voigt magnetic field lays the foundation for applications including the initialization and manipulation of spin qubits[305–307] and spin–photon entanglement.[308–312]

Using piezoelectric actuators offers a strain tuning pathway for single QD, that is, applying uniaxial,[313–315] biaxial,[316–319] or multiaxial[320–322] elastic stress along specific crystallographic axes to QD membranes. This enables the study of light-hole excitons.[164,165] The resulting lattice deformation modifies the QD structure and confinement potential, allowing for deterministic tuning of emission energy and FSS. Strain control is thereby particularly valuable for producing polarization-entangled photon pairs by suppressing FSS (further discussed in Sec. IV). Figure 9(c) presents an integrated QD nanomembrane bonded to the PMN-PT piezoelectric material thin film, grown on the monolithically epitaxial $LaSrCoO_3/SrTiO_3/Si$ structure, where the $LaSrCoO_3$ and Au both serve as electrodes. The energy resonance of two spatially separated QDs mounted on distinct PMN–PT actuators can be tuned with varying piezo voltage, showing the scalable potential of these individually addressable strain-controlled QD devices.[264]

Dynamical mechanical modulation can be realized via SAWs, enabling high-frequency (GHz-scale) control of exciton states through time-periodic strain and electrical field across the QD structure.[323,324] These acoustic fields can control QD transition energies, carrier dynamics, and exciton occupations on nanosecond timescales, whose basic principle has been comprehensively reviewed in Ref. 325, serving as an ideal interface for the interplay between the exciton, photon, and phonon.[326–328] Recently, DeCrescent *et al.*[265] reported the mechanically assisted photon scattering to promote coherent RF control. As shown in Fig. 9(d), an interdigital transducer inside a SAW cavity launches SAW phonons that couple to the embedded QD at a rate *g*. When the laser is detuned by $-\omega_{SAW}$ from the exciton resonance, SAW modulation increases the scattered-photon intensity at the bare exciton frequency, with the employed *g* indicated by the different red color. With a gradually decaying excitation pulse, the enhancement of the exciton occupancies under SAW control first rises with oscillations and then increases monotonically compared to the QD without SAW coupling. This enhancement effect based on phonon interaction grows stronger as *g* becomes larger.

IV. QUANTUM LIGHT SOURCES AND QUBITS BASED ON QDs

QDs serve as versatile platforms for quantum technologies, intrinsically enabling deterministic single-photon emission and on-demand entangled photon pairs with high quality. QD-confined single exciton/spin states naturally enable the realization of matter (stationary) qubits. This section discusses the basic principle of QD-based flying qubits, including their performance metrics and engineering strategies, and spin qubits, covering the all-optical initialization/manipulation scheme and nuclear spin quantum memory.

A. Single-photon sources

Quantum light sources, which emit light with intrinsically nonclassical properties, are fundamental building blocks for quantum technologies such as quantum communication,[9] quantum computing,[330] and quantum metrology.[331] Among them, two representative types are SPSs and entangled photon pair sources. The SPS emits one and only one photon at a time, and the entangled photon pair source produces two photons in a quantum-correlated state. Traditional photon-pair sources based on spontaneous parametric downconversion (SPDC) generate entangled photon pairs probabilistically.[332] This inherent randomness leads to a non-negligible probability of multi-photon events, which limits their scalability in applications requiring deterministic photon generation. In contrast, semiconductor QDs act as artificial atoms with discrete energy levels, enabling the triggered emission of single photons or entangled photon pairs through excitonic radiative transitions. As a result, QD-based light sources exhibit sub-Poissonian photon statistics and high quantum efficiency under appropriate excitation conditions. The performance of single-photon sources is typically characterized by three key metrics: purity, indistinguishability, and brightness.

Purity reflects the degree of suppression of multiphoton events and is typically quantified by the second-order correlation function $g^{(2)}(\tau)$, measured using a Hanbury Brown and Twiss (HBT) setup,[333] as shown in Fig. 10(a). In this configuration, the PL from the QDs is split into two paths and detected by a pair of single-photon detectors. The second-order correlation function $g^{(2)}(\tau)$ is derived from the coincidence histogram of detection events. For an ideal SPS, $g^{(2)}(0) = 0$ indicates perfect antibunching and no simultaneous detection. In practice, $g^{(2)}(0) < 0.5$ is commonly regarded as evidence of non-classical emission. The lower $g^{(2)}(0)$ value corresponds to the higher purity. Figure 10(b) shows a second-order correlation measurement under pulsed excitation,[329] with negligible coincidence counts at zero delay, confirming excellent single-photon purity.

Indistinguishability represents whether all the parameters of each photon emitted by an SPS are identical. It is essential for optical quantum computing because entangling operations in linear optics arise from multi-photon interference; any residual which-path information suppresses the interference and degrades gate fidelity.[103] The indistinguishability of two photons emitted by a single QD with a longer time interval has been expected for the single-photon application with quantum advantages,[334] which demands improved exciton coherence. The experimental setup used to measure photon indistinguishability is the Hong–Ou–Mandel (HOM) setup,[335] as shown in Fig. 10(a). Under pulsed excitation, an unbalanced Mach–Zehnder interferometer with a delay equal to one laser period overlaps two consecutive photons at a 50:50 beam splitter. If two photons are perfectly indistinguishable, quantum interference causes them to coalesce and exit through the same output port, suppressing coincidence detections and implying that the second-order correlation function at zero time delay tends to zero.[329] The HOM visibility—and thus the indistinguishability—is obtained by integrating the zero-delay peak of the interfering trace (parallel polarization) and comparing it either to a non-interfering

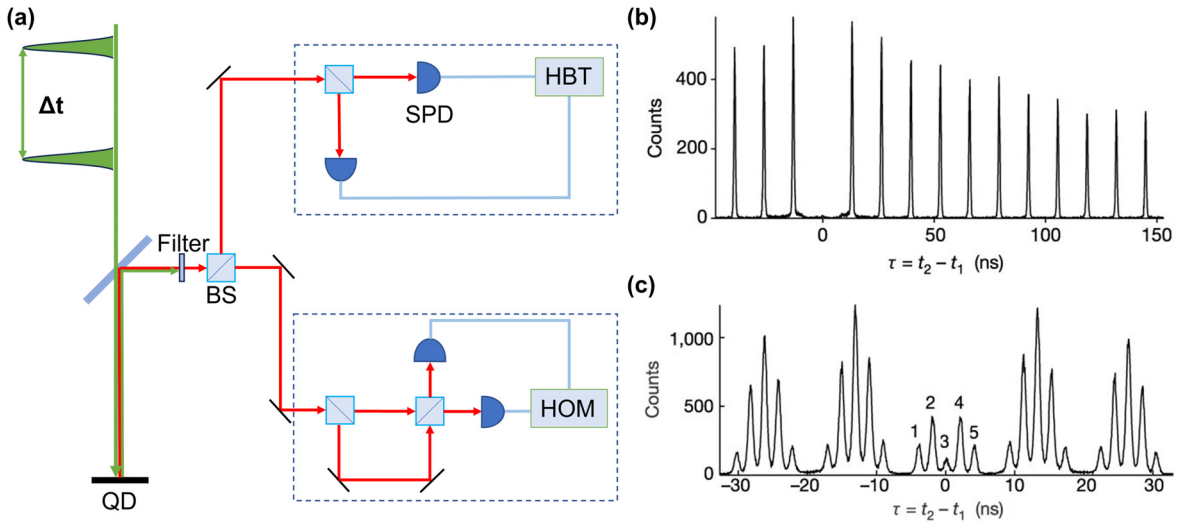

FIG. 10. QD-based single-photon sources (SPSs) (a) Experimental setup for characterization of single photons emitted by QDs. Hanbury Brown and Twiss (HBT) setup and Hong–Ou–Mandel (HOM) setups are used to characterize the purity and the indistinguishability of a single photon, respectively. (b) Second-order correlation measured by HBT setup. Obvious antibunching was observed at zero time delay. (c) Second-order correlation measured by HOM setup. The dip at zero time delay implies a high degree of indistinguishability. Reproduced with permission from Nature **419**, 594–597 (2002). Copyright 2002, Springer Nature.[329]

reference (cross-polarized or large delay) or to the average of the nearest side peaks. After subtracting accidentals and correcting for splitter imbalance and detector efficiencies, the reported visibility directly reflects photon indistinguishability.

Brightness measures the efficiency of generating and collecting single photons. It is related to the fluorescence quantum yield of QD and the photon extraction efficiency, where the latter one is generally defined as the photon collection efficiency at the first objective lens in free-space measurement configurations to exclude the variations of the used optical setups.[103] High-brightness quantum light sources[336,337] are essential for various quantum information applications, such as the multi-photon interference task[338] and fault-tolerant linear optical quantum computing,[339,340] where the generation of large numbers of indistinguishable single photons serves as the fundamental resource for complex quantum protocols.

Simultaneously achieving high brightness, purity, and indistinguishability remains a significant experimental challenge. Various approaches have been developed involving excitation schemes, device structures, and sample growth. For instance, deterministic excitation via resonant π-pulses enhances photon coherence and spectral purity by avoiding uncertainties and noise from carrier relaxation.[253] To improve photon brightness, QDs are embedded into nanophotonic structures such as micropillar cavities or PHC cavities. These structures exploit the Purcell effect to boost spontaneous emission rates and direct emission into specific optical modes, significantly increasing collection efficiency (see Sec. V for details). Additionally, strategies like polarization-selective cavities,[344] phase-locked dichromatic excitation,[261] and two-photon resonant excitation with triggering schemes[345–347] have been developed to mitigate losses associated with conventional resonant excitation filtering.

B. Entangled photon pairs

Entangled photon pairs consist of two photons whose quantum states, such as polarization or energy-time modes, are inseparably correlated, forming a quantum-entangled state. Compared with conventional sources based on the probabilistic SPDC process in nonlinear crystals, semiconductor QDs enable a deterministic generation of polarization-entangled photon pairs via the biexciton–exciton (XX^0–X^0) radiative cascade. This concept was first proposed by Benson *et al.*[348] and later experimentally demonstrated in seminal experiments.[304,349] A key challenge in realizing high-fidelity entangled photon emission from QDs is the suppression of the FSS, for which the origin has been detailed in Sec. IV A. This splitting renders the two-photon emission paths distinguishable in frequency and polarization, thereby degrading entanglement. With the existence of energy splitting δ_{FSS}, the emitted two-photon state can be described as $|\psi\rangle = 1/\sqrt{2}(|H_{XX^0}H_{X^0}\rangle + e^{i\delta_{FSS}t/\hbar}|V_{XX^0}V_{X^0}\rangle)$, where t is the emission lifetime of XX^0 to X^0. Ideally, if the FSS is eliminated, the time-dependent phase vanishes, and the system recovers a maximally entangled Bell state, typically expressed as $|\phi^+\rangle = \frac{1}{\sqrt{2}}(|H_{XX^0}H_{X^0}\rangle + |V_{XX^0}V_{X^0}\rangle)$. This state represents the highest degree of quantum correlation: each individual photon is completely unpolarized when measured alone, while joint measurements in the same polarization basis are perfectly correlated. Consequently, the quality of the generated entanglement is quantified by the entanglement fidelity f with respect to a target Bell state, defined as $f = \langle\phi^+|\rho_{\text{exp}}|\phi^+\rangle$, where ρ_{exp} is the two-photon density matrix reconstructed from polarization-resolved correlation measurements or quantum state tomography. Therefore, minimizing the FSS is essential to maximize the fidelity and approach the ideal limit of unity ($f = 1$).

For higher entanglement fidelity and deterministic excitation, two-photon resonant excitation (TPE) is commonly used, as shown in Fig. 11(a). This technique employs a pulse laser with photon energy $E_{\text{laser}} = 1/2(E_{XX^0} + E_{X^0})$ to drive the two-photon transition from the ground state to the biexciton via a virtual intermediate level. TPE method also enables the spectral separation between scattering laser and emission. The system then spontaneously emits a biexciton and an exciton photons in sequence. Figure 11(b) illustrates synchronized Rabi oscillations of the exciton and biexciton populations under TPE.[341] This TPE excitation eliminates uncertainty from relaxation processes, enhances temporal synchronization, and improves entanglement fidelity. Moreover, as the excitation light is spectrally separated from the emission lines, it allows efficient filtering of the excitation background. Compared to the direct pulsed resonant excitation, pulsed TPE could further improve the purity of the single-photon emission by suppressing the pulse length dependent re-excitation and subsequent multi-photon contribution.[350]

Several tuning methods have been developed to suppress or eliminate FSS in QDs, including electric fields,[288] magnetic fields,[304] and strain engineering.[342,351,352] Among these, strain tuning is particularly effective, as it enables simultaneous control over emission energy and the FSS. Figure 11(c) shows a typical device configuration where a QD membrane is bonded onto a two-dimensional piezoelectric actuator, allowing fine adjustment of in-plane strain to achieve near-zero FSS. This strain tuning can achieve tuning of FSS and emission wavelength independently, as shown in Fig. 11(d). Moreover, materials such as GaAs/AlGaAs droplet-epitaxy QDs inherently exhibit smaller FSS,[99,353] making them favorable for the direct generation of high-fidelity entangled photon pairs. Under such tuning conditions, polarization-resolved coincidence measurements reveal clear signatures of entanglement. In addition to the conventional pair of photons generated by two single-photon emissions shown in Fig. 11(a), the biexciton state could also generate entangled photons through the direct spontaneous two-photon emission directly, i.e., two photons with the same energy, as shown in Fig. 11(e). Such two-photon emission can simultaneously achieve near-unity entanglement fidelity and on-demand generation,[343] and can be further enhanced by the nanophotonic cavity as discussed in Sec. V.

Recently, entangled photon sources (EPS) based on semiconductor QDs have been applied in practical applications in quantum networks, entanglement swapping,[354,355] and quantum key distributions.[356] By incorporating advanced photonic engineering techniques, such as optimized broadband cavities, further improvements in emission efficiency, entanglement fidelity, and photon indistinguishability are expected to be achieved, which are important for quantum communication, quantum repeaters, and entanglement-based quantum computing.

C. Solid-state qubits based on QDs

As artificial atomic systems, QDs possess rich excitonic energy level structures and spin degrees of freedom, enabling the construction of solid-state qubit systems. In addition, their strong dipole interactions provide a robust spin–photon interface. On one hand, optical excitation and detection techniques enable the initialization, manipulation, and readout of spin qubits. On the other hand, QDs hold great

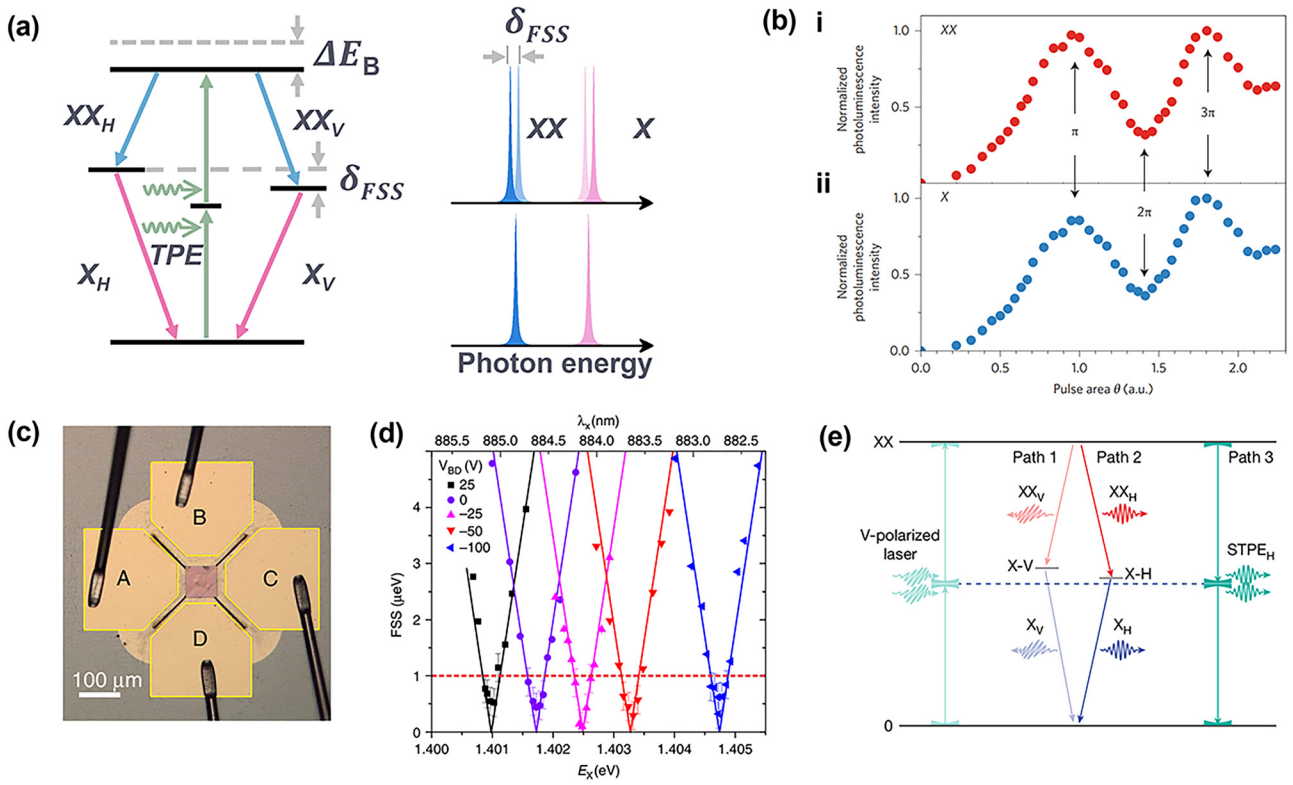

FIG. 11. QD-based polarization entangled photon sources (EPSs). (a) Schematic illustration of entangled photon pair generation via the biexciton–exciton radiative cascade. Due to the presence of FSS, the biexciton and exciton exhibit linearly polarized emission peaks. Eliminating the FSS is essential for generating polarization-entangled photon pairs. The energy difference between XX^0 and X^0 reflects the biexciton binding energy ΔE_B. (b) Rabi oscillations of the biexciton (i) and exciton (ii) under two-photon excitation (TPE). Reproduced with permission from Nat. Photonics **8**, 224–228 (2014). Copyright 2014, Springer Nature.[341] (c) Optical micrograph of the strain-tunable QD device. A GaAs nanomembrane containing InAs QDs is integrated onto a suspended PMN-PT thin film with four actuation legs. (d) Measured FSS vs exciton wavelength under different uniaxial stress configurations, demonstrating independent control of FSS and emission wavelength. Reproduced from Chen *et al.*, Nat. Commun. **7**, 10387 (2016); licensed under a Creative Commons Attribution (CC BY) license.[342] (e) Entangled photon sources from spontaneous two-photon emission. Reproduced with permission from Nature **643**, 1234–1239 (2025). Copyright 2025, Springer Nature.[343]

potential for achieving efficient coupling between stationary spin qubits and flying photonic qubits, paving the way toward the realization of multi-node quantum networks.

Figure 12(a) illustrates a common spin qubit platform.[357] To fully exploit the spin degree of freedom of a single electron in a QD, an external magnetic field is typically applied to lift the spin-state degeneracy and create a controllable energy level structure. Under a transverse magnetic field (Voigt geometry), the electron spin states and the two excited states (trion states) form a four-level Λ system. In this system, all four linearly polarized transitions are allowed by optical selection rules, enabling the implementation of Raman transitions between the spin ground states.

Spin initialization can be achieved via optical pumping: for example, tuning a laser resonantly to the $|\downarrow\rangle \rightarrow |\uparrow\downarrow\Uparrow\rangle$ transition causes electrons to be repeatedly pumped out and spontaneously decay back to the $|\uparrow\rangle$ state, resulting in high-fidelity initialization. Spin manipulation is performed by applying a strong, off-resonant, circularly polarized picosecond laser pulse between the spin states. This drives a coherent Raman process between $|\downarrow\rangle$ and $|\uparrow\rangle$, effectively realizing rotations within a two-level system. In the experiments, multiple periods of Rabi oscillations can be observed by controlling the intensity of a single laser pulse, demonstrating the ability to rotate the electron spin by arbitrary angles,[357] as shown in the bottom panel in Fig. 12(a). By applying two coherent pulses and varying their separation time, Ramsey interference experiments were performed, confirming control over the rotation axis direction. These operations are equivalent to arbitrary rotations on the Bloch sphere. By adjusting the rotation angle via Rabi oscillations and the rotation axis via Ramsey interference, one can implement arbitrary single-qubit unitary operations. This establishes full SU(2) control, i.e., the ability to generate any unitary transformation in the SU(2) group by tailoring the amplitude, phase, and timing of the driving pulses, thereby coherently steering the qubit from any initial state to any desired target state on the Bloch sphere.

Based on similar schemes, subsequent studies have demonstrated entanglement between a single spin in a QD and an emitted photon,[308] with extensions into the telecommunications band.[309,359] Furthermore, by exploiting the long-lived states of dark excitons or hole spins,[312,360–362] the generation of photonic cluster states has been experimentally realized, significantly expanding the potential of semiconductor QDs as nodes in quantum networks.

The manipulation and fidelity of electron spin states in QDs are inevitably significantly influenced by the surrounding nuclear spin

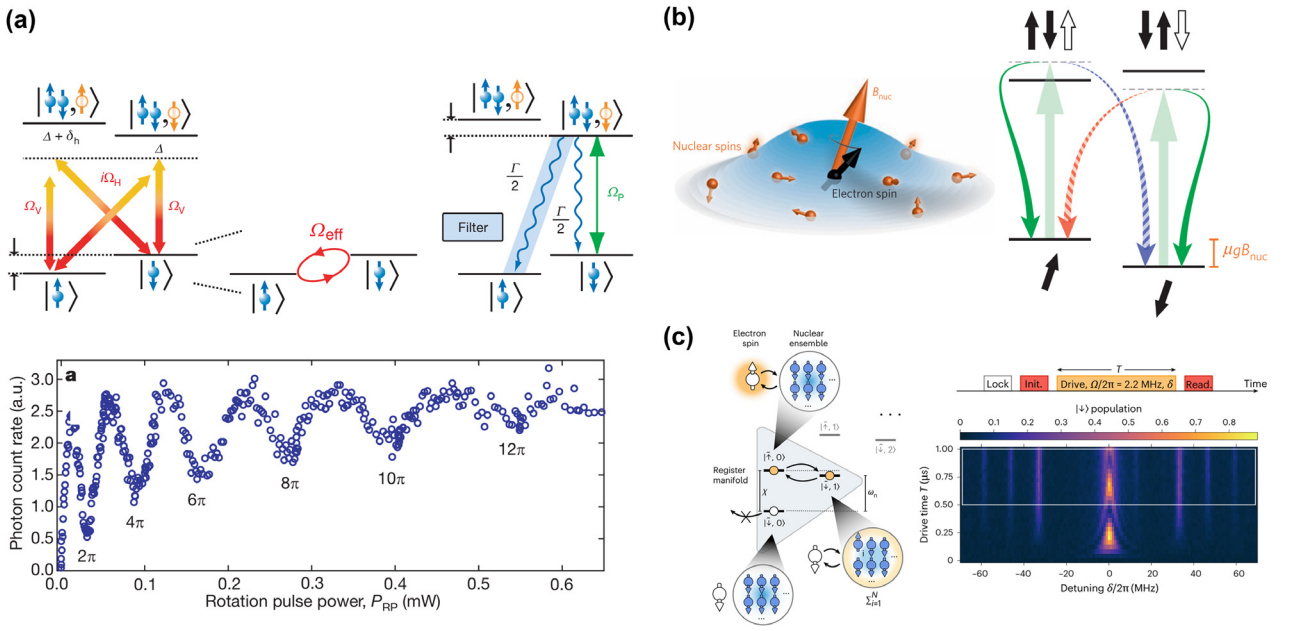

FIG. 12. QD-based spin qubit and the role of nuclear spin. (a) Schematic and experimental demonstration of optical spin qubit control in a QD. A single electron spin confined in a QD is manipulated via a stimulated Raman transition using picosecond optical pulses. Initialization and readout are performed by resonant optical pumping. Rabi oscillations between spin-up and spin-down states are observed by varying the power of the rotation pulse, demonstrating coherent control of the qubit rotation angle. Reproduced with permission from Nature **456**, 218–221 (2008). Copyright 2008, Macmillan Publishers.[357] (b) Influence of the nuclear spin on optical spin selection rules in a QD. Reproduced with permission from Nat. Phys. **10**, 725–730 (2014). Copyright 2014, Springer Nature.[199] The hyperfine interaction generates an effective Overhauser field that sets the spin quantization axis and alters the strength of allowed and spin–flip transitions. (c) Nuclear spin ensemble as a quantum register for electron spin qubits. The electron spin couples to a polarized nuclear ensemble, enabling state transfer. Electron spin resonance (ESR) spectrum showing resolved nuclear sidebands, allowing selective access to different nuclear species for coherent control. Reproduced from Appel *et al.*, Nat. Phys. **21**, 368–373 (2025); licensed under a Creative Commons Attribution (CC BY) license.[358]

environment. On one hand, nuclear spin fluctuations induce a random effective magnetic field (Overhauser field) on the electron spin via the hyperfine interaction, constituting a major source of decoherence. The quasi-static Overhauser field from nuclear spins defines a different spin quantization axis across experimental time windows, leading to inhomogeneous Zeeman splitting in the energy level structure, as shown in Fig. 12(b), thereby compromising spin qubit controllability and reproducibility.[199] This intrinsic uncertainty of the environmental magnetic field noise limits the fidelity of spin readout and manipulation, particularly under zero or low external magnetic fields. Several methods have been employed to mitigate nuclear spin effects on spin qubits,[363–366] such as dynamical decoupling and using lattice-matched QD structures. Furthermore, since holes primarily consist of atomic p-orbitals with zero wavefunction amplitude at the atomic nuclei, utilizing hole spins can suppress nuclear spin noise and achieve longer coherence times.[40,367]

Although nuclear spin fluctuations are considered a primary mechanism for electron spin decoherence in QDs, recent experimental studies reveal that the nuclear spin system itself can be harnessed as a useful quantum memory resource. Recent work employed an all-optical Raman cooling scheme to suppress nuclear spin fluctuations well below the nuclear Zeeman energy, thereby accessing the sideband-resolved regime for the first time.[368] Under these conditions, they observed multiple nuclear spin sideband excitations via off-resonant driving and demonstrated coherent driving of a single "nuclear magnon" excitation. This showcased resonant exchange between the electron-nuclear system, enabling the manipulation of collective nuclear spin excitations. Recently, Appel *et al.*[358] demonstrated a reversible quantum state transfer between the electron spin and a nuclear spin dark state, as shown in Fig. 12(c). They utilized the nuclear spins as a quantum register, demonstrating a complete write–store–read cycle with a storage time of 130 μs and an overall fidelity near 70%. Combined with dynamical decoupling techniques, this time could potentially be extended to the millisecond range. This achievement signifies the transformation of nuclear spins within the QD platform from a disordered environment into a structured, controllable quantum resource. In addition to this, nuclear spins can be used as quantum sensors. In a recent study, individual nuclear spin excitations were detected within a dense ensemble of approximately 80 000 nuclei,[369] underscoring their potential as a controllable resource for future quantum technologies. These works demonstrate a controllable pathway for converting the electron-nuclear coupling between a decoherence source[199] and a "quantum register."[358,368,370] This not only provides new strategies for extending qubit coherence times but also establishes the physical foundation for building flying qubit–stationary interfaces equipped with quantum memory.

V. CAVITY QUANTUM ELECTRODYNAMICS

QDs host the quantum state of a single electron/hole or exciton at the quantum limit, and the dipolar allowed optical transitions enable

the coupling of the exciton to a single photon. However, a single photon in free space has very weak optical field overlap with the QD, which limits the interaction between the exciton and the photon. By comparison, an optical cavity can confine the photon at the micro- or nanoscale, thereby significantly enhancing the LDOS. The interaction between the confined photon and the exciton of QD embedded in the cavity is therefore greatly enhanced. Depending on whether the cavity–QD exchange coupling exceeds the decay rates of both the cavity and the QD, the system operates in the strong or weak coupling regime. Such a cavity–QD system is an ideal platform for the study of light–matter interactions at the quantum limit, which is an important research area in quantum photonics and quantum information processing. This chapter will introduce the fundamental theory of cQED, the development of the cavity–QD devices, and their applications in quantum photonic technologies.

A. Coupling theory

We first discuss the fundamental theory of the cavity–QD coupling, for which the system consists of a single QD embedded in a single cavity supporting a single confined photonic mode. The QD is a two-level system including the ground state G and the excited state X, while the spontaneous emission ($X \rightarrow G$ transition) has the energy $\hbar\omega_X$ and the linewidth (decay rate) $\hbar\gamma_X$. The eigenfrequency of the bare QD is thus written as $\Omega_X = \omega_X + i\gamma_X/2$. The photons confined in the cavity are identical and have the energy $\hbar\omega_c$ and the linewidth (loss rate) $\hbar\kappa$, corresponding to the eigenfrequency $\Omega_c = \omega_c + i\kappa/2$. The state of the system can be described by the combination of the state of QD (X/G) and the number of photons in the cavity mode N as $|X/G, N\rangle$. At the weak excitation limit, the system has three allowed states, i.e., $|G, 0\rangle$, $|X, 0\rangle$, and $|G, 1\rangle$, corresponding to the ground state of the system, the state with excited QD, and the state with one photon in the cavity, respectively. Exciton–photon coupling occurs between the state $|X, 0\rangle$ and $|G, 1\rangle$, i.e., $\langle X, 0|H|G, 1\rangle$ means the photon is absorbed by the QD, and $\langle G, 1|H|X, 0\rangle$ means the QD emits a photon to the cavity. This interaction has the coupling strength (exchange rate) $\hbar g$. The Hamiltonian of this cavity–QD system H is then written as

$$H\begin{bmatrix} |X,0\rangle \\ |G,1\rangle \end{bmatrix} = \begin{bmatrix} \Omega_X & g \\ g & \Omega_c \end{bmatrix}\begin{bmatrix} |X,0\rangle \\ |G,1\rangle \end{bmatrix}. \quad (1)$$

The two eigenfrequencies of the system $\Omega_\pm = \omega_\pm + i\gamma_\pm/2$ are then solved as

$$\Omega_\pm = \frac{\Omega_X + \Omega_c}{2} \pm \sqrt{\frac{(\Omega_X - \Omega_c)^2}{4} + g^2}. \quad (2)$$

When the cavity and QD are at resonance $\omega_X = \omega_c = \omega_0$, the energies (real part) of the eigenstates are

$$\hbar\omega_\pm = \hbar\omega_0 \pm \mathrm{Re}\left(\hbar\sqrt{g^2 - \left(\frac{\gamma-\kappa}{4}\right)^2}\right), \quad (3)$$

and the linewidths (imaginary part) are

$$\hbar\gamma_\pm = \hbar\left(\frac{\gamma+\kappa}{2}\right) \pm \mathrm{Im}\left(\hbar\sqrt{4g^2 - \left(\frac{\gamma-\kappa}{2}\right)^2}\right), \quad (4)$$

for which the results are presented in Fig. 13(a). As shown, determined by whether $g\langle|\kappa-\gamma|/4$ or $g\rangle|\kappa-\gamma|/4$, the system is in the weak or strong coupling regime. We calculate the spectra using the master

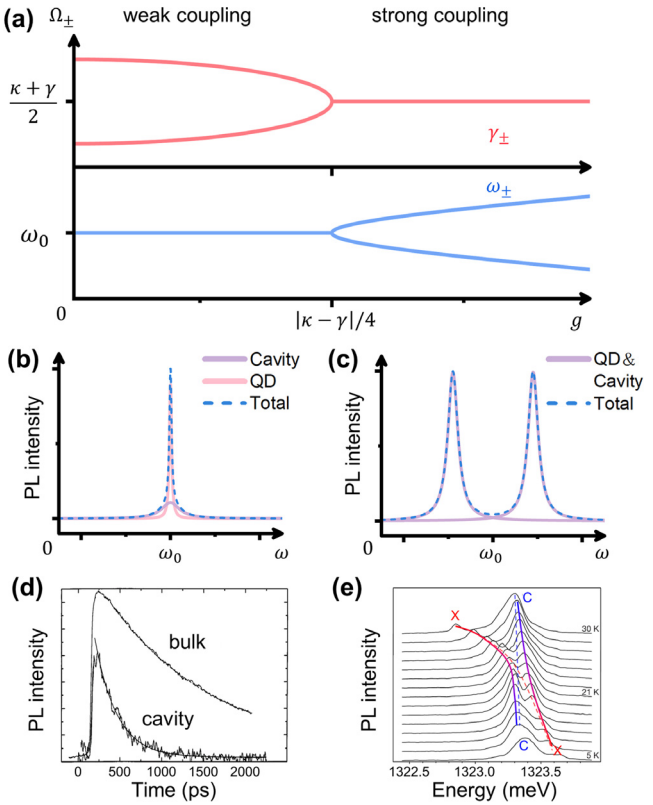

FIG. 13. Basic features of a coupled cavity–QD system. (a) Theoretical calculations of the eigenstates $\Omega_\pm$ when the cavity and the QD are at resonance. The upper panel shows the linewidth $\gamma_\pm$ (imaginary part), and the bottom panel shows the energy $\omega_\pm$ (real part). As the coupling strength g increases, the system evolutes from the weak coupling regime to the strong coupling regime with the threshold value $g = |\kappa - \gamma|/4$. (b) Normalized spectral profiles corresponding to the weak coupling regime, including the emission from the cavity branch (purple solid line), the QD branch (pink solid line), and the total spectrum (blue dashed line). The cavity branch and the QD branch have the same energy but different linewidths. (c) Normalized spectral profiles corresponding to the strong coupling regime. The eigenstates are polaritons as the hybridization of the cavity and the QD (purple lines). The distinct Rabi splitting between two polariton branches is clearly observed. (d) Time-resolved PL spectra illustrating the Purcell effect in the weak coupling regime. The decay rate of the QD emission is $\tau_d = 1.3$ ns when the QD is in bulk material while $\tau_d = 0.25$ ns when the QD is resonantly coupled to the cavity. Reproduced from Gerard *et al.*, Phys. Rev. Lett. **81**, 1110–1113 (1998); licensed under a Creative Commons Attribution (CC BY) license.[371] (e) Temperature-dependent PL spectra of the cavity–QD system in the strong coupling regime. Dashed lines denote the temperature-dependent shift of bare QD (red) and bare cavity (blue) without coupling. As the detuning changes, anticrossing behavior between the two polariton branches (solid lines) as the distinct feature of strong coupling is clearly observed. Reproduced with permission from Nature **432**, 197–200 (2004). Copyright 2004, Springer Nature.[372]

equation theory and present typical results with $\kappa = 10\gamma$ in Figs. 13(b) and 13(c). In Fig. 13(b), we present the result with $g = 9\gamma/16$, corresponding to the weak coupling regime. As shown, the two eigenstate branches have the same energy but different linewidths, consistent with the prediction in Fig. 13(a). In contrast, in Fig. 13(c), we present the result with $g = 9\gamma$, corresponding to the strong coupling regime. In this case, the two eigenstate branches have the same linewidth but different energies. This energy splitting between them is the well-known Rabi splitting, corresponding to the Rabi oscillation in the time domain. In recent years, some literature has also suggested that $g > (\kappa + \gamma)/4$ is a criterion for strong coupling. This is generally based on the coupled harmonic oscillator model in classical mechanics, in which the transition from weak coupling to strong coupling is a smooth change.[373,374] In contrast, in the quantum model shown in Eq. (1), the transition between the two regimes is sharp as discussed above. Although different conclusions arise from various models and perspectives used in the analysis, we emphasize that in most experimental works, the distinct feature for determining weak or strong coupling remains whether the Rabi splitting is obtained or not.

The cavity loss rate $\kappa = \omega_c/Q$ is proportional to the inverse of the quality factor Q. The coupling strength g for the QD under the dipole approximation is $\hbar g = |\mathbf{d} \cdot \mathbf{E}(\mathbf{r})|$, in which $\mathbf{d}$ is the dipole moment of the exciton, and $\mathbf{E}(\mathbf{r})$ is the local cavity electric field at the position $\mathbf{r}$ of the QD. The coupling strength g scales inversely with the square root of mode volume V as $g \propto 1/\sqrt{V}$, where $V = \int \epsilon(\mathbf{r})|\mathbf{E}(\mathbf{r})|^2 d^3\mathbf{r}/\max[\epsilon(\mathbf{r})|\mathbf{E}(\mathbf{r})|^2]$. The Purcell factor quantifies the enhancement of the spontaneous emission rate and is governed by the coupling strength g. By enhancing the spontaneous emission rate of QDs via the Purcell effect, decoherence processes can be suppressed, while the increased extraction efficiency leads to improved brightness. The Purcell factor at zero detuning between the cavity and the quantum emitter can be expressed as[375]

$$F_P = \frac{3}{4\pi^2}\left(\frac{\lambda}{n}\right)^3 \frac{Q}{V}\frac{|\mathbf{E}(\mathbf{r})|^2}{|\mathbf{E}_{max}|^2}\left(\frac{\mathbf{d}\cdot\mathbf{E}(\mathbf{r})}{|\mathbf{d}|\cdot|\mathbf{E}(\mathbf{r})|}\right)^2, \tag{5}$$

where λ is the wavelength of cavity and quantum emitter, n is the refractive index, and $\mathbf{E}_{max}$ is cavity electric field at the location of maximum electric field energy density (εE^2). From this, we can see that to increase the Purcell factor F_P or the coupling strength g, it is necessary to increase Q and decrease V. Additionally, F_P and g are also proportional to the degree of the overlap between the QD and maximum electric field energy density, as well as overlap of the exciton polarization and local electric field vector. Therefore, Q-factor and mode volume are the most commonly used parameters for evaluating the performance of cavities.[22] High Q-factor, small mode volume, along with the match of spatial position and dipole direction between the cavity and the QD is the key to improving the coupling strength and achieving the strong coupling regime.

The applications of weakly coupled cavity–QD systems are mainly based on the enhancement of the spontaneous emission rate of the QD, i.e., the Purcell effect.[376] In 1998, Gérard *et al.*[371] experimentally demonstrated the Purcell effect of QD in the cavity. As shown by the time-resolved spectra in Fig. 13(d), QD has the decay rate of $\tau_d = 1.3$ ns in the bulk material while that of $\tau_d = 0.25$ ns when resonantly coupled to the cavity, revealing a Purcell factor of 5. The applications of strong coupling mainly rely on the hybridized polaritons, which are quasiparticles that are half-light and half-matter excitations. In 2003, Yoshie *et al.*[377] and Reithmaier *et al.*[372] experimentally demonstrated the Rabi splitting in the cavity–QD system. As shown by the PL spectra in Fig. 13(e), the detuning between the cavity mode and the QD is controlled by the temperature. As the temperature increases, the cavity–QD system evolves from detuning to resonance and then detuning again, and PL peaks from the hybridized polariton branches (denoted by solid lines) with the anticrossing between them are clearly observed. Since then, the cavity–QD system has been widely investigated and improved for the study of cQED and their applications.[378]

B. Photonic cavities

Optical cavities confining photons in micro or nanoscale are the key to investigating cQED experimentally. Modern optical cavities exhibit a rich variety of architectures tailored for enhanced light–matter interaction. The DBR cavity is a well-known and widely applied optical cavity. It consists of a pair of one-dimensional PHCs at the top and bottom, which serve as a pair of mirrors to confine the photons. Micropillar cavity exemplified by GaAs/AlAs DBR structures, as shown in Fig. 14(a), is a typical DBR cavity and has been widely applied for III–V QDs. In the vertical direction, the periodic material layers with certain effective refractive index form one-dimensional PHCs at the top and bottom and reflect photons within the photonic bandgap. The photons are confined in the middle layer where the QDs are embedded. Other optical properties such as the resonant energy and mode volume can be controlled by the radius of the micropillar in the horizontal direction. The Q-factor of the micropillar cavity is mainly determined by the roughness of the sidewall.[386] After decades of optimization in the fabrication methods, the Q-factor of the micropillar cavity has been optimized to the ultrahigh regime, e.g., the value of around 2×10^5 has been achieved by Schneider *et al.*[379] in 2016.

In addition to the high Q-factor, the improvements of the DBR cavity mainly aim to achieve high controllability. For example, Tomm *et al.*[336] and Ding *et al.*[337] fabricated the open DBR cavity as schematically shown in Fig. 14(b), in which the top DBR mirror is freely movable. This allows the fine alignment of the position of QD in the DBR cavity. By evaporation of Au/Ti marks on the sample, we can precisely get the position of QDs from the map of PL spectroscopy, and the accuracy has been optimized to 15 nm in spatial and 0.4 nm in spectral.[387] Then the top DBR is aligned to ensure the QD is in the center of the DBR cavity as shown in the inset in Fig. 14(b). This maximizes the cavity–QD coupling strength because the cavity electric field has the maximum amplitude at the center. Meanwhile, the control of QD is also crucial for the cavity–QD system. External electric field applied from the top and bottom electrode gate is one of the conventional methods to control the QD. However, in the DBR cavity, the QD is deeply embedded in the center layer, and thereby, the electric field introduced by electrodes at the top and bottom of the DBR cavity has very weak effects on the QD. Somaschi *et al.*[25] solved this problem by adding four electrodes in the horizontal direction, as schematically shown in Fig. 14(c). In this case, the emission energy of QD is tuned by > 0.5 meV by adding the bias voltage 1.2 V, and the cavity–QD resonance is precisely achieved.

Two-dimensional slab PHC cavity is another type of optical cavity that has been widely applied for QDs, typically formed by introducing defects in the lattice of two-dimensional PHC. It confines photons by the photonic bandgap in the in-plane direction while by the total internal reflection in the out-of-plane direction. Compared to the DBR

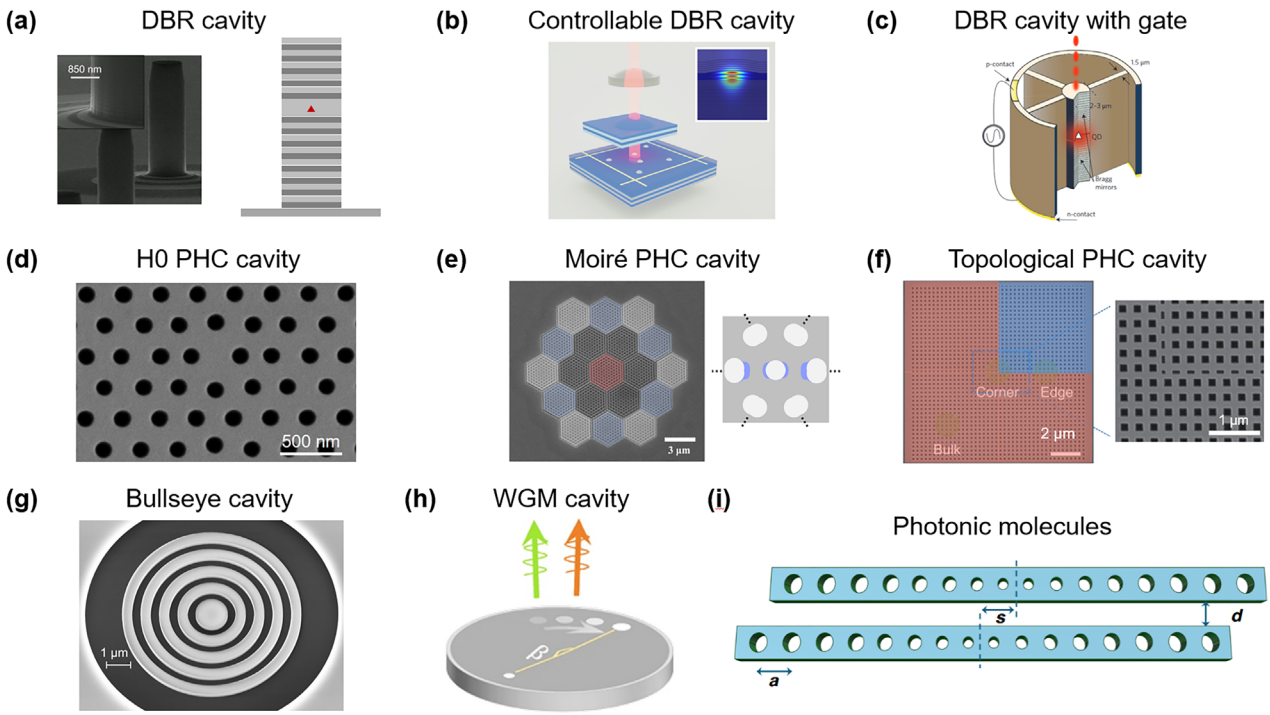

FIG. 14. Optical cavities for the investigation of QD-based cQED. (a) Typical micropillar DBR cavity. Reproduced with permission from Appl. Phys. B **122**, 19 (2016). Copyright 2016, Springer-Verlag Berlin Heidelberg.[379] (b) Open cavity with movable top DBR to control the cavity modes. Reproduced with permission from Nat. Photonics **19**, 387–391 (2025). Copyright 2025, Springer Nature.[337] (c) DBR cavity connected to a surrounding circular frame by four one-dimensional wires to apply external electric field. Reproduced with permission from Nat. Photonics **10**, 340–345 (2016). Copyright 2016, Springer Nature.[25] (d) H0-type PHC cavity. Reproduced from Ota *et al.*, Appl. Phys. Lett. **112**, 093101 (2018), with the permission of AIP Publishing.[380] (e) Moiré PHC cavity formed by superimposing two hexagonal lattices with a relative twist angle. Reproduced from Yan *et al.*, Nat. Commun. **16**, 4634 (2025); licensed under a Creative Commons Attribution (CC BY) license.[381] (f) High order topological PHC cavity. Reproduced from Xie *et al.*, Laser Photonics Rev. **14**, 1900425 (2020); licensed under a Creative Commons Attribution (CC BY) license.[382] (g) Highly symmetric bullseye cavity. Reproduced from Holewa *et al.*, Nat. Commun. **15**, 3358 (2024); licensed under a Creative Commons Attribution (CC BY) license.[383] (h) WGM cavity with non-Hermitian scattering. Reproduced from Yang *et al.*, Commun. Phys. **7**, 13 (2024); licensed under a Creative Commons Attribution (CC BY) license.[384] (i) Photonic molecule consisting of two coupled nanobeam cavities. The new degrees of freedom including the gap *d* and shift *s* in the photonic molecule improves the controllability with the full polarization control. Reproduced from Zhu *et al.*, Light Sci. Appl. **14**, 114 (2025); licensed under a Creative Commons Attribution (CC BY) license.[385]

cavity, PHC cavity greatly decreases the mode volume to the wavelength scale $V \sim (\lambda/n)^3$, i.e., the regime of nanocavity. Moreover, PHC nanocavity has high design flexibility and can be directly integrated in the on-chip PHC circuit. Typical defect profiles of the PHC cavity mainly include the H0, H1, and L3 cavity corresponding to the different defect profiles.[388,389] For example, Fig. 14(d) shows an optimized H0 cavity, which means no nanohole is removed, but the two nanoholes at the center are mainly adjusted to form the photon confinement with surrounding holes modified to improve the Q-factor. Recently, the defect profiles have been further optimized for subwavelength mode volume, such as the L4/3 cavity having $V \sim 0.32(\lambda/n)^3$ and the H0 cavity having $V \sim 0.25(\lambda/n)^3$ generated from the automated optimization method.[390,391] The subwavelength scale is expected to achieve high-efficiency modulation of photons and provide the basis for novel cavity–QD coupling phenomena.

In addition to the conventional H-series and L-series defect profiles, PHC cavity has been developed with other types of photon confinements. Figure 14(e) shows the moiré PHC cavity, which is a combination of two PHC crystal layers with a twist angle between them. This results in the periodic moiré superlattice and optical modes with high Q/V ratio in theory.[392] When the twist angle is "magic," each moiré site becomes uniform. Such moiré cavities have recently been demonstrated to enhance the single-photon emission of the QD.[381,393] Topology is another method to form the cavity photonic mode. Generally, the boundary between two PHCs with different topology can generate edge states and confine the photons with the topological protection.[394] The line boundary usually supports the waveguide mode, while the corner boundary supports the confined photonic mode. Xie *et al.*[3,382] achieved the lasing and Purcell effect with the QD using the topological corner state, as shown in Fig. 14(f). Owing to the high design flexibility of PHC cavity, we would expect more new types of PHC cavity in the future.

The controllability of a single PHC cavity is limited by the geometry design, e.g., the far-field polarization of the cavity mode is usually linear due to the breaking of rotational symmetry and is difficult to control. Specific cavities have been developed for the circular polarization, which can be applied for the coupling with both two single exciton states of the QD.[380] For example, the bullseye cavity (or called

CBG) as shown in Fig. 14(g) has the PHC structure in the radial axis while it is uniform in the polar angle axis, resulting in highly degenerate modes that allow the circular polarization.[383] In 2021, Fong *et al.*[395] achieved the circularly polarized cavity mode in an H1 PHC cavity based on the non-Hermitian coupling between two cavity modes. The non-Hermiticity leads to the supermode of two linearly polarized modes with an imaginary phase shift, which means the circular polarization. In 2024, Yang *et al.*[384] introduced defects with different sizes in the whispering gallery mode (WGM) cavity, as shown in Fig. 14(h). The well-designed defects result in the asymmetric backscattering and the non-Hermiticity, and a controllable polarization including ellipse states is achieved by controlling the position of defects near the exceptional point.

Compared to a single PHC cavity, photonic molecules consisting of coupled cavities provide controllability in more degrees of freedom, which greatly improves the controllability of the cavity mode. The coupling between two cavities in the photonic molecule is usually described by the coupled mode theory in the Hermitian regime, and the coupling strength is controlled by the spatial distance between them.[396] Recently, Zhu *et al.*[385] fabricated the photonic molecule consisting of two 1D PHC nanobeam cavities with an ultra-subwavelength gap between them, as shown in Fig. 14(i). In this photonic molecule, the coupling between two cavities is dominated by the evanescent wave and exhibits strong non-Hermitian features. The non-Hermiticity allows the non-trivial phase in the supermodes, enabling the full far-field polarization control of the cavity mode from linear to circular polarization. These novel optical modes demonstrate the potential of integrated optical cavities in the applications of non-trivial quantum photonic devices.

If one aims to pursue an ultrasmall mode volume, bowtie-type cavities can be considered.[397–399] These cavities with extreme dielectric confinement are capable of compressing light into volumes far below the diffraction limit. In 2022, Albrechtsen *et al.*[398] demonstrated, for the first time, photon confinement inside dielectrics below the diffraction limit, without intrinsic limitations on the Q-factor. However, whether such structures can be successfully implemented in QD systems remains a question, given that the gap between the two dielectric elements is only a few nanometers—smaller than the typical diameter of self-assembled QDs.

Overall, to achieve the cavities with the higher Q-factor and smaller mode volume, PHC cavities have been developed by the optimization of defect profile designs and nanofabrication technologies. In the early stage, the defect profile of the PHC cavity is usually optimized by tuning only a few nearby nanoholes, such as the shift of two nearest nanoholes in the L3 PHC cavity that increases the Q-factor to over 10^4 for a reduced optical leakage.[388] Recently, automated optimization approaches have been utilized, which can simultaneously optimize multiple parameters of multiple nanoholes to improve the Q-factor and maintain the small mode volume of the cavity.[391,400] In experiments, the fabrication-induced imperfections will introduce structure interface roughness and thereby the optical scattering or absorption loss, degrading the cavity performance. The post-treatment after the etching process can be employed, considering the generally used e-beam lithography and subsequent dry etching techniques. Conventionally, ammonia was applied to passivate the surface of optical cavities.[401] In 2020, Kuruma *et al.*[402] developed the sulfur-based surface passivation technique using a Na_2S solution. This method further improves the Q-factor of PHC cavities to 1.6×10^5. Moreover, the alignment between the cavity field maximum and single QD in space has been improved. Using the luminescence spectroscopy method[387,403] similar to that in Fig. 14(b), along with the *in situ* lithography,[404–406] the spatial mismatch between the cavity and the QD can be suppressed to <10 nm in recent years.

C. Quantum devices and applications

Weak Coupling: The weak coupling regime leads to the Purcell effect of the QD. As shown in Fig. 15(a), compared to the bare QD, the cavity modulates the local optical field, which enhances the emission rate. This enhancement filters the background emissions such as the phonon sideband or other nearby QDs, optimizing the spectral and spatial profiles in the emission of the QD. The Purcell-enhanced SPS has enabled single photons with high purity [low $g^{(2)}(0)$], high indistinguishability H_{VOM}, and high brightness. The experimental challenge of the SPS is mainly the photon extraction efficiency and the noise that introduces dephasing effects. In 2016, Somaschi *et al.*[25] fabricated SPS using the micropillar cavity with gate [discussed in Fig. 14(c)] and improved the performance through the resonant excitation. As shown in Fig. 15(b), they tuned the emission energy of the QD by the Stark effect and achieved the cavity–QD resonance. The controllable external electric field through the gate also helps to suppress the charge noise. Moreover, they investigated the performance of SPS using different excitation conditions. When the excitation laser is non-resonant, the purity is $g^{(2)}(0) = 0.024$, and the indistinguishability is $H_{VOM} \sim 70\%$. In contrast, when the excitation laser is resonant to the cavity–QD system, the purity is improved to $g^{(2)}(0) = 0.0028$, and the indistinguishability is improved to $H_{VOM} \sim 99.56\%$.

The major challenge in the resonant excitation is filtering of the excitation laser. In free space, the filtering is usually based on the polarization. The direct implementation of polarizers leads to a 50% loss of brightness, while the utilization of polarization-diverse mode-splitting cavities provides an effective solution to this problem.[344,409,410] The optical waveguide embedded with single QDs also enables the on-chip routed SPS[334,411–413] and other possible resonant filtering schemes. In 2020, Uppu *et al.*[407] applied a similar method to the on-chip integrated nanophotonic circuit. As shown in Fig. 15(c), they used a planar nanophotonic structure consisting of two waveguide modes. The excitation employs a higher-order mode, which will suffer losses in the subsequent taper section and bend. The leakage of the excitation laser into the collection channel is theoretically calculated as $\sim 10^{-4}$ and experimentally measured as $\sim 10^{-3}$. The high-efficiency separation between excitation and collection allows the on-chip resonant excitation, enabling guided single-photon emission with high purity and high indistinguishability as $g^{(2)}(0) \sim 0.02$ and $V_{HOM} = 96\%$. In addition, the coupling efficiency between the QD and the waveguide mode is also investigated. As shown in the bottom panels in Fig. 15(c), the coupling efficiency is improved to >80% when the QD is at the center of the waveguide, and the coupling efficiency slowly decreases as the QD position offset increases. Meanwhile, owing to the high-efficiency filtering through waveguide modes, the impurity contributed by the excitation laser is always $<10^{-2}$. However, the efficiency of filtering based on the polarization cannot reach 100 %, and the existence of re-excitation for the cavity–QD system will degrade the purity of SPS. Methods such as the TPE[350,414] and two-color excitation[261,415] have been developed to further solve these problems, as discussed in Sec. IV.

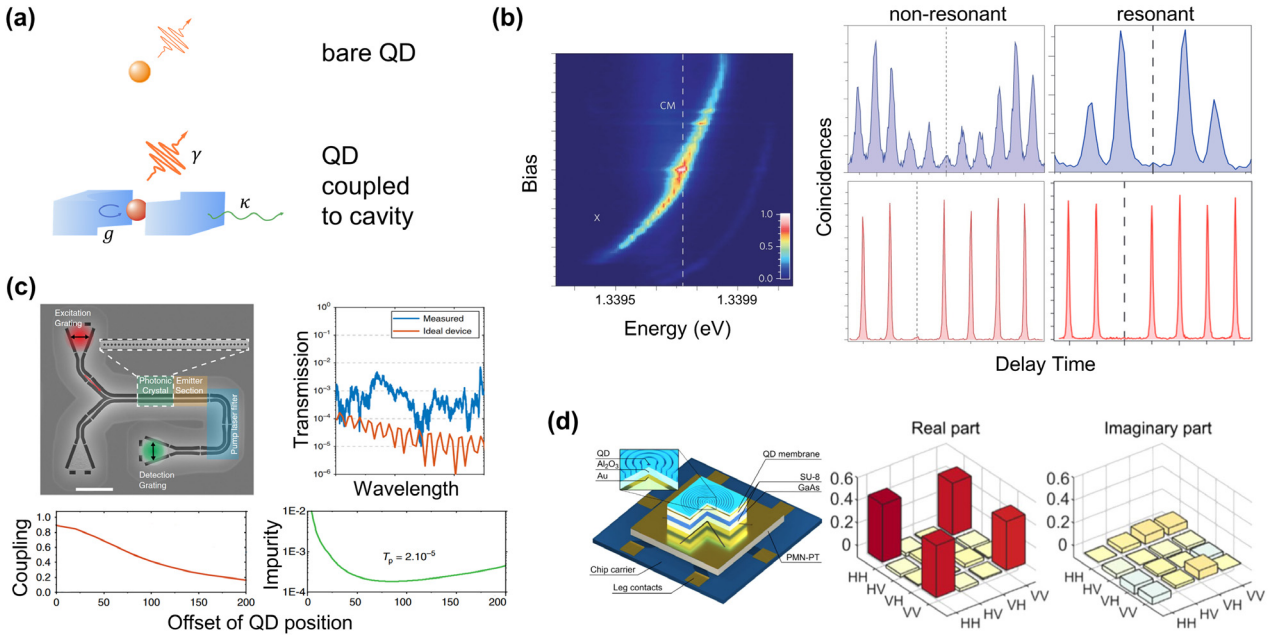

FIG. 15. Single-photon and entangled photon sources. (a) Schematic illustration of cavity–QD SPS system. Compared to the bare QD (top), the Purcell effect in the weakly coupled cavity–QD system (bottom) enhances the emission rate and improves the SPS performances. (b) Micropillar SPS. Left panel shows the emission intensity as a function of bias and energy. The energy of exciton (X) is tuned to the resonance with the cavity mode (CM) by the Stark effect, as denoted by the dashed line. Right panel shows the correlation histograms measuring the indistinguishability V_{HOM} of photons (blue) and the second-order autocorrelation of photons (red) at the low excitation power. The measurement was implemented at both the non-resonant and resonant excitation conditions. The performance of SPS is greatly improved when the excitation laser is resonant to the cavity–QD system. Reproduced with permission from Nat. Photonics **10**, 340–345 (2016). Copyright 2016, Springer Nature.[25] (c) SPSs integrated on-chip. Top left panel is the SEM image of the fabricated device. Top right panel shows the measured and calculated transmission T_p spectrum of the excitation laser, which is filtered by the polarization of two orthogonal waveguide modes. After filtering, the transmission is around $10^{-4} - 10^{-3}$. Bottom panels show the calculated coupling efficiency for the waveguide mode and expected single-photon impurity contributed by the excitation laser as a function of the offset of QD position from the waveguide center. Reproduced from Uppu *et al.*, Nat. Commun. **11**, 3782 (2020); licensed under a Creative Commons Attribution (CC BY) license.[407] (d) Entangled photon sources. Left panel shows the device structure. Right panels display the reconstructed density matrix at the highest fully entangled fraction of the QD. Reproduced from Rota *et al.*, eLight **4**, 13 (2024); licensed under a Creative Commons Attribution (CC BY) license.[408]

Overall, a good SPS should possess the following key aspects: (i) high controllability with deterministic integration of QDs in the cavity to maximize complete coupling between QDs and the cavity; (ii) noise reduction and proper excitation scheme to enhance indistinguishability and purity; and (iii) improved brightness for on-demand operation with large Purcell enhancement and optimized resonant filtering methods. The latest progress in open microcavity-based SPSs integrates all these aspects, representing the currently best comprehensive performance.[336,337,416] Among them, in 2025, Ding *et al.*[337] reported an SPS system with an system efficiency of 0.712, $g^{(2)}(0) = 0.0205$, and $H_{VOM} = 98.56\%$. For a comprehensive comparison, the parameters of other high-performance SPSs are summarized in Table II. Here, the system efficiency refers to the end-user efficiency, which includes the total contributions from all loss channels, including the optical path losses, device extraction efficiency and excluding the detection efficiency of the single-photon detectors. Due to the relatively mature growth technology and the favorable overall performance of QDs emitting near 900 nm, representative works of reported QD-based SPSs in this wavelength range are mainly summarized in Table II. At the same time, progress has also been achieved in studies operating at other wavelengths.[413,417,422–424] For instance, a $g^{(2)}(0)$ value as low as 0.012 has been realized in the telecom O-band.[420]

The biexciton state XX^0 of the QD allows the cavity–QD system for more possible applications. For example, XX^0 can directly emit two identical photons with the cavity interaction. In 2011, Ota *et al.*[425] found that when the cavity has the energy $\omega_c = (\omega_{X^0} + \omega_{XX^0})/2$, the two-photon emission is enhanced along with the suppression of one photon emission. In 2018, Qian *et al.*[100] further demonstrated that when the cavity–QD coupling increases above a threshold, such enhancement of two-photon emission (weak coupling) will evolve to the two-photon Rabi splitting (strong coupling), resulting in a two-photon process. Such two-photon emission introduces the bright nonlinear radiation into the quantum photonic technologies.[343] In addition to the two-photon emission, the biexciton state XX^0 can also emit a pair of entangled photons mediated by X^0, as discussed in Sec. IV. The Purcell effect from the cavity can also enhance the cascaded optical transitions,[24,426–429] but the challenge is how to simultaneously enhance both transitions with different energies ω_{XX^0} and ω_{X^0}. In 2024, Rota *et al.*[408] used a low-Q ($Q \sim 100$) bullseye cavity to enhance the EPS, as shown in Fig. 15(d). Owing to the low Q-factor, the linewidth of the cavity mode is very large and results in the broadband enhancement over tens of nm of wavelength, covering both the two transitions having the energies ω_{XX^0} and ω_{X^0}. This improves the purity and indistinguishability of the pair of photons, and thereby, improves

TABLE II. Comparison of QD SPSs.

Cavity type	Wavelength (nm)	Q-factor	Purcell factor	$g^{(2)}(0)$	Indistinguishability	System efficiency	Specialized techniques
Open cavity[337]	**885**	8400	17 (2)	0.0205 (6)	0.9856 (13)	0.712 (18)	Shaping system
Open cavity[416]	**915**	8054	9	0.044 (2)	0.922 (4)	0.129	Strain tuning
Circular Bragg grating[417]	**1545**	183	6.7 (6)	0.057 (4)	···	···	p-shell pumping
Micropillar[345]	**906**	7540	6.6	0.002 (1)	0.926 (4)	0.03 (2)	TPE with stimulating lasers
Micropillar[418]	**925**	4000	···	0.046 (1)	0.909 (4)	0.107	Phonon-assisted excitation
Open cavity[336]	**920**	12 600	12	0.021 (1)	0.975 (5)	0.575 (30)	Gated QDs
Microring[419]	**900**	···	2	0.115 (1)	···	0.0078	Carry orbital angular momentum
Circular Bragg grating[420]	**1300**	130	4.0 (7)	0.0115 (2)	···	0.014	p-shell pumping
Elliptical micropillar[344]	**897**	5016	17.8	0.025 (5)	0.975 (6)	0.237	Polarization-orthogonal excitation–collection
Elliptical Bragg grating[344]	**890**	181	15.7	0.009 (3)	0.951 (5)	0.215	
Circular Bragg grating[24]	**772**	150	3.5	0.001 (1)	0.901 (3)	0.082	π-pulse TPE
Micropillar[261]	**900**	1000	···	0.012 (1)	0.962 (6)	0.055	Two-color excitation
H1 cavity[26]	**915**	765	43 (2)	0.026 (7)	0.939 (33)	···	π-pulse excitation, on-chip
Micropillar[25]	**925**	12 000	7.6	0.0028 (12)	0.9956 (45)	0.012[a]	Electrically controlled
Micropillar[421]	**898**	6124	6.3 (4)	0.009 (2)	0.985 (4)	0.138	π-pulse excitation

[a]This value was obtained using a SPAD characterized by a detection efficiency of 0.4.

the entanglement up to 96%. Therefore, for EPSs, a high cavity Q-factor is not required. If the cavity exhibits an excessively high Q-factor, it can no longer provide simultaneous enhancement of the two transitions. In practice, a Q-factor of approximately $\sim 10^2$ is appropriate for EPSs and sufficient to achieve Purcell enhancement.

Other applications of the weakly coupled cavity–QD system mainly focus on the enhanced quantum state manipulation based on the Purcell effect. The quantum state of the QD can be driven by the pulsed resonant excitation laser, as discussed in the context of Sec. V C. In 2013, Carter *et al.*[430] used the L3 PHC cavity under resonant excitation. The optical initialization and readout processes of the QD spin are realized, where the Purcell effect from the cavity mode greatly enhances the rate of these two processes. The device structure and the Ramsey fringe of the cavity coupled QD system relating the pulse power are shown by the Fig. 16(a). In 2023, Antoniadis *et al.*[431] used the Purcell effect to improve the collection efficiency of photons and shorten the readout time of QD spin to 3 ns, as shown in Fig. 16(b). Owing to the rapid readout time, errors resulting from measurement-induced back-action were suppressed. This readout time is also below the spin relaxation and dephasing times, and thereby suppressing the noise from these two effects. The fidelity of the quantum state operation is improved to 95.2%. In 2024, Mehdi *et al.*[432] further used such Purcell enhancement to suppress the noise from experimental fluctuations such as birefringence. Combined with the external magnetic field, the enhanced light–matter interaction allows most conditional rotations in the Poincaré sphere with a control both in longitude and latitude, as shown in Fig. 16(c). Specifically, by tuning the laser frequency and the magnetic field strength, the two electron spin states can be selectively addressed, thereby enabling precise control over the polarization state of the output light. These works reveal that even in the weak coupling regime, the Purcell effect can enhance the rate of quantum operations and allow for high-fidelity state manipulation on the QD, which is crucial to apply the spin–photon interfaces for quantum information processing. In addition, the cavity–QD system also enables the study of novel single-photon emission carrying with orbital angular momentum[419] and degenerated cavity modes featuring skyrmionic characteristics recently.[433]

Strong coupling: The investigation of strongly coupled cavity–QD system imposes stringent requirements on both cavity quality and light–matter coupling strength. Achieving this regime necessitates precise spectral tuning with a large spatial overlap between the QD dipole and cavity field maximum. To date, distinct Rabi splitting has been widely observed in the cavity–QD system based on micro-disk cavity,[439] DBR-based cavity[440,441] and photonic crystal cavity.[442–445] In 2006, Hennessy *et al.*[434] investigated the cavity–QD system involving only a single cavity and a single QD verified by AFM spectroscopy and time-correlation spectroscopy. As shown in Fig. 17(a), the AFM image shows that there is only one QD at the nearly central position in the L3 PHC cavity. The central position corresponds to the antinode of the cavity electric field, which enhances the cavity–QD coupling strength. Moreover, they performed the time-resolved measurements to further probe the underpinning physics. When the cavity and QD are off resonance, photon emission from the cavity mode and the QD is anti-correlated at the level of single quanta. This demonstrates that even when off-resonance, the cavity mode is driven solely by the QD despite the energy mismatch, and there is no other nearby QD within the cavity mode volume. In such a system, the Rabi splitting is clearly observed as shown in the right panel in Fig. 17(a). When the cavity is tuned to resonance, the lifetime of the QD reduces by a factor of 145, and the generated photon exhibits the antibunching feature with $g^{(2)}(0)$ decreased by half compared to the off-resonant case. These results clearly demonstrate that the strongly coupled cavity–QD system is in the quantum regime, providing the basis for the applications in quantum photonic technologies.

The coupling strength g is a key parameter of the cavity–QD system that determines the coherence time and fidelity of the spin–

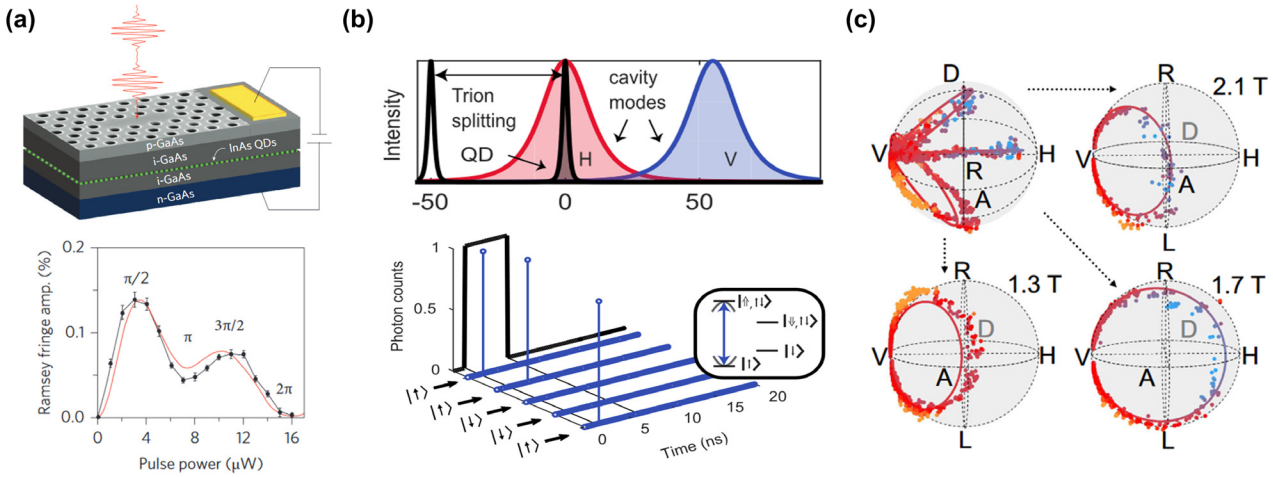

FIG. 16. Quantum state manipulation enhanced by the Purcell effect. (a) Quantum control of a spin qubit. Top panel shows the device architecture. Bottom panel displays the fitted amplitude of Ramsey interference fringes as a function of pulse power. The operation rate is enhanced by the Purcell effect. Reproduced with permission from Nat. Photonics **7**, 329–334 (2013). Copyright 2013, Springer Nature Limited.[430] (b) Single-shot readout of a QD spin. Owing to the resonant cavity mode, the readout time is shortened to 3 ns. This is faster than the relaxation and dephasing times, resulting in a high fidelity of 95.2 %. Reproduced from Antoniadis *et al.*, Nat. Commun. **14**, 3977 (2023); licensed under a Creative Commons Attribution (CC BY) license.[431] (c) Quantum state control in the Poincaré sphere. Combining the cavity enhancement and the external magnetic field, the spin state of the QD can be controlled arbitrarily in the Poincaré sphere, including the left and right circular polarization (R and L), the horizontal and vertical linear polarization (H and V), and the diagonal and antidiagonal polarization (D and A). Reproduced from Mehdi *et al.*, Nat. Commun. **15**, 598 (2024); licensed under a Creative Commons Attribution (CC BY) license.[432]

photon interface. Increasing the coupling strength g accelerates the energy exchange between the photon and exciton, enhancing the gate speed and reducing the effects of decoherence processes. Because the interface operation occurs faster than the system dissipation, the quantum information is transferred before being lost due to cavity decay or decoherence, thereby improving the fidelity. As mentioned above, g influences the Purcell factor, thus affecting the performance of SPSs. Photon blockade, single-photon switches, transistors, and many nonclassical effects also have strength proportional to g. Furthermore, a larger g value improves tolerance to spectral detuning and device imperfections, thereby enhancing the robustness and scalability of solid-state quantum photonic systems. Thus, the control and enhancement of g are long-standing topics for the cavity–QD system. One potential method is to increase the number of excitons or cavity modes. For example, in 2018, Ota *et al.*[380] used the H0 cavity for the coupling with the QD. Owing to the fact that the H0 cavity has two degenerate cavity modes that can couple to different polarization states of QD, the cavity–QD coupling strength g is theoretically enhanced by a factor of $\sqrt{2}$ and experimentally reaches the value of 165 μeV. However, the enhancement of g between a single QD and a single cavity mode remains a challenge. For example, in 2009 and 2010, Reitzenstein *et al.*[446] and Faraon *et al.*[447] controlled the cavity–QD coupling using the external magnetic and electric fields, respectively. As the magnetic field or electric field increases, the dipole moment of the exciton in the QD decreases, along with the decreasing coupling strength g to the cavity mode. These methods enable the changing from the strong coupling regime to the weak coupling regime but cannot enhance the coupling strength g. To solve this problem, in 2019, Qian *et al.*[435] investigated the cavity–QD system by applying the p-shell excitons.

As shown in Fig. 17(b), the emission spectrum of the ensemble of QDs involves three peaks, corresponding to the s-shell, p-shell, and d-shell excitons with the peak energy from low to high, respectively. The s-shell exciton has a small wavefunction extent that follows the dipole approximation, i.e., the local cavity electric field is approximately uniform. In this regime, the cavity–QD coupling strength g is separately determined by the amplitude of the local cavity electric field $\mathbf{E}(\mathbf{r})$ and the dipole moment of the exciton $\mathbf{d}$ as $\hbar g = |\mathbf{d} \cdot \mathbf{E}(\mathbf{r})|$ as discussed above. Thus, the decrease in the dipole moment results in the decrease in g, as reported by Reitzenstein *et al.*[446] and Faraon *et al.*[447] In contrast, the p-shell exciton has a large wavefunction extent in spatial.[448] As such, the local cavity electric field $E(r)$ is no longer uniform when the exciton is at different positions. In this nonlocal regime, the coupling strength g is determined by the intertwining of cavity and dot degrees of freedom as $\hbar g = \int \psi(r)E(r)dr$, in which $\psi(r)$ is the center-of-mass wavefunction of the p-shell exciton.[449] The dependence of the coupling strength g on the exciton wavefunction extent (dipole moment) is presented as the gray line in the bottom left panel in Fig. 17(b). As the exciton wavefunction extent (dipole moment) is decreased by the magnetic field, g for the s-shell exciton follows the prediction of the dipole approximation and monotonically decreases, but g for the p-shell exciton shows a non-trivial tendency along with a maximum g as the wavefunction extent changes. In experiments, the external magnetic field is applied in a Faraday configuration to shrink the exciton wavefunction extent, and the experimentally observed coupling strength g perfectly agrees with the theoretical prediction. With the magnetic field of 3.5 T, the maximum g of 210 μeV is achieved, which is also the largest value ever reported for the coupling between the PHC cavity and the QD. These results indicate that the new excitonic states are the key to further exploring and developing the physics of the QD-based cQED.

The applications of strongly coupled cavity–QD systems are mainly based on the coherent coupling, i.e., the quantum information

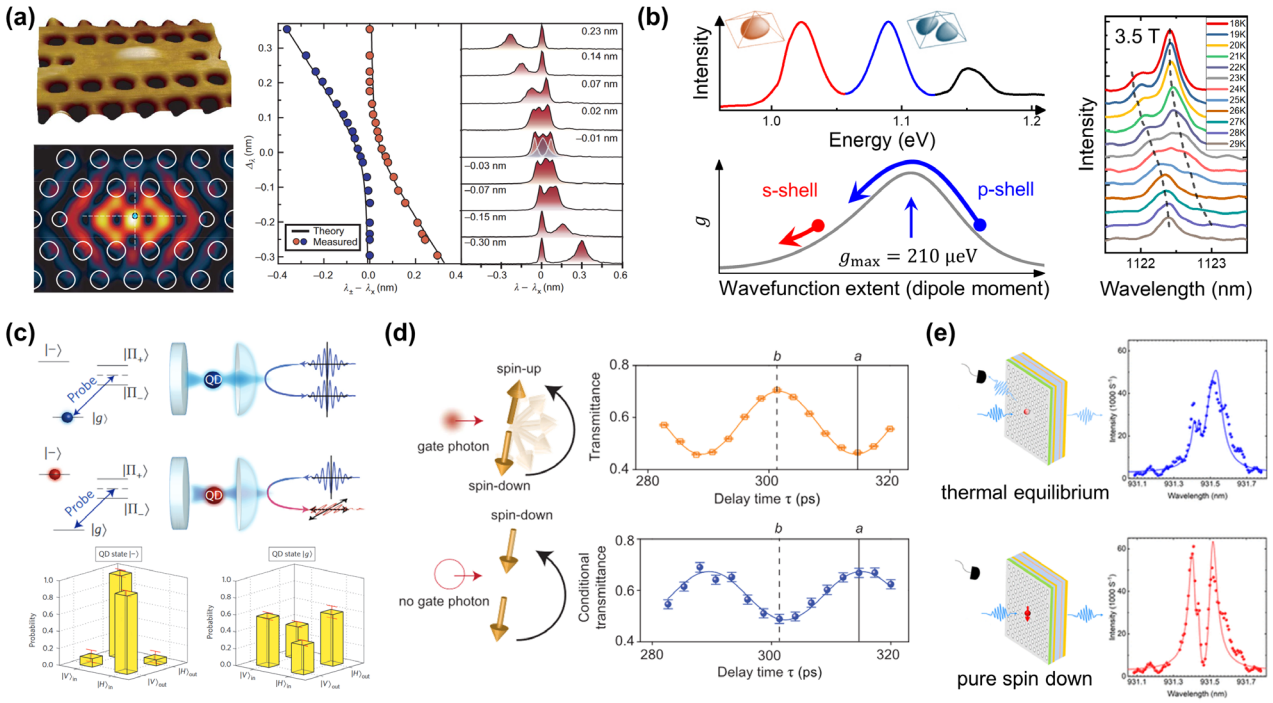

FIG. 17. Cavity–QD strong coupling and applications. (a) The system with a single cavity and a single QD verified by AFM spectroscopy and time-correlation spectroscopy. Left panels shows the spatial distribution of the cavity electric field in the L3 PHC cavity, as well as the position of QD detected by the AFM spectroscopy. Right panels display the distinct anticrossing behavior in the strong coupling regime. Reproduced with permission from Nature **445**, 896–899 (2007).Copyright 2007, Springer Nature.[434] (b) Enhanced coupling strength through *p*-shell exciton. Left top panel presents the spectra of ensemble QDs at high excitation power, in which the multiple peaks corresponding to multiple energy levels of the QD. Left bottom panel shows that due to the large wavefunction extent, the p-shell–exciton–photon coupling is beyond the dipole approximation. As the wavefunction extent shrinks, the coupling strength is first enhanced and the suppressed. The maximum coupling strength g between the cavity and the p-shell exciton is 210 μeV, and the corresponding raw PL spectra are shown in the right panel. Reproduced from Qian *et al.*, Phys. Rev. Lett. **122**, 087401 (2019); licensed under a Creative Commons Attribution (CC BY) license.[435] (c) A QD-photon cNOT operation. Upper panel illustrate the cNOT operation. Lower panel presents the measured state probabilities $P_{a\to b}$ for QDs in excited and ground state configurations. Reproduced with permission from Nat. Photonics 7, 373–377 (2013). Copyright 2013, Springer Nature.[436] (d) All-optical switching via spin control. Left panel shows the schematic of the working principle of the single-photon switch and transistor. In the first step, a gate photon controls the state of the spin. In the second step, the spin determines the polarization of the signal field. Right panel displays the conditional transmittance as a function of delay time τ between spin rotation pulses, with (orange circles) and without (blue circles) gate field detecting. Reproduced from Sun *et al.*, Science **361**, 57–60 (2018); licensed under a Creative Commons Attribution (CC BY) license.[437] (e) Spin-dependent cavity reflectivity within a charge tunable device. The resonant reflection spectrum of the cavity dot system in the thermal equilibrium condition (top panel) and pure spin down condition (bottom panel). Reproduced with permission from Nano Lett. **19**, 7072–7077 (2019). Copyright 2019, American Chemical Society.[438]

exchanging at the spin–photon interface, where the spin is controlled through optical, magnetic-field, or electrical tuning schemes, enabling conditional manipulation of both the spin state and the photonic polarization. For example, Kim *et al.*[436] demonstrated a cNOT quantum gate through the strongly coupled cavity–QD system. They found that the reflectivity of a photon emitted to the cavity is determined by the polarization of the photon and the state of the QD. As shown in Fig. 17(c), when the QD is in the ground state, the polarization of the incident photon is preserved. In contrast, the polarization of the incident photon is rotated when the QD is in the excited state. By using the pump-probe setup, they achieved a cNOT gate based on the polarization of the incident photon. Based on the same principle, Sun *et al.*[437] introduced a third gate pulse between the pump and probe pulse and achieved the single-photon switch, as shown in Fig. 17(d). Similar to the weak coupling system, experimental fluctuations such as charge noise are the major challenge in the applications of strong coupling systems. In 2019, Luo *et al.*[438] investigated the strong coupling between the cavity and the negatively charged state of the QD. They found that when the system is in the thermal equilibrium state, the random charging from nearby impurities leads to instability in the charge state and causes poor contrast in the cavity reflectivity, as shown in Fig. 17(e). They used a diode structure to deterministically charge the QD and initialize the spin through optical pumping. This results in a strong spin-dependent modulation of the cavity reflectivity, corresponding to a cooperativity of 12 in contrast to the value of 2 reported previously.[450–452] Further suppression of these noises would be an important topic in the study of the cavity–QD coupling system, where the surface passivation offers a viable path.[83,85] In addition, the anharmonic energy levels of Jaynes–Cumming ladders in the strongly coupled system enable the non-classical photon generation including the photon blockade and the photon-induced tunneling[453–455] and ultra-fast optical switching.[456]

VI. ON-CHIP INTEGRATION

With the rapid progress of quantum information technology, the significant miniaturization of quantum devices has become an urgent requirement.[457] Achieving on-chip integration of QD-based photonic devices has emerged as a critical technological pathway for constructing scalable quantum photonic systems. A complete on-chip quantum optical circuit encompasses quantum light sources, waveguides, beam splitters, phase shifters, filtering and selection devices, detectors, and other essential components.[458] While such comprehensive integration remains an ideal and ultimate objective, the integration of individual components is progressing steadily, and there have also been some attempts at small-scale on-chip integration for specific applications.[459] This chapter will first introduce work related to on-chip waveguides, then introduce some on-chip integration technologies and current progress.

A. Nanophotonic waveguides

Waveguides can connect different QDs through the photons propagating in the waveguide modes, which are the basic components of a scalable integrated optical quantum network exploiting the quantum interface.[466] As shown in Fig. 18(a), multiple kinds of waveguides in the 2D slab PHC, enabling dispersion engineering with various geometric parameters, have been developed, including the W1 waveguide, the glide-plane waveguide, and the valley-Hall waveguide. In addition, a simple nanobeam without any nanostructures is also a kind of waveguide, confining photons through total internal reflection, like the

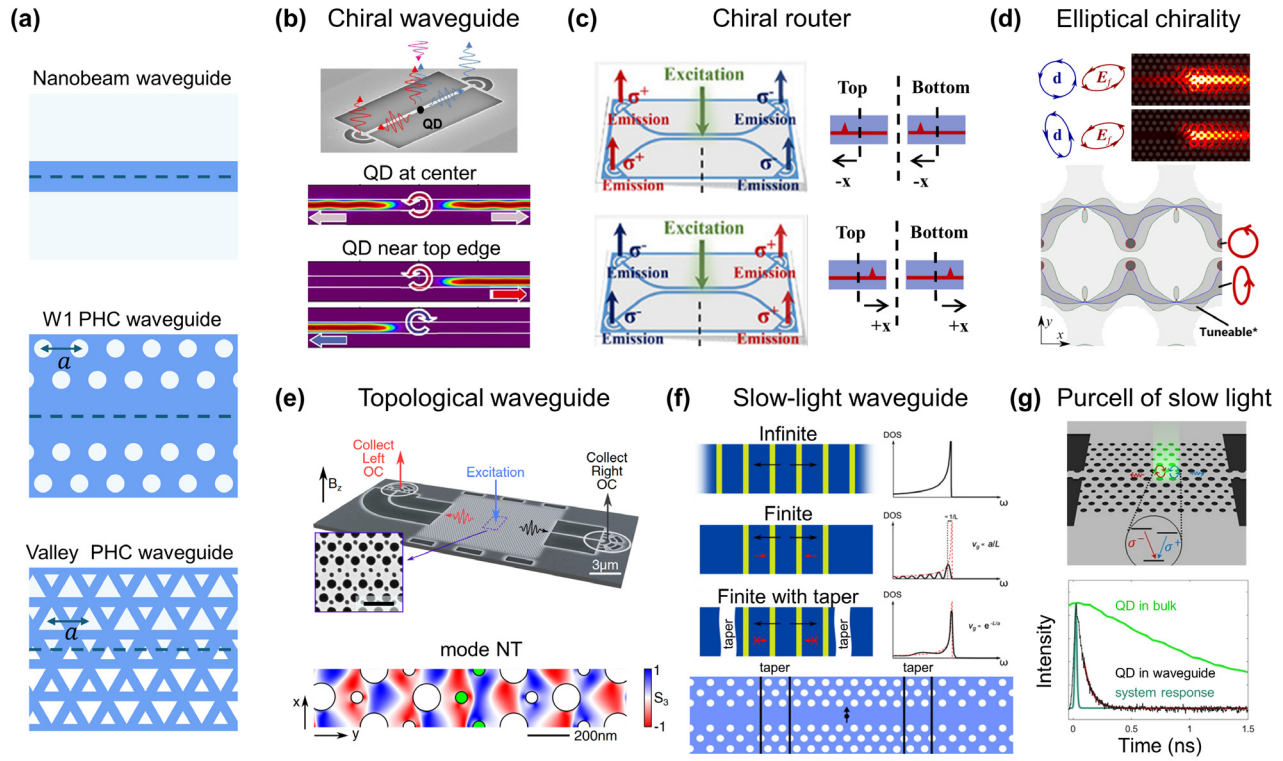

FIG. 18. Nanophotonic waveguides coupled with QDs exhibiting chiral and slow light features. (a) Schematic of the waveguide structures, including the bare nanobeam waveguide, the W1 PHC waveguide, and the valley-Hall (VH) PHC waveguide. (b)–(d) Waveguides with chirality. (b) Demonstration of chiral effects in the nanobeam system. Top panel shows the SEM image of the waveguide-QD device. Middle panel shows the case when the QD is at center. In this case, no chirality is observed. Bottom panels show the case when the QD is near the top edge. In this case, the right circular emission propagates right, and the left circular polarized emission propagates left, showing the chiral behavior. Reproduced from Coles *et al.*, Nat. Commun. **7**, 11183 (2016); licensed under a Creative Commons Attribution (CC BY) license.[460] (c) Chiral router based on coupled waveguides. Top and bottom panels correspond to the cases where the QD located in the $+x$ direction (left panel) and $-x$ direction (right panel) off-center are excited. Reproduced from Xiao *et al.*, Laser Photonics Rev. **15**, 2100009 (2021); licensed under a Creative Commons Attribution (CC BY) license.[461] (d) Chiral behavior based on elliptical polarizations. Top panel is the simulation results for circular and elliptical polarization emitter within the waveguide structure. Bottom panel denotes the effective area of the QD that exhibits the chirality. As shown, the effective area for the elliptical polarization (light gray area) based chirality is much larger compared to that for the circular polarization (darkest area) based chirality. Reproduced from Lang *et al.*, Phys. Rev. Lett. **128**, 073602 (2022); licensed under a Creative Commons Attribution (CC BY) license.[462] (e) SEM image of a topological valley waveguide and the normalized Stokes parameter S_3 of the non-trivial waveguide mode indicating the effective region for chiral interaction. Reproduced from Mehrabad *et al.*, Optica **7**, 1690 (2020); licensed under a Creative Commons Attribution (CC BY) license.[463] (f) Slow-light W1 PHC waveguide. Top panel shows that the back reflection in the finite structure alters the group velocity, which should vanish in the infinite structure. The perfectly matched tapers can suppress the back reflection and improve the slow light mode. Bottom panel shows the optimized W1 PHC waveguide with tapers. Reproduced from Faggiani *et al.*, Optica **4**, 393 (2017); licensed under a Creative Commons Attribution (CC BY) license.[464] (g) Purcell effect of the QD coupled with the slow-light waveguide mode. Top panels is the schematic of the sample. Bottom panel shows the time-resolved spectra for the QD in bulk material (green), the QD in the waveguide (black) and the system response function (blue). A Purcell factor of 20 is observed. Reproduced from Siampour *et al.*, npj Quantum Inf. **9**, 15 (2023); licensed under a Creative Commons Attribution (CC BY) license.[465]

conventional fiber. The β_{wg}-factor represents one of the critical parameters for characterizing waveguide properties. It is defined as the ratio of QD spontaneous emission power coupled into a specific waveguide mode Γ_{wg} to the total spontaneous emission power Γ_{tot}, yielding $\beta_{wg} = \Gamma_{wg}/\Gamma_{tot}$, thereby quantifying the coupling efficiency between the QD and the waveguide mode. A β_{wg}-factor equal to unity indicates that all spontaneous emission is channeled into the selected waveguide mode.[467,468]

Recently, chiral waveguides are attracting growing interest for their spin-momentum locking photon transport,[28,469,470] i.e., they provide unidirectional photon emission from circularly polarized single photons from the QD with resultant in-plane transfer of matter-qubit information.[471–473] The chirality of the waveguide stems from the strong structural confinement of the light field that results in transverse photon spin. In 2016, Coles *et al.*[460] demonstrated the local chiral behavior in a simple nanobeam waveguide. As shown in Fig. 18(b), the different positions in the waveguide have different chirality. When the QD is at the center of the waveguide, no chirality is observed in the emission directions. In contrast, when the QD is at the top edge of the waveguide, the left/right propagating modes have different local polarizations that couple to the QD. The left circular polarization emission from the QD will propagate left, while the right circular polarization emission from the QD will propagate right, showing the chiral waveguide-QD coupling behavior.[474] In 2021, Xiao *et al.*[461] extended the system from the single waveguide to the coupled waveguides with four output channels and achieved the deterministic chiral routing of photons. As shown in Fig. 18(c), depending on the different QD positions relative to each waveguide center, the routing of circularly polarized photons from the QDs can be adjusted. The chiral behaviors with quantum emitters typically require a perfect circular dipole located at certain positions of the waveguide exhibiting high local chirality. In 2022, Lang *et al.*[462] studied the circular polarization-based unidirectional emission to the elliptical polarization base. As shown in Fig. 18(d), the elliptical dipoles increase the size of the area suitable for chiral interactions and simultaneously increase the coupling efficiencies.

Topological waveguides, a recent hot topic, enable high transmission across sharp bends, which are critical building blocks for the low-loss photonic circuits. Waveguides exploiting the topological valley Hall effect and spin Hall effect[475] are both studied with QD embedded devices.[463,476–479] Fig. 18(e) presents a topological valley waveguide of bearded interface where the chiral interaction with single QDs was observed.[463] The local high chirality area can be indicated by the normalized Stokes parameter S_3, and $S_3 = \pm 1$ denotes the perfect circular polarization of the local waveguide photonic modes.

The support of slow light mode is a special feature of PHC waveguide, which leads to a dense LDOS and permits strong light–matter interaction for a broader spectral region.[480,481] This is generally because for the periodic structure, the group velocity vanishes near the band edges along with the diverging density of states. In 2017, Faggiani *et al.*[464] optimized the slow light mode in the PHC waveguide with inserted taper structures. As shown in Fig. 18(f), the major challenge of slow light mode in the experiment is that finite periodic structure introduces back reflections and alters the energy level structure. Thus, the group velocity does not entirely vanish. They developed the perfectly matched boundaries (tapers) to suppress the back reflection and improved the group index from 4 to 1000 (group velocity is 10^{-3} of light speed in vacuum). In 2023, Siampour *et al.*[465] coupled the slow light mode to the QD and demonstrated the Purcell effect. As shown in Fig. 18(g), the structure is a modified W1 PHC cavity, which is also called a glide-plane PHC waveguide. The group index of 100 results in an observed large Purcell factor of 20. With further design and optimization of the structure, we could expect a waveguide-QD coupling system with a high β_{wg}-factor, a high Purcell factor, and chiral routing with low propagation loss, therefore enabling a high efficiency on-chip quantum light source. In addition, the single-photon nonlinearity has also been explored based on the QD-waveguide platform.[482–484]

B. Integration technologies

Monolithic integration: GaAs/AlGaAs quantum photonic circuits provide a natural platform for full on-chip integration of III–V QDs.[491] The superior material compatibility of monolithic integration offers high lattice matching and excellent interface quality, enabling the fabrication and integration of key photonic devices, including quantum light sources, waveguides, beam splitters, and phase modulators on a single chip. The coupling between the cavity and waveguide is a basic on-chip unit. Figure 19(a) shows an example of the integration of an SPS and a waveguide.[485] It is achieved by a monolithic ring cavity with a DBR ridge waveguide. The coupling between waveguides provides the basis of a beam splitter and a logic gate. Li *et al.*[486] and Schnauber *et al.*[406] applied the multimode interference (MMI) coupler for the beam splitter, as shown by the schematic and the SEM image in Fig. 19(b). MMI relies on the self-imaging effect, whereby single-mode outputs can be achieved by simply positioning them at the self-imaging locations.[492] This approach offers several advantages: it requires low fabrication precision, exhibits broadband characteristics, demonstrates polarization and wavelength insensitivity, and enables various splitting ratios and quantities.[493] However, it suffers from disadvantages such as large footprint requirements, output imbalance, and excess loss.[494] In contrast, evanescent couplers (directional couplers) utilize evanescent wave coupling, such as the device made by Dusanowski *et al.*[487] shown in Fig. 19(c). The evanescent couplers offer advantages that include a compact footprint facilitating high-density integration with simple structures, flexibility in the splitting ratio, and low back-scattering losses.[495] Their splitting ratio is significantly influenced by the air gap size and length of the coupler,[496] necessitating high fabrication precision. They also show a narrow bandwidth characteristic and are sensitive to polarization. Additionally, evanescent couplers may introduce losses because of four bending sections.[497]

By combining the integration of different cavities and waveguides shown in Figs. 19(a)–19(c), we can realize fully on-chip integrated quantum photonic circuits, as shown in Fig. 19(d). Such circuits encompass quantum light sources, operators, and detectors.[490] The major challenge in the on-chip quantum photonic circuit is the random nature of QD growth. The randomness in spatial distribution and optical spectra of self-assembled QDs leads to non-deterministic coupling. With the development of QD positioning technologies, *in situ* lithography is employed to achieve deterministic integration of one or two QDs, such as the devices in Figs. 19(a)–19(c). In the future, the QD site-controlled growth and deterministic manufacturing techniques mentioned above constitute the principal solutions to this challenge.

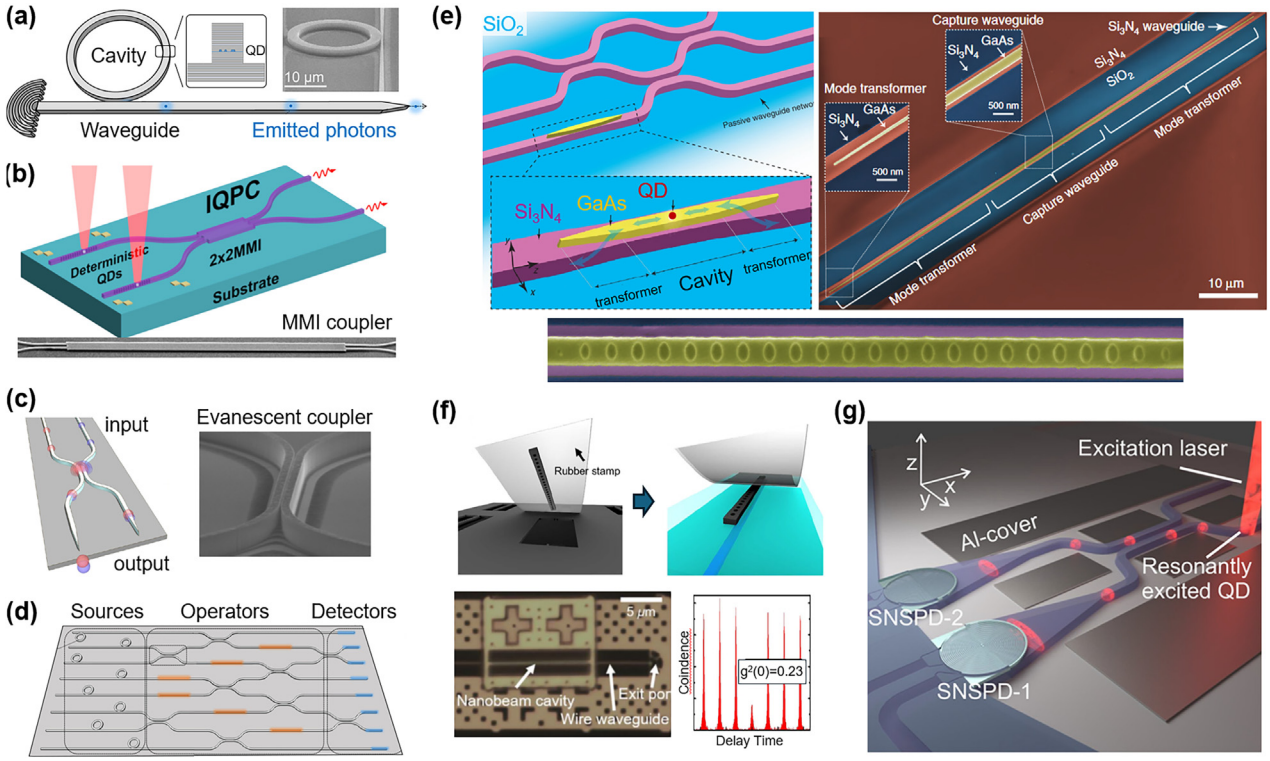

FIG. 19. On-chip integration technologies for QDs. (a) Integration of cavity–QD SPS with the waveguide. Reproduced with permission from Nano Lett. **20**, 6357–6363 (2020). Copyright 2020, American Chemical Society.[485] (b) Integration of two QDs in waveguides with MMI beam splitter (coupler). Upper panel shows the schematic of the device. Bottom panel shows the SEM image of the MMI coupler. Reproduced with permission from ACS Photonics **10**, 2846–2853 (2023). Copyright 2023, American Chemical Society.[486] (c) Integration of two QDs in waveguides with evanescent coupler. (d) Schematic of all-GaAs on-chip photonic circuit integrating SPSs, beam splitters, phase shifters, and detectors. Reproduced with permission from ACS Photonics **10**, 2941–2947 (2023). Copyright 2023, American Chemical Society.[487] (e) Heterogeneous integration of GaAs and Si_3N_4 waveguides. Top panel shows the schematic and false-color SEM image of device. Bottom panel shows false-color SEM image of the waveguide. Reproduced from Davanc *et al.*, Nat. Commun. **8**, 889 (2017); licensed under a Creative Commons Attribution (CC BY) license.[488] (f) Transfer printing process for heterogeneous integration. Top panels show the pick-up and place-down processes of the nanobeam cavity with embedded QD. Bottom left panel shows the image of integrated device. Bottom right panel shows that the SPS after heterogeneous integration still exhibits antibunching. Reproduced from Katsumi *et al.*, Optica **5**, 691 (2018); licensed under a Creative Commons Attribution (CC BY) license.[489] (g) Integration of QDs with superconducting nanowire single-photon detectors (SNSPD). Reproduced with permission from Nano Lett. **20**, 6357–6363 (2020). Copyright 2020, American Chemical Society.[490]

Heterogeneous integration: Heterogeneous integration techniques are necessary because the optimal materials to fabricate different devices are mostly different. For example, silicon photonics platforms provide a critical pathway for large-scale quantum photonic integrated circuits through their compatibility with complementary metal-oxide semiconductor (CMOS) fabrication processes and inherent cost advantages.[498] Heterogeneous integration combines III–V QD light sources with silicon-based photonic devices, creating an architecture where III–V chips generate high-quality quantum light while the silicon platform handles optical routing, processing, and detection functions. Silicon waveguides possess high refractive index contrast, enabling compact photonic device designs and low-loss optical transmission. Si_3N_4 represents one of the most prevalent silicon-based materials, offering broadband optical transparency, tunable dispersion properties, ultra-low propagation losses and relatively high Kerr nonlinearities.[488,499,500] The primary challenge in hybrid integration lies in addressing refractive index mismatch and mode matching issues between dissimilar materials. This is typically accomplished through tapered couplers,[488,500–503] grating couplers[504] or evanescent couplers[503,505] to enhance coupling efficiency. Such platforms are particularly well-suited for constructing large-scale quantum computing and quantum communication systems, capable of integrating hundreds to thousands of photonic devices on a single chip.

Current heterogeneous integration techniques for QDs include heterogeneous epitaxial growth, wafer bonding, pick-and-place, and adhesive bonding. Heterogeneous epitaxial growth involves the direct growth of III–V QDs on silicon substrates.[64,505–507] This approach offers relatively simple processing, enables monolithic integration, provides excellent electrical and thermal contact, and is suitable for large-scale production. However, due to lattice mismatch, extensive buffer layers are typically required, which not only compromises crystal quality but also results in QDs being positioned too far from the boundary, thereby affecting coupling efficiency with the circuit. Furthermore, differences in thermal expansion coefficients introduce stress that can cause unintended effects.

Wafer bonding technology bonds a III–V QD device wafer to a silicon-based wafer through surface activation, cleaning and high-temperature treatment, and then etches the structure on the III–V device after the bonding.[488,500,508,509] This method can employ either direct bonding or indirect bonding through intermediate layers (such as silicon oxide). This technology can maintain the high quality of III–V materials and avoid lattice mismatch issues associated with heterogeneous epitaxial growth, reducing losses due to the distance of QDs to the circuit surface. Current bonding process is relatively mature and allows for large area bonding. The uncertainty in structural positioning can be improved through site-controlled growth and lithography techniques. Figure 19(e) demonstrates the integrated circuit following wafer bonding, where GaAs devices are integrated onto Si_3N_4 waveguides.[488] The disadvantages of wafer bonding include the requirement for high-precision surface treatment, sensitivity of bonding strength to environmental conditions, relatively high process complexity, and potential interface defects that may affect device performance. Additionally, since the bonding step occurs after CMOS fabrication, the high temperatures required by the process may cause some damage to CMOS components. In 2025, Wang *et al.*[510] integrated QD waveguide arrays with low-loss lithium niobate (LN) photonic circuits through wafer bonding technology, incorporating 20 deterministic SPS to achieve a nearly complete on-chip circuit. By leveraging the piezoelectric properties of thin-film LN, a circuit-compatible strain tuning technique was introduced, enabling on-chip localized spectral tuning of individual QD emission.

Pick-and-place techniques enable the relocation of pre-fabricated III–V QD devices from their native growth substrates to target silicon-based substrates. This method offers the advantage of preserving the original high quality of devices. Compared to wafer bonding technology, it facilitates the transfer of more complex structures and enables selective integration. Transfer printing is a subset of pick-and-place techniques, where rubber stamps, such as polydimethylsiloxane (PDMS), are used to facilitate the transfer process.[489,511–515] Figure 19(f) illustrates the process of transferring suspended nanobeams using the rubber stamp and shows a visible microscope image.[489] The measurement of the second-order coherence function indicates good purity of single photons generated with the integration system. However, the transfer accuracy of rubber stamp methods is inherently limited, with challenges in controlling both relative positioning and orientation. Due to these constraints, this approach is more suitable for small-scale devices and may introduce interface contamination during the transfer process. For example, Larocque *et al.*[516] used a rubber stamp for heterogeneous integration of multiple InAs/InP microchips containing high-brightness infrared semiconductor QD SPS into advanced silicon-on-insulator photonic integrated circuits, demonstrating scalable emission wavelength programmability with single emitter resolution. In a broader context, pick-and-place techniques also encompass the direct transfer of pre-fabricated III–V structures to silicon-based substrates.[502,517–519] This method uses precise manipulation of probe tips to relocate structures, achieving accuracy typically at the sub-micrometer level. For instance, in 2022, Chanana *et al.*[519] employed pick-and-place techniques to achieve heterogeneous integration of III–V SPS onto Si_3N_4 waveguides, leading to a significant reduction in coupling loss.

Adhesive bonding is relatively simple and precise in operation, directly using adhesives to integrate two components together. There are multiple types of adhesives available. The first type employs polymers such as benzocyclobutene (BCB), where the two devices are aligned and then subjected to heating and pressure, causing the liquid adhesive to transform into a rigid solid phase for integration.[520,521] The second type utilizes optical adhesives that are cured through ultraviolet light exposure.[504] Adhesive bonding has relatively low equipment requirements, making it suitable for rapid prototyping, and imposes less stringent requirements on substrate surface quality. However, the bonding strength is limited, and it may introduce additional thermal and electrical resistance. The thermal stability of optical adhesives also needs to be considered.

Hybrid quantum systems: Heterogeneous integration technology enables the fabrication of a single device by combining different materials. Unlike the direct fabrication of a single device from more than one material, we can also integrate multiple devices made of distinct materials into a system to form a hybrid system. As discussed above, a complete quantum optical circuit typically comprises quantum emitters, waveguides, single-photon detectors, and other processing components. Leveraging the strengths of different material platforms enables the realization of efficient hybrid quantum systems, such as the hybrid integration of III–V QDs with superconducting nanowire single-photon detectors (SNSPDs). Various approaches have been developed to integrate components from different material platforms into a single-photonic system, among which photonic wire bonding (PWB) is a representative example. Photonic wire bonding represents an emerging three-dimensional integration technology that interconnects optical devices across different chips via polymer waveguides fabricated through direct-write two-photon lithography.[499,522–524] The flexible nature of these waveguides confers high integration flexibility and forms three-dimensional connections. PWB imposes minimal requirements on substrate materials and eliminates the need for elevated temperatures, rendering it well-suited for hybrid systems. Nevertheless, this integration approach is characterized by relatively elevated optical losses, necessitating stringent process precision, and is presently limited primarily to optical interconnections rather than electrical integration applications.

The integration of single-photon detectors into circuits constitutes the final step of on-chip integration. Superconducting nanowire single-photon detectors are particularly compelling owing to their high detection efficiency, sub-50 ps timing jitter, and nanosecond reset times. Najafi *et al.*[525] employed pick-and-place methodology to integrate multiple SNSPDs into on-chip circuits, marking the first demonstration of on-chip photon correlation measurements of non-classical light. The system detection efficiency for four simultaneously operating SNSPDs was projected to achieve 14%–52%, substantially surpassing the $< 1\%$ efficiency reported in prior investigations.[526,527] An alternative approach involves the direct growth of SNSPDs on GaAs interfaces via direct current magnetron sputtering.[528] Reithmaier *et al.*[529] utilized this methodology to integrate SNSPDs with QDs, achieving detection through evanescent coupling mechanisms. The incorporation of an AlN buffer layer mitigates lattice mismatch, thereby yielding enhanced critical temperature, critical current density, and reduced residual resistivity.[530] Furthermore, the implementation of a double-helix Archimedean spiral geometry serves to reduce critical current requirements.[531] These technologies result in diminished dark count rates, enhanced detection efficiency, and reduced timing jitter. Schwartz *et al.*[490] leveraged these methodologies to integrate SNSPDs

with QDs, successfully realizing on-chip HBT experiments, with the experimental apparatus illustrated in Fig. 19(g). These achievements demonstrate the critical progression of SNSPD technology from initial on-chip integration, through on-chip integration with QDs, to the achievement of complete on-chip HBT measurements.

VII. SUMMARY AND OUTLOOK

In summary, III–V QDs have been investigated and optimized for quantum technologies over the past few decades. The excitons and their coupling to the nanophotonic systems have been enhanced and utilized to achieve the quantum light sources and spin–photon interfaces. Preliminary theoretical and experimental investigations have been carried out on QD applications in quantum communication and quantum computing, encompassing long-distance qubit transmission,[532] quantum random number generation,[533,534] quantum repeaters,[535] quantum key distribution,[536–540] and boson sampling.[541] It is worth noting that quantum key distribution has successfully demonstrated high-rate intercity transmission over distances reaching 79 km[538] and the longest distance through telecom fiber reached 175 km,[537] thereby establishing the significant potential of QDs in quantum communication technologies. Meanwhile, we would expect more optimizations and breakthroughs in applications based on QDs in the future. Figure 20 illustrates the outlook on future developments in QD research. The inner areas represent the four general directions of current research in QDs, starting from the most basic QD growth, through the realization of quantum light sources and spin/exciton–photon interfaces, to integrated optics based on application needs. The outer part delineates potential future research directions, with color saturation serving as an indicator of implementation complexity.

III–V QDs are most commonly grown by MBE using the SK method and DE method. To date, QDs at the visible and NIR wavelength range have been optimized with the best single-photon emission performance compared to other kinds of quantum sources. There are three main challenges in the future applications in large-scale quantum devices. First, the emission wavelength of QDs in the wafer needs to be identical, i.e., the homogeneity of QDs needs to be improved. Second, the QDs need to be deterministically grown at designed positions, i.e., site-controlled growth. Third, the photon wavelength needs to shift to the telecom bands while preserving high optical emission quality to suppress the photon loss in the network. Much effort has been reported to improve these three properties. However, simultaneously achieving these three goals while maintaining the high quality of QDs, including negligible FSS, high brightness, and suppressed non-radiative decay rate, has not been realized yet. For GaN QDs, which are currently the candidates for room-temperature applications, the main challenge is that increasing temperature enhances exciton–phonon interactions, thereby reducing brightness, broadening the emission linewidth, and accelerating decoherence. Furthermore, GaN quantum dots are difficult to implement in the telecom wavelength range. This requires further exploration in both the material and the method.

The quantum light source is one of the major applications of III–V QDs. The weakly coupled cavity–QD system is the center of the quantum light source, in which the Purcell effect from the cavity

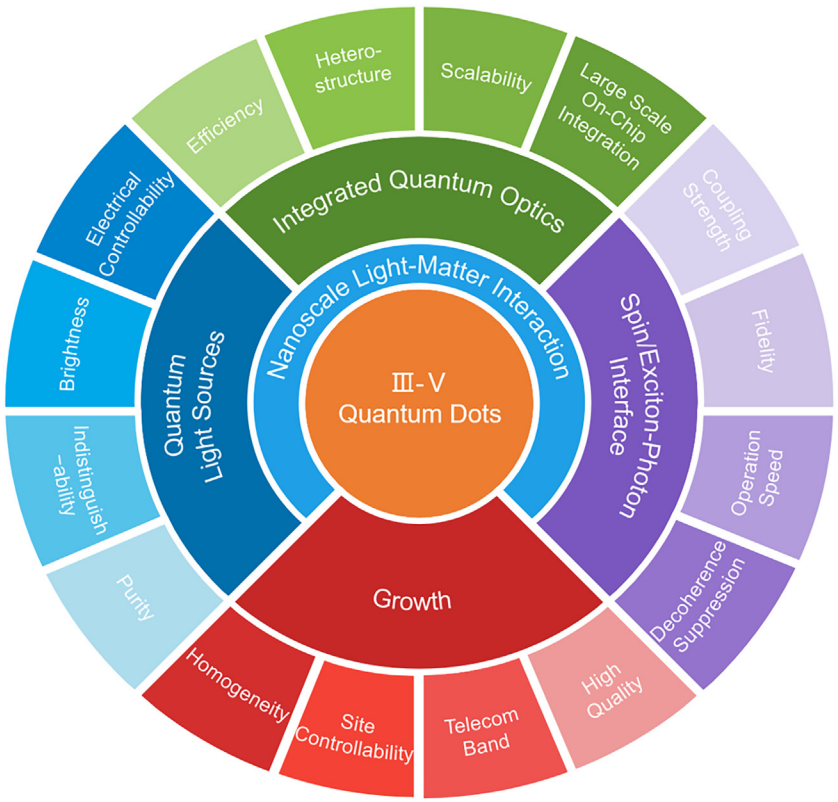

FIG. 20. Summary and outlook of III–V QDs in quantum technologies, mainly including the QD growth methods, the quantum light sources, the spin/exciton–photon interfaces, and the integrated quantum photonics.

improves the purity, indistinguishability, and brightness of the single photons emitted from the QD. The manipulation of the exciton properties is fundamental to improving the performance of the cavity–QD system. The external electric and magnetic fields are applied to manipulate the emission energy and the polarization to match those of the cavity mode. The strain is applied to improve the symmetry of the QD and suppress the FSS, which is the key to the fidelity of entangled photons. Compared to the static strain, the periodic strain (acoustic wave) introduces dynamic and high-frequency manipulation of the QD emission. This enables scalable on-chip quantum communication protocols. Combining manipulations in multiple degrees of freedom is a potential method to further improve the performance of the quantum light source in the future. Most quantum light sources are based on the optical excitation of the QD, which raises challenges in the miniaturization and integration on-chip. In contrast, in recent years, little progress has been reported in the electrical excitation of the quantum light source.[177,178] However, electrical excitation is necessary for on-chip integration and the real "plug-and-play" devices.[542–545] This is a major challenge for the development of the quantum light source in the future.

The strongly coupled cavity–QD system provides the spin/exciton–photon interface with the on-chip integrability. The coupling strength is the most important parameter, which directly determines the fidelity and operation speed of the quantum interface. For the conventional s-shell exciton in the III–V QD with the size ∼20 nm, the coupling strength to a typical L3 PHC cavity is ∼50 μeV, which is enough to achieve the Rabi splitting in the strong coupling regime. When the coupling strength increases to ∼100 μeV, the two-photon Rabi splitting occurs between the biexciton state and two photons, promoting the quantum interface to the two-photon nonlinear regime. Moreover, when we introduce the p-shell exciton to couple to the cavity, the exciton–photon coupling enters the nonlocal regime, and the coupling strength is tuned to 210 μeV at maximum through the magneto wavefunction control. In addition to the increase in the coupling strength, the suppression of the decoherence process is also crucial to improve the fidelity. Particularly, the nanophotonic cavity structures near the QD will introduce additional surface states, which increase the dephasing rate and emission linewidth of the exciton. Such decoherence effects are far from fully explored, and further investigations would be an important topic in the future study.

The QD embedded in solid-state nanophotonic cavities is the basic building block in the on-chip integrated quantum photonic devices. In this scheme, the coupling efficiency between the QD and the cavity, as well as the coupling efficiency between the cavity–QD system and the waveguide, plays key roles in improving the performance. Waveguides supporting the chirality, topology, and slow light mode have been developed to achieve novel functionalities such as the unidirectional router, robust propagation, and the Purcell effect for the embedded QD. The coupling efficiency in the monolithic integration, i.e., the QD, the cavity, and the waveguides are all III–V materials, has been optimized to above 50 %. However, waveguides based on III–V materials introduce the relatively large photon loss rate, and therefore, the heterogeneous integration of III–V QD devices into high-performance silicon-based platforms and SNSPD systems is necessary to achieve the low-loss on-chip devices. Integration effectiveness is primarily constrained by efficiency limitations, requiring improvement of heterogeneous integration technologies to minimize inter-material signal losses. In addition, the scalability is another challenge for the devices based on QDs. Till now, there are only small-scale attempts at on-chip integration including two QDs, and achieving on-chip coherent integration of more than three QDs simultaneously remains a challenge. On one hand, we need to improve the QD growth method as discussed above, toward the generating of identical QDs at selective positions. On the other hand, the on-chip integration technology still needs to be optimized toward the high efficiency, high controllability, and low additional dephasing. Leveraging mature heterogeneous integration techniques for the co-design of QDs, waveguides, and SNSPDs is essential to enhance efficiency and scalability, aiming to build large-scale on-chip hybrid quantum systems capable of handling complex computations. Notably, successful demonstration of HBT experiments on-chip with QDs and SNSPDs has already been demonstrated.[490] Future development in all these technologies is expected to achieve the quantum photonic network with large-scale on-chip integration.

Furthermore, the excitonic/electronic transitions are the fundamental emission processes in various kinds of semiconductors. Therefore, the excitonic manipulation, the spin–photon interface, and the cQED discussed in this review would also help the study and application of other semiconductor emitters. For example, the magneto spectroscopy has been applied to control the exciton energy and probe the excitonic properties such as colloidal QDs, color centers, and 2D materials.[546] The manipulation through strain and acoustic waves has shown better effects in 2D materials, since the atomically thin structure is more sensitive to the deformations.[547–550] The Purcell effect has been applied to enhance the optoelectronic coupling for various purpose such as improving the luminescence efficiency of perovskites.[551] The nonlocal exciton–photon coupling beyond the dipole approximation has been applied to control the exciton–photon coupling between the cavity and the free exciton in the 2D materials.[552] Therefore, the development of QD-based nanophotonics and quantum photonic technologies will also bring insights to the investigation of other optoelectronic materials and different quantum photonic systems.

ACKNOWLEDGMENTS

This work was supported by the National Natural Science Foundation of China (Grant Nos. 62025507, 12494600, 12494601, 12494603, 92250301, 22461142143, and 12404033) and the National Key Research and Development Program of China (Grant No. 2021YFA1400700).

AUTHOR DECLARATIONS

Conflict of Interest

The authors have no conflicts to disclose.

Author Contributions

Zhikai Ma and Shiyao Wu contributed equally to this work.

Zhikai Ma: Resources (lead); Writing – original draft (lead); Writing – review & editing (lead). **Shiyao Wu:** Resources (lead); Writing – original draft (lead); Writing – review & editing (lead). **Hancong Li:** Resources (equal); Writing – original draft (equal); Writing – review & editing (equal). **Xiqing Chen:** Resources (equal); Writing – original draft (equal); Writing – review & editing (equal). **Kai Peng:** Conceptualization (equal); Resources (equal); Writing – original draft

(equal); Writing – review & editing (equal). **Chenjiang Qian:** Conceptualization (equal); Resources (equal); Writing – original draft (equal); Writing – review & editing (equal). **Kuijuan Jin:** Conceptualization (equal); Writing – review & editing (equal). **Qihuang Gong:** Conceptualization (equal); Writing – review & editing (equal). **Xiulai Xu:** Conceptualization (lead); Funding acquisition (lead); Writing – original draft (equal); Writing – review & editing (equal).

DATA AVAILABILITY

The data that support the findings of this study are available from the corresponding author upon reasonable request.

REFERENCES

[1]P. Lodahl, S. Mahmoodian, and S. Stobbe, Rev. Mod. Phys. **87**, 347 (2015).
[2]K. Vahala, Y. Arakawa, and A. Yariv, Appl. Phys. Lett. **50**, 365 (1987).
[3]W. Zhang, X. Xie, H. Hao, J. Dang, S. Xiao, S. Shi, H. Ni, Z. Niu, C. Wang, K. Jin, X. Zhang, and X. Xu, Light Sci. Appl. **9**, 109 (2020).
[4]M. C. Weidman, M. E. Beck, R. S. Hoffman, F. Prins, and W. A. Tisdale, ACS Nano **8**, 6363 (2014).
[5]X. Jin, K. Xie, T. Zhang, H. Lian, Z. Zhang, B. Xu, D. Li, and Q. Li, Chem. Commun. **56**, 6130 (2020).
[6]I. L. Medintz, H. T. Uyeda, E. R. Goldman, and H. Mattoussi, Nat. Mater. **4**, 435 (2005).
[7]X. Gong, Z. Yang, G. Walters, R. Comin, Z. Ning, E. Beauregard, V. Adinolfi, O. Voznyy, and E. H. Sargent, Nat. Photonics **10**, 253 (2016).
[8]T. Heindel, J.-H. Kim, N. Gregersen, A. Rastelli, and S. Reitzenstein, Adv. Opt. Photonics **15**, 613 (2023).
[9]D. A. Vajner, L. Rickert, T. Gao, K. Kaymazlar, and T. Heindel, Adv. Quantum Technol. **5**, 2100116 (2022).
[10]F. P. G. de Arquer, D. V. Talapin, V. I. Klimov, Y. Arakawa, M. Bayer, and E. H. Sargent, Science **373**, eaaz8541 (2021).
[11]Y. Arakawa and H. Sakaki, Appl. Phys. Lett. **40**, 939 (1982).
[12]G. Bastard, Phys. Rev. B **24**, 4714 (1981).
[13]C. Weisbuch, R. Dingle, A. C. Gossard, W. Wiegmann, B. Laboratories, M. Hill, and E. Burstein, Solid State Commun. **38**, 709 (1981).
[14]D. J. Eaglesham and M. Cerullo, Phys. Rev. Lett. **64**, 1943 (1990).
[15]S. Guha, A. Madhukar, and K. C. Rajkumar, Appl. Phys. Lett. **57**, 2110 (1990).
[16]C. B. Murray, C. R. Kagan, and M. G. Bawendi, Science **270**, 1335 (1995).
[17]L. Chu, M. Arzberger, G. Böhm, and G. Abstreiter, J. Appl. Phys. **85**, 2355 (1999).
[18]L. E. Brus, J. Chem. Phys. **79**, 5566 (1983).
[19]M. Liu, N. Yazdani, M. Yarema, M. Jansen, V. Wood, and E. H. Sargent, Nat. Electron. **4**, 548 (2021).
[20]M. Atatüre, D. Englund, N. Vamivakas, S.-Y. Lee, and J. Wrachtrup, Nat. Rev. Mater. **3**, 38 (2018).
[21]I. Aharonovich, D. Englund, and M. Toth, Nat. Photonics **10**, 631 (2016).
[22]K. J. Vahala, Nature **424**, 839 (2003).
[23]L. C. Andreani, G. Panzarini, and J.-M. Gérard, Phys. Rev. B **60**, 13276 (1999).
[24]J. Liu, R. Su, Y. Wei, B. Yao, S. F. C. d Silva, Y. Yu, J. Iles-Smith, K. Srinivasan, A. Rastelli, J. Li, and X. Wang, Nat. Nanotechnol. **14**, 586 (2019).
[25]N. Somaschi, V. Giesz, L. De Santis, J. C. Loredo, M. P. Almeida, G. Hornecker, S. L. Portalupi, T. Grange, C. Antón, J. Demory, C. Gómez, I. Sagnes, N. D. Lanzillotti-Kimura, A. Lemaítre, A. Auffeves, A. G. White, and P. C. Lanco, Nat. Photonics **10**, 340 (2016).
[26]F. Liu, A. J. Brash, J. O'Hara, L. M. P. P. Martins, C. L. Phillips, R. J. Coles, B. Royall, E. Clarke, C. Bentham, N. Prtljaga, I. E. Itskevich, L. R. Wilson, M. S. Skolnick, and A. M. Fox, Nat. Nanotechnol. **13**, 835 (2018).
[27]Y. Yu, S. Liu, C.-M. Lee, P. Michler, S. Reitzenstein, K. Srinivasan, E. Waks, and J. Liu, Nat. Nanotechnol. **18**, 1389 (2023).
[28]P. Lodahl, S. Mahmoodian, S. Stobbe, A. Rauschenbeutel, P. Schneeweiss, J. Volz, H. Pichler, and P. Zoller, Nature **541**, 473 (2017).
[29]X. Wang, J. Zhuang, Q. Peng, and Y. Li, Nature **437**, 121 (2005).
[30]R. Rossetti, S. Nakahara, and L. E. Brus, J. Chem. Phys. **79**, 1086 (1983).
[31]M. Bayer, Ann. Phys. **531**, 1900039 (2019).
[32]G. Rainó, M. A. Becker, M. I. Bodnarchuk, R. F. Mahrt, M. V. Kovalenko, and T. St'oferle, Nature **563**, 671 (2018).
[33]P. M. Petroff, A. C. Gossard, R. A. Logan, and W. Wiegmann, Appl. Phys. Lett. **41**, 635 (1982).
[34]F. Houzay, C. Guille, J. Moison, P. Henoc, and F. Barthe, J. Cryst. Growth **81**, 67 (1987).
[35]A. Cho and J. Arthur, Prog. Solid State Ch. **10**, 157 (1975).
[36]U. W. Pohl, "Thermodynamics of epitaxial layer-growth," in *Epitaxy of Semiconductors: Physics and Fabrication of Heterostructures* (Springer International Publishing, Cham, 2020), pp. 207–250.
[37]I. Bozovic, IEEE T. Appl. Supercon. **11**, 2686 (2001).
[38]K. Nishi, T. Kageyama, M. Yamaguchi, Y. Maeda, K. Takemasa, T. Yamamoto, M. Sugawara, and Y. Arakawa, J. Cryst. Growth **378**, 459 (2013).
[39]H. Liu, T. Wang, Q. Jiang, R. Hogg, F. Tutu, F. Pozzi, and A. Seeds, Nat. Photonics **5**, 416 (2011).
[40]R. J. Warburton, Nat. Mater. **12**, 483–493 (2013).
[41]A. J. Shields, Nat. Photonics **1**, 215 (2007).
[42]G. Stringfellow, "Fundamental aspects of MOVPE," in *Metalorganic Vapor Phase Epitaxy (MOVPE)* (John Wiley I& Sons, Ltd., 2019), Chap. 2, pp. 19–69.
[43]F. C. Frank, J. H. van der Merwe, and N. F. Mott, Proc. R. Soc. London A **198**, 205 (1949).
[44]V. G. Dubrovskii, *Nucleation Theory and Growth of Nanostructures* (Springer, 2014).
[45]K. A. Lozovoy, A. G. Korotaev, A. P. Kokhanenko, V. V. Dirko, and A. V. Voitsekhovskii, Surf. Coat. Technol. **384**, 125289 (2020).
[46]K. D. Vallejo, C. I. Cabrera-Perdomo, T. A. Garrett, M. D. Drake, B. Liang, K. A. Grossklaus, and P. J. Simmonds, ACS Nano **17**, 2318 (2023).
[47]J. Prieto and I. Markov, Surf. Sci. **664**, 172 (2017).
[48]D. Leonard, M. Krishnamurthy, C. M. Reaves, S. P. Denbaars, and P. M. Petroff, Appl. Phys. Lett. **63**, 3203 (1993).
[49]A. D. Yoffe, Adv. Phys. **50**, 1–208 (2001).
[50]N. Koguchi, S. Takahashi, and T. Chikyow, J. Cryst. Growth **111**, 688 (1991).
[51]N. Koguchi and K. Ishige, Jpn. J. Appl. Phys. **32**, 2052 (1993).
[52]K. I. N. Koguchi and S. Takahashi, J. Vac. Sci. Technol. B **11**, 787 (1993).
[53]A. Nemcsics, in *Quantum Dots*, edited by V. N. Stavrou (IntechOpen, Rijeka, 2015), Chap. 5.
[54]R. S. R. Gajjela, N. R. S. van Venrooij, A. R. da Cruz, J. Skiba-Szymanska, R. M. Stevenson, A. J. Shields, C. E. Pryor, and P. M. Koenraad, Nanotechnology **33**, 305705 (2022).
[55]R. S. R. Gajjela and P. M. Koenraad, Nanomaterials **11**, 85 (2021).
[56]S. Tamariz, G. Callsen, J. Stachurski, K. Shojiki, R. Butté, and N. Grandjean, ACS Photonics **7**, 1515 (2020).
[57]M. Arita, F. Le Roux, M. J. Holmes, S. Kako, and Y. Arakawa, Nano Lett. **17**, 2902 (2017).
[58]M. J. Holmes, T. Zhu, F. C.-P. Massabuau, J. Jarman, R. A. Oliver, and Y. Arakawa, APL Mater. **9**, 061106 (2021).
[59]S. Bietti, F. B. Basset, A. Tuktamyshev, E. Bonera, A. Fedorov, and S. Sanguinetti, Sci. Rep. **10**, 6532 (2020).
[60]F. Basso Basset, S. Bietti, M. Reindl, L. Esposito, A. Fedorov, D. Huber, A. Rastelli, E. Bonera, R. Trotta, and S. Sanguinetti, Nano Lett. **18**, 505 (2018).
[61]Y. H. Huo, V. Křápek, A. Rastelli, and O. G. Schmidt, Phys. Rev. B **90**, 041304 (2014).
[62]J. Skiba-Szymanska, R. M. Stevenson, C. Varnava, M. Felle, J. Huwer, T. Müller, A. J. Bennett, J. P. Lee, I. Farrer, A. B. Krysa, P. Spencer, L. E. Goff, D. A. Ritchie, J. Heffernan, and A. J. Shields, Phys. Rev. Appl. **8**, 014013 (2017).
[63]C. Shang, M. De Gregorio, Q. Buchinger, M. Meinecke, P. Gschwandtner, A. Pfenning, T. Huber-Loyola, S. Hoefling, and J. E. Bowers, APL Quantum **1**, 036115 (2024).
[64]I. Limame, P. Ludewig, C.-W. Shih, M. Hohn, C. C. Palekar, W. Stolz, and S. Reitzenstein, Optica Quantum **2**, 117 (2024).
[65]L. Seravalli, C. Bocchi, G. Trevisi, and P. Frigeri, J. Appl. Phys. **108**, 114313 (2010).
[66]M. Paul, J. Kettler, K. Zeuner, C. Clausen, M. Jetter, and P. Michler, Appl. Phys. Lett. **106**, 122105 (2015).

[67]A. Tuktamyshev, A. Fedorov, S. Bietti, S. Vichi, K. D. Zeuner, K. D. Jöns, D. Chrastina, S. Tsukamoto, V. Zwiller, M. Gurioli, and S. Sanguinetti, Appl. Phys. Lett. **118**, 133102 (2021).
[68]R. Sittig, C. Nawrath, S. Kolatschek, S. Bauer, R. Schaber, J. Huang, P. Vijayan, P. Pruy, S. L. Portalupi, M. Jetter, and P. Michler, Nanophotonics **11**, 1109 (2022).
[69]P. A. Wroński, P. Wyborski, A. Musiał, P. Podemski, G. Sek, S. H"ofling, and F. Jabeen, Materials **14**, 5221 (2021).
[70]W. Zhan, S. Ishida, J. Kwoen, K. Watanabe, S. Iwamoto, and Y. Arakawa, Phys. Status Solidi B **257**, 1900392 (2020).
[71]J. Riikonen, J. Sormunen, H. Koskenvaara, M. Mattila, M. Sopanen, and H. Lipsanen, Jpn. J. Appl. Phys. **44**, L976 (2005).
[72]K. Takemoto, Y. Sakuma, S. Hirose, T. Usuki, N. Yokoyama, T. Miyazawa, M. Takatsu, and Y. Arakawa, Jpn. J. Appl. Phys. **43**, L993 (2004).
[73]K. Takemoto, Y. Sakuma, S. Hirose, T. Usuki, and N. Yokoyama, Jpn. J. Appl. Phys. **43**, L349 (2004).
[74]P. Holewa, M. Gawełczyk, C. Ciostek, P. Wyborski, S. Kadkhodazadeh, E. Semenova, and M. Syperek, Phys. Rev. B **101**, 195304 (2020).
[75]J. Kwoen, M. Kakuda, and Y. Arakawa, Opt. Mater. Express **15**, 939 (2025).
[76]A. Kors, J. P. Reithmaier, and M. Benyoucef, Appl. Phys. Lett. **112**, 172102 (2018).
[77]C. L. Phillips, A. J. Brash, M. Godsland, N. J. Martin, A. Foster, A. Tomlinson, R. Dost, N. Babazadeh, E. M. Sala, L. Wilson, J. Heffernan, M. S. Skolnick, and A. M. Fox, Sci. Rep. **14**, 4450 (2024).
[78]D. A. Vajner, P. Holewa, E. Zięba-Ostój, M. Wasiluk, M. von Helversen, A. Sakanas, A. Huck, K. Yvind, N. Gregersen, A. Musiał, M. Syperek, E. Semenova, and T. Heindel, ACS Photonics **11**, 339 (2024).
[79]P. Wyborski, A. Musiał, P. Mrowiński, P. Podemski, V. Baumann, P. Wroński, F. Jabeen, S. Höfling, and G. Sęk, Materials **14**, 759 (2021).
[80]A. Chellu, J. Hilska, J.-P. Penttinen, and T. Hakkarainen, APL Mater. **9**, 051116 (2021).
[81]J. Michl, G. Peniakov, A. Pfenning, J. Hilska, A. Chellu, A. Bader, M. Guina, S. Höfling, T. Hakkarainen, and T. Huber-Loyola, Adv. Quantum Technol. **6**, 2300180 (2023).
[82]S. Manna, H. Huang, S. F. C. da Silva, C. Schimpf, M. B. Rota, B. Lehner, M. Reindl, R. Trotta, and A. Rastelli, Appl. Surf. Sci. **532**, 147360 (2020).
[83]J. Liu, K. Konthasinghe, M. Davanço, J. Lawall, V. Anant, V. Verma, R. Mirin, S. W. Nam, J. D. Song, B. Ma, Z. S. Chen, H. Q. Ni, Z. C. Niu, and K. Srinivasan, Phys. Rev. Appl. **9**, 064019 (2018).
[84]X. Cao, J. Yang, P. Li, Y. Zhang, E. P. Rugeramigabo, B. Brechtken, R. J. Haug, M. Zopf, and F. Ding, Appl. Phys. Lett. **118**, 221107 (2021).
[85]J. Zhao, R. Liu, G. Zou, Z. Ge, Q. Zhang, Y. Qiao, X. Ding, G. Jiang, Y. Lou, Y. Guo, T. Chung, Y. He, C. Lu, Y. Huo, and J. Pan, Light Sci. Appl. **14**, 170 (2025).
[86]K. Karrai, R. J. Warburton, C. Schulhauser, A. Högele, B. Urbaszek, E. J. McGhee, A. O. Govorov, J. M. Garcia, B. D. Gerardot, and P. M. Petroff, Nature **427**, 135 (2004).
[87]B. Urbaszek, E. J. McGhee, M. Krüger, R. J. Warburton, K. Karrai, T. Amand, B. D. Gerardot, P. M. Petroff, and J. M. Garcia, Phys. Rev. B **69**, 035304 (2004).
[88]Q. Q. Wang, A. Muller, P. Bianucci, E. Rossi, Q. K. Xue, T. Takagahara, C. Piermarocchi, A. H. MacDonald, and C. K. Shih, Phys. Rev. B **72**, 035306 (2005).
[89]J. M. Villas-Bôas, S. E. Ulloa, and A. O. Govorov, Phys. Rev. Lett. **94**, 057404 (2005).
[90]M. Kaniber, A. Laucht, A. Neumann, J. M. Villas-Bôas, M. Bichler, M.-C. Amann, and J. J. Finley, Phys. Rev. B **77**, 161303 (2008).
[91]X. Lu, S. Matsubara, Y. Nakagawa, T. Kitada, and T. Isu, J. Cryst. Growth **425**, 106 (2015).
[92]M. C. Löbl, S. Scholz, I. Söllner, J. Ritzmann, T. Denneulin, A. Kovács, B. E. Kardynał, A. D. Wieck, A. Ludwig, and R. J. Warburton, Commun. Phys. **2**, 93 (2019).
[93]M. Bayer, G. Ortner, O. Stern, A. Kuther, A. A. Gorbunov, A. Forchel, P. Hawrylak, S. Fafard, K. Hinzer, T. L. Reinecke, S. N. Walck, J. P. Reithmaier, F. Klopf, and F. Schäfer, Phys. Rev. B **65**, 195315 (2002).
[94]R. Seguin, A. Schliwa, S. Rodt, K. Pötschke, U. W. Pohl, and D. Bimberg, Phys. Rev. Lett. **95**, 257402 (2005).
[95]J. D. Mar, J. J. Baumberg, X. L. Xu, A. C. Irvine, and D. A. Williams, Physical Review B **93**, 045316 (2016)
[96]S. F. C. da Silva, G. Undeutsch, B. Lehner, S. Manna, T. M. Krieger, M. Reindl, C. Schimpf, R. Trotta, and A. Rastelli, Appl. Phys. Lett. **119**, 120502 (2021).
[97]Z. M. Wang, K. Holmes, Y. I. Mazur, K. A. Ramsey, and G. J. Salamo, Nanoscale Res. Lett. **1**, 57 (2006).
[98]P. Atkinson, E. Zallo, and O. G. Schmidt, J. Appl. Phys. **112**, 054303 (2012).
[99]R. Keil, M. Zopf, Y. Chen, B. Höfer, J. Zhang, F. Ding, and O. G. Schmidt, Nat. Commun. **8**, 15501 (2017).
[100]C. Qian, S. Wu, F. Song, K. Peng, X. Xie, J. Yang, S. Xiao, M. J. Steer, I. G. Thayne, C. Tang, Z. Zuo, K. Jin, C. Gu, and X. Xu, Phys. Rev. Lett. **120**, 213901 (2018).
[101]N. Bart, C. Dangel, P. Zajac, N. Spitzer, J. Ritzmann, M. Schmidt, H. G. Babin, R. Schott, S. R. Valentin, S. Scholz, Y. Wang, R. Uppu, D. Najer, M. C. Löbl, N. Tomm, A. Javadi, N. O. Antoniadis, L. Midolo, K. Müller, R. J. Warburton, P. Lodahl, A. D. Wieck, J. J. Finley, and A. Ludwig, Nat. Commun. **13**, 1633 (2022).
[102]C. Shen, W. Zhan, K. Xin, M. Li, Z. Sun, H. Cong, C. Xu, J. Tang, Z. Wu, B. Xu, Z. Wei, C. Xue, C. Zhao, and Z. Wang, Nat. Commun. **15**, 2724 (2024).
[103]P. Senellart, G. Solomon, and A. White, Nat. Nanotechnol. **12**, 1026 (2017).
[104]E. S. Semenova, R. Hostein, G. Patriarche, O. Mauguin, L. Largeau, I. Robert-Philip, A. Beveratos, and A. Lemaître, J. Appl. Phys. **103**, 103533 (2008).
[105]M. Paul, F. Olbrich, J. Höschele, S. Schreier, J. Kettler, S. L. Portalupi, M. Jetter, and P. Michler, Appl. Phys. Lett. **111**, 033102 (2017).
[106]P. Wyborski, P. Podemski, P. A. Wroński, F. Jabeen, S. Höfling, and G. Sek, Materials **15**, 1071 (2022).
[107]P. Wyborski, M. Gawelczyk, P. Podemski, P. A. Wronski, M. Pawlyta, S. Gorantla, F. Jabeen, S. Höfling, and G. Sek, Phys. Rev. Appl. **20**, 044009 (2023).
[108]A. Musiał, P. Holewa, P. Wyborski, M. Syperek, A. Kors, J. P. Reithmaier, G. Sek, and M. Benyoucef, Adv. Quantum Technol. **3**, 1900082 (2020).
[109]T. Miyazawa, K. Takemoto, Y. Nambu, S. Miki, T. Yamashita, H. Terai, M. Fujiwara, M. Sasaki, Y. Sakuma, M. Takatsu, T. Yamamoto, and Y. Arakawa, Appl. Phys. Lett. **109**, 132106 (2016).
[110]Zon, P. Phienlumlert, S. Thainoi, S. Kiravittaya, A. Tandaechanurat, N. Nuntawong, S. Sopitpan, V. Yordsri, C. Thanachayanont, S. Kanjanachuchai, S. Ratanathammaphan, S. Panyakeow, Y. Ota, S. Iwamoto, and Y. Arakawa, Phys. Status Solidi A **216**, 1800499 (2019).
[111]K. Kawaguchi, M. Ekawa, A. Kuramata, T. Akiyama, H. Ebe, M. Sugawara, and Y. Arakawa, Appl. Phys. Lett. **85**, 4331 (2004).
[112]K. Takemoto, Y. Sakuma, S. Hirose, T. Usuki, N. Yokoyama, T. Miyazawa, M. Takatsu, and Y. Arakawa, Phys. E **26**, 185 (2005).
[113]J. Tatebayashi, S. Iwamoto, S. Kako, S. Ishida, and Y. Arakawa, Jpn. J. Appl. Phys. **42**, 2391 (2003).
[114]J. P. Reithmaier, G. Eisenstein, and A. Forchel, Proc. IEEE **95**, 1779 (2007).
[115]L. Dusanowski, M. Syperek, J. Misiewicz, A. Somers, S. Hofling, M. Kamp, J. P. Reithmaier, and G. Sek, Appl. Phys. Lett. **108**, 163108 (2016).
[116]B. Alloing, C. Zinoni, V. Zwiller, L. H. Li, C. Monat, M. Gobet, G. Buchs, A. Fiore, E. Pelucchi, and E. Kapon, Appl. Phys. Lett. **86**, 101908 (2005).
[117]H. M. Hao, X. B. Su, H. Q. Liu, X. J. Shang, H. Q. Ni, and Z. C. Niu, J. Phys.: Conf. Ser. **2226**, 012006 (2022).
[118]Z. Zon, S. Thainoi, S. Kiravittaya, A. Tandaechanurat, S. Kanjanachuchai, S. Ratanathammaphan, S. Panyakeow, Y. Ota, S. Iwamoto, and Y. Arakawa, J. Appl. Phys. **126**, 084301 (2019).
[119]A. Rastelli, S. Stufler, A. Schliwa, R. Songmuang, C. Manzano, G. Costantini, K. Kern, A. Zrenner, D. Bimberg, and O. G. Schmidt, Phys. Rev. Lett. **92**, 166104 (2004).
[120]W. Zhang, Z. Shi, D. Huo, X. Guo, F. Zhang, L. Chen, Q. Wang, B. Zhang, and C. Peng, Appl. Phys. Lett. **112**, 153108 (2018).
[121]Y.-R. Wang, I. S. Han, and M. Hopkinson, Nanophotonics **12**, 1469 (2023).
[122]C.-W. Shih, I. Limame, C. C. Palekar, A. Koulas-Simos, A. Kaganskiy, P. Klenovský, and S. Reitzenstein, Laser Photonics Rev. **18**, 2301242 (2024).
[123]J. Zhang, S. Chattaraj, S. Lu, and A. Madhukar, J. Appl. Phys. **120**, 243103 (2016).
[124]J. Zhang, Q. Huang, L. Jordao, S. Chattaraj, S. Lu, and A. Madhukar, APL Photonics **5**, 116106 (2020).

[125]M. Felici, P. Gallo, A. Mohan, B. Dwir, A. Rudra, and E. Kapon, Small **5**, 938 (2009).
[126]M. Blumin, H. E. Ruda, I. G. Savelyev, A. Shik, and H. Wang, J. Appl. Phys. **99**, 093518 (2006).
[127]S. Birudavolu, N. Nuntawong, G. Balakrishnan, Y. C. Xin, S. Huang, S. C. Lee, S. R. J. Brueck, C. P. Hains, and D. L. Huffaker, Appl. Phys. Lett. **85**, 2337 (2004).
[128]C. Schneider, A. Huggenberger, M. Gschrey, P. Gold, S. Rodt, A. Forchel, S. Reitzenstein, S. Höfling, and M. Kamp, Phys. Status Solidi A **209**, 2379 (2012).
[129]C. Schneider, A. Huggenberger, T. Sünner, T. Heindel, M. Strauß, S. Göpfert, P. Weinmann, S. Reitzenstein, L. Worschech, M. Kamp, S. Höfling, and A. Forchel, Nanotechnology **20**, 434012 (2009).
[130]A. Huggenberger, C. Schneider, C. Drescher, S. Heckelmann, T. Heindel, S. Reitzenstein, M. Kamp, S. Höfling, L. Worschech, and A. Forchel, Cryst. Growth **323**, 194 (2011).
[131]A. Huggenberger, S. Heckelmann, C. Schneider, S. Höfling, S. Reitzenstein, L. Worschech, M. Kamp, and A. Forchel, Appl. Phys. Lett. **98**, 131104 (2011).
[132]I. S. Han, Y.-R. Wang, and M. Hopkinson, Appl. Phys. Lett. **118**, 142101 (2021).
[133]Y.-R. Wang, I. S. Han, C.-Y. Jin, and M. Hopkinson, Appl. Phys. Lett. **116**, 201901 (2020).
[134]S. Tomić, J. Pal, M. A. Migliorato, R. J. Young, and N. Vukmirović, ACS Photonics **2**, 958 (2015).
[135]C. C. Ahia, N. Tile, A. Navarro, B. G. Blanco, and J. R. Botha, AIP Adv. **8**, 075004 (2018).
[136]K. Xin, L. Li, Z. Zhou, C. Zhang, J. Yang, H.-X. Deng, J. Zhang, J. Liu, K. Liu, C. Liu, F. Liu, Z. Wei, and S. Zhai, Nat. Synth. **3**, 1176 (2024).
[137]I. Limame, C.-W. Shih, A. Koltchanov, F. Heisinger, F. Nippert, M. Plattner, J. Schall, M. R. Wagner, S. Rodt, P. Klenovsky, and S. Reitzenstein, Appl. Phys. Lett. **124**, 061102 (2024).
[138]J. Große, M. von Helversen, A. Koulas-Simos, M. Hermann, and S. Reitzenstein, APL Photonics **5**, 096107 (2020).
[139]A. Kaganskiy, F. Gericke, T. Heuser, T. Heindel, X. Porte, and S. Reitzenstein, Appl. Phys. Lett. **112**, 071101 (2018).
[140]M. Strauß, A. Kaganskiy, R. Voigt, P. Schnauber, J.-H. Schulze, S. Rodt, A. Strittmatter, and S. Reitzenstein, Appl. Phys. Lett. **110**, 111101 (2017).
[141]A. Strittmatter, A. Schliwa, J.-H. Schulze, T. D. Germann, A. Dreismann, O. Hitzemann, E. Stock, I. A. Ostapenko, S. Rodt, W. Unrau, U. W. Pohl, A. Hoffmann, D. Bimberg, and V. Haisler, Appl. Phys. Lett. **100**, 093111 (2012).
[142]A. Strittmatter, A. Holzbecher, A. Schliwa, J.-H. Schulze, D. Quandt, T. D. Germann, A. Dreismann, O. Hitzemann, E. Stock, I. A. Ostapenko, S. Rodt, W. Unrau, U. W. Pohl, A. Hoffmann, D. Bimberg, and V. Haisler, Phys. Status Solidi A **209**, 2411 (2012).
[143]M. Podhorsky, M. Klonz, I. Limame, S. Tripathi, K. Gaur, C. C. Palekar, P. Mudi, P. Klenovsky, S. Rodt, and S. Reitzenstein, Phys. Conf. Ser. **2931**, 012016 (2024).
[144]J. Zhang, Z. Lingley, S. Lu, and A. Madhukar, J. Vac. Sci. Technol. B **32**, 02C106 (2014).
[145]M. J. Holmes, K. Choi, S. Kako, M. Arita, and Y. Arakawa, Nano Lett. **14**, 982 (2014).
[146]D. Dalacu, K. Mnaymneh, J. Lapointe, X. Wu, P. J. Poole, G. Bulgarini, V. Zwiller, and M. E. Reimer, Nano Lett. **12**, 5919 (2012).
[147]S. Haffouz, K. D. Zeuner, D. Dalacu, P. J. Poole, J. Lapointe, D. Poitras, K. Mnaymneh, X. Wu, M. Couillard, M. Korkusinski, E. Schöll, K. D. Jöns, R. L. Zwiller, and R. L. Williams, Nano Lett. **18**, 3047 (2018).
[148]P. Yu, Z. Li, T. Wu, Y.-T. Wang, X. Tong, C.-F. Li, Z. Wang, S.-H. Wei, Y. Zhang, H. Liu, L. Fu, Y. Zhang, J. Wu, H. H. Tan, C. Jagadish, and Z. M. Wang, ACS Nano **13**, 13492 (2019).
[149]I. Geijselaers, N. Vainorius, S. Lehmann, C. E. Pryor, K. A. Dick, and M.-E. Pistol, Appl. Phys. Lett. **119**, 263102 (2021).
[150]M. Bouwes Bavinck, K. D. Jöns, M. Zieliński, G. Patriarche, J.-C. Harmand, N. Akopian, and V. Zwiller, Nano Lett. **16**, 1081 (2016).
[151]M. Kunrugsa, S. Kiravittaya, S. Sopitpan, S. Ratanathammaphan, and S. Panyakeow, J. Cryst. Growth **401**, 441 (2014).
[152]E. Alphandéry, R. J. Nicholas, N. J. Mason, S. G. Lyapin, and P. C. Klipstein, Phys. Rev. B **65**, 115322 (2002).
[153]S. Shusterman, Y. Paltiel, A. Sher, V. Ezersky, and Y. Rosenwaks, J. Cryst. Growth **291**, 363 (2006).
[154]V. Tasco, N. Deguffroy, A. N. Baranov, E. Tournié, B. Satpati, A. Trampert, M. S. Dunaevskii, and A. Titkov, Appl. Phys. Lett. **89**, 263118 (2006).
[155]M. A. M. Versteegh, M. E. Reimer, K. D. Jöns, D. Dalacu, P. J. Poole, A. Gulinatti, A. Giudice, and V. Zwiller, Nat. Commun. **5**, 5298 (2014).
[156]J. Claudon, J. Bleuse, N. S. Malik, M. Bazin, P. Jaffrennou, N. Gregersen, C. Sauvan, P. Lalanne, and J.-M. Gérard, Nat. Photonics **4**, 174 (2010).
[157]Y. Zhang, A. V. Velichko, H. A. Fonseka, P. Parkinson, J. A. Gott, G. Davis, M. Aagesen, A. M. Sanchez, D. Mowbray, and H. Liu, Nano Lett. **21**, 5722 (2021).
[158]M. J. Holmes, M. Arita, and Y. Arakawa, Semicond. Sci. Technol. **34**, 033001 (2019).
[159]S. Wu, K. Peng, S. Battiato, V. Zannier, A. Bertoni, G. Goldoni, X. Xie, J. Yang, S. Xiao, C. Qian, F. Song, S. Sun, J. Dang, Y. Yu, F. Beltram, L. Sorba, A. Li, B. B. Li, F. Rossella, and X. Xu, Nano Res. **12**, 2842 (2019).
[160]K. Peng, S. Wu, X. Xie, J. Yang, C. Qian, F. Song, S. Sun, J. Dang, Y. Yu, S. Shi, J. He, and X. Xu, Phys. Rev. Appl. **11**, 024015 (2019).
[161]K. Peng, S. Wu, X. Xie, J. Yang, C. Qian, F. Song, S. Sun, J. Dang, Y. Yu, S. Xiao, and X. Xu, Appl. Phys. Lett. **114**, 091109 (2019).
[162]T. Belhadj, T. Amand, A. Kunold, C.-M. Simon, T. Kuroda, M. Abbarchi, T. Mano, K. Sakoda, S. Kunz, X. Marie, and B. Urbaszek, Appl. Phys. Lett. **97**, 051111 (2010).
[163]K. F. Karlsson, M. A. Dupertuis, D. Y. Oberli, E. Pelucchi, A. Rudra, P. O. Holtz, and E. Kapon, Phys. Rev. B **81**, 161307 (2010).
[164]Y. H. Huo, B. J. Witek, S. Kumar, J. R. Cardenas, J. X. Zhang, N. Akopian, R. Singh, E. Zallo, R. Grifone, D. Kriegner, R. Trotta, F. Ding, J. Stangl, V. Zwiller, G. Bester, A. Rastelli, and O. G. Schmidt, Nat. Phys. **10**, 46 (2014).
[165]J. Zhang, Y. Huo, A. Rastelli, M. Zopf, B. Höfer, Y. Chen, F. Ding, and O. G. Schmidt, Nano Lett. **15**, 422 (2015).
[166]M. Zieliński, Phys. Rev. B **88**, 115424 (2013).
[167]M. Jeannin, A. Artioli, P. Rueda-Fonseca, E. Bellet-Amalric, K. Kheng, R. André, S. Tatarenko, J. Cibert, D. Ferrand, and G. Nogues, Phys. Rev. B **95**, 035305 (2017).
[168]G. Pirard, F. B. Basset, S. Bietti, S. Sanguinetti, R. Trotta, and G. Bester, Phys. Rev. B **107**, 205417 (2023).
[169]N. R. S. van Venrooij, A. R. da Cruz, R. S. R. Gajjela, P. M. Koenraad, C. E. Pryor, and M. E. Flatté, Phys. Rev. B **109**, L201405 (2024).
[170]Y. Toda, O. Moriwaki, M. Nishioka, and Y. Arakawa, Phys. Rev. Lett. **82**, 4114 (1999).
[171]O. Gazzano, S. Michaelis de Vasconcellos, C. Arnold, A. Nowak, E. Galopin, I. Sagnes, L. Lanco, A. Lemaître, and P. Senellart, Nat. Commun. **4**, 1425 (2013).
[172]P. Gold, A. Thoma, S. Maier, S. Reitzenstein, C. Schneider, S. Höfling, and M. Kamp, Phys. Rev. B **89**, 035313 (2014).
[173]J. D. Mar, X. L. Xu, J. J. Baumberg, F. S. F. Brossard, A. C. Irvine, C. Stanley, and D. A. Williams, Phys. Rev. B **83**, 075306 (2011).
[174]R. J. Warburton, C. S. Dürr, K. Karrai, J. P. Kotthaus, G. Medeiros-Ribeiro, and P. M. Petroff, Phys. Rev. Lett. **79**, 5282 (1997).
[175]S. Rodt, R. Heitz, A. Schliwa, R. L. Sellin, F. Guffarth, and D. Bimberg, Phys. Rev. B **68**, 035331 (2003).
[176]A. Zrenner, E. Beham, S. Stufler, F. Findeis, M. Bichler, and G. Abstreiter, Nature **418**, 612 (2002).
[177]Z. Yuan, B. E. Kardynal, R. M. Stevenson, A. J. Shields, C. J. Lobo, K. Cooper, N. S. Beattie, D. A. Ritchie, and M. Pepper, Science **295**, 102 (2002).
[178]X. Xu, D. A. Williams, and J. R. A. Cleaver, Appl. Phys. Lett. **85**, 3238 (2004).
[179]A. J. Bennett, R. B. Patel, A. J. Shields, K. Cooper, P. Atkinson, C. A. Nicoll, and D. A. Ritchie, Appl. Phys. Lett. **92**, 193503 (2008).
[180]R. B. Patel, A. J. Bennett, K. Cooper, P. Atkinson, C. A. Nicoll, D. A. Ritchie, and A. J. Shields, Phys. Rev. Lett. **100**, 207405 (2008).
[181]C. Spinnler, L. Zhai, G. N. Nguyen, J. Ritzmann, A. D. Wieck, A. Ludwig, A. Javadi, D. E. Reiter, P. Machnikowski, R. J. Warburton, and M. C. Löbl, Nat. Commun. **12**, 6575 (2021).
[182]J.-Y. Yan, C. Chen, X.-D. Zhang, Y.-T. Wang, H.-G. Babin, A. D. Wieck, A. Ludwig, Y. Meng, X. Hu, H. Duan, W. Chen, W. Fang, M. Cygorek, X. Lin, D.-W. Wang, C.-Y. Jin, and F. Liu, Nat. Nanotechnol. **18**, 1139 (2023).
[183]A. V. Kuhlmann, J. H. Prechtel, J. Houel, A. Ludwig, D. Reuter, A. D. Wieck, and R. J. Warburton, Nat. Commun. **6**, 8204 (2015).
[184]R. Heitz, M. Veit, N. N. Ledentsov, A. Hoffmann, D. Bimberg, V. M. Ustinov, P. S. Kop'ev, and Z. I. Alferov, Phys. Rev. B **56**, 10435 (1997).
[185]M. Davanço, C. S. Hellberg, S. Ates, A. Badolato, and K. Srinivasan, Phys. Rev. B **89**, 161303 (2014).

[186]X. Y. Wang, W. Q. Ma, J. Y. Zhang, G. J. Salamo, M. Xiao, and C. K. Shih, Nano Lett. **5**, 1873 (2005).
[187]A. Kurzmann, A. Ludwig, A. D. Wieck, A. Lorke, and M. Geller, Nano Lett. **16**, 3367 (2016).
[188]M. C. Löbl, C. Spinnler, A. Javadi, L. Zhai, G. N. Nguyen, J. Ritzmann, L. Midolo, P. Lodahl, A. D. Wieck, A. Ludwig, and R. J. Warburton, Nat. Nanotechnol. **15**, 558 (2020).
[189]K. Gawarecki, C. Spinnler, L. Zhai, G. N. Nguyen, A. Ludwig, R. J. Warburton, M. C. Löbl, D. E. Reiter, and P. Machnikowski, Phys. Rev. B **108**, 235410 (2023).
[190]M. Reindl, J. H. Weber, D. Huber, C. Schimpf, S. F. Covre Da Silva, S. L. Portalupi, R. Trotta, P. Michler, and A. Rastelli, Phys. Rev. B **100**, 155420 (2019).
[191]B. Krummheuer, V. M. Axt, and T. Kuhn, Phys. Rev. B **65**, 195313 (2002).
[192]D. E. Reiter, T. Kuhn, and V. M. Axt, Adv. Phys. X **4**, 1655478 (2019).
[193]J. Houel, A. V. Kuhlmann, L. Greuter, F. Xue, M. Poggio, B. D. Gerardot, P. A. Dalgarno, A. Badolato, P. M. Petroff, A. Ludwig, D. Reuter, A. D. Wieck, and R. J. Warburton, Phys. Rev. Lett. **108**, 107401 (2012).
[194]A. V. Kuhlmann, J. Houel, A. Ludwig, L. Greuter, D. Reuter, A. D. Wieck, M. Poggio, and R. J. Warburton, Nat. Phys. **9**, 570 (2013).
[195]B. Urbaszek, X. Marie, T. Amand, O. Krebs, P. Voisin, P. Maletinsky, A. Högele, and A. Imamoglu, Rev. Mod. Phys. **85**, 79 (2013).
[196]P.-F. Braun, X. Marie, L. Lombez, B. Urbaszek, T. Amand, P. Renucci, V. K. Kalevich, K. V. Kavokin, O. Krebs, P. Voisin, and Y. Masumoto, Phys. Rev. Lett. **94**, 116601 (2005).
[197]R. N. E. Malein, T. S. Santana, J. M. Zajac, A. C. Dada, E. M. Gauger, P. M. Petroff, J. Y. Lim, J. D. Song, and B. D. Gerardot, Phys. Rev. Lett. **116**, 257401 (2016).
[198]J. H. Prechtel, A. V. Kuhlmann, J. Houel, L. Greuter, A. Ludwig, D. Reuter, A. D. Wieck, and R. J. Warburton, Phys. Rev. X **3**, 041006 (2013).
[199]J. Hansom, C. H. H. Schulte, C. Le Gall, C. Matthiesen, E. Clarke, M. Hugues, J. M. Taylor, and M. Atatüre, Nat. Phys. **10**, 725 (2014).
[200]P. Borri, W. Langbein, S. Schneider, U. Woggon, R. Sellin, D. Ouyang, and D. Bimberg, Phys. Rev. Lett. **87**, 157401 (2001).
[201]E. A. Muljarov and R. Zimmermann, Phys. Rev. Lett. **93**, 237401 (2004).
[202]A. J. Ramsay, A. V. Gopal, E. M. Gauger, A. Nazir, B. W. Lovett, A. M. Fox, and M. S. Skolnick, Phys. Rev. Lett. **104**, 017402 (2010).
[203]A. Thoma, P. Schnauber, M. Gschrey, M. Seifried, J. Wolters, J.-H. Schulze, A. Strittmatter, S. Rodt, A. Carmele, A. Knorr, T. Heindel, and S. Reitzenstein, Phys. Rev. Lett. **116**, 033601 (2016).
[204]A. Reigue, J. Iles-Smith, F. Lux, L. Monniello, M. Bernard, F. Margaillan, A. Lemaitre, A. Martinez, D. P. McCutcheon, J. Mørk, R. Hostein, and V. Voliotis, Phys. Rev. Lett. **118**, 233602 (2017).
[205]S. Varoutsis, S. Laurent, P. Kramper, A. Lemaître, I. Sagnes, I. Robert-Philip, and I. Abram, Phys. Rev. B **72**, 041303 (2005).
[206]P. Kaer, N. Gregersen, and J. Mork, New J. Phys. **15**, 035027 (2013).
[207]T. Grange, N. Somaschi, C. Antón, L. De Santis, G. Coppola, V. Giesz, A. Lemaître, I. Sagnes, A. Auffèves, and P. Senellart, Phys. Rev. Lett. **118**, 253602 (2017).
[208]J. Iles-Smith, D. P. S. McCutcheon, A. Nazir, and J. Mørk, Nat. Photonics **11**, 521 (2017).
[209]A. J. Brash, J. Iles-Smith, C. L. Phillips, D. P. S. McCutcheon, J. O'Hara, E. Clarke, B. Royall, L. R. Wilson, J. Mørk, M. S. Skolnick, A. M. Fox, and A. Nazir, Phys. Rev. Lett. **123**, 167403 (2019).
[210]S. Liu, C. Gustin, H. Liu, X. Li, Y. Yu, H. Ni, Z. Niu, S. Hughes, X. Wang, and J. Liu, Nat. Photonics **18**, 318 (2024).
[211]Y. Wu, I. M. Piper, M. Ediger, P. Brereton, E. R. Schmidgall, P. R. Eastham, M. Hugues, M. Hopkinson, and R. T. Phillips, Phys. Rev. Lett. **106**, 067401 (2011).
[212]W. Heitler, *The Quantum Theory of Radiation* (Courier Corporation, 1984).
[213]B. R. Mollow, Phys. Rev. **188**, 1969 (1969).
[214]H. S. Nguyen, G. Sallen, C. Voisin, P. Roussignol, C. Diederichs, and G. Cassabois, Appl. Phys. Lett. **99**, 261904 (2011).
[215]C. Matthiesen, A. N. Vamivakas, and M. Atatüre, Phys. Rev. Lett. **108**, 093602 (2012).
[216]R. Proux, M. Maragkou, E. Baudin, C. Voisin, P. Roussignol, and C. Diederichs, Phys. Rev. Lett. **114**, 067401 (2015).
[217]C. Matthiesen, M. Geller, C. H. H. Schulte, C. Le Gall, J. Hansom, Z. Li, M. Hugues, E. Clarke, and M. Atatüre, Nat. Commun. **4**, 1600 (2013).
[218]A. J. Bennett, J. P. Lee, D. J. P. Ellis, T. Meany, E. Murray, F. F. Floether, J. P. Griffths, I. Farrer, D. A. Ritchie, and A. J. Shields, Sci. Adv. **2**, e1501256 (2016).
[219]K. Konthasinghe, J. Walker, M. Peiris, C. K. Shih, Y. Yu, M. F. Li, J. F. He, L. J. Wang, H. Q. Ni, Z. C. Niu, and A. Muller, Phys. Rev. B **85**, 235315 (2012).
[220]D. P. S. McCutcheon and A. Nazir, Phys. Rev. Lett. **110**, 217401 (2013).
[221]Z. X. Koong, D. Scerri, M. Rambach, T. S. Santana, S. I. Park, J. D. Song, E. M. Gauger, and B. D. Gerardot, Phys. Rev. Lett. **123**, 167402 (2019).
[222]G. Fernandez, T. Volz, R. Desbuquois, A. Badolato, and A. Imamoglu, Phys. Rev. Lett. **103**, 087406 (2009).
[223]Y. He, Y.-M. He, Y.-J. Wei, X. Jiang, M.-C. Chen, F.-L. Xiong, Y. Zhao, C. Schneider, M. Kamp, S. Höfling, C.-Y. Lu, and J.-W. Pan, Phys. Rev. Lett. **111**, 237403 (2013).
[224]T. M. Sweeney, S. G. Carter, A. S. Bracker, M. Kim, C. S. Kim, L. Yang, P. M. Vora, P. G. Brereton, E. R. Cleveland, and D. Gammon, Nat. Photonics **8**, 442 (2014).
[225]A. Muller, E. B. Flagg, P. Bianucci, X. Y. Wang, D. G. Deppe, W. Ma, J. Zhang, G. J. Salamo, M. Xiao, and C. K. Shih, Phys. Rev. Lett. **99**, 187402 (2007).
[226]A. Muller, W. Fang, J. Lawall, and G. S. Solomon, Phys. Rev. Lett. **101**, 027401 (2008).
[227]E. B. Flagg, A. Muller, J. W. Robertson, S. Founta, D. G. Deppe, M. Xiao, W. Ma, G. J. Salamo, and C. K. Shih, Nat. Phys. **5**, 203 (2009).
[228]A. Nick Vamivakas, Y. Zhao, C.-Y. Lu, and M. Atatüre, Nat. Phys. **5**, 198 (2009).
[229]S. Ates, S. M. Ulrich, S. Reitzenstein, A. Löffler, A. Forchel, and P. Michler, Phys. Rev. Lett. **103**, 167402 (2009).
[230]S. Unsleber, S. Maier, D. P. S. McCutcheon, Y.-M. He, M. Dambach, M. Gschrey, N. Gregersen, J. Mørk, S. Reitzenstein, S. Höfling, C. Schneider, and M. Kamp, Optica **2**, 1072 (2015).
[231]X. Xu, B. Sun, P. R. Berman, D. G. Steel, A. S. Bracker, D. Gammon, and L. J. Sham, Science **317**, 929 (2007).
[232]G. Jundt, L. Robledo, A. Högele, S. Fält, and A. Imamoğlu, Phys. Rev. Lett. **100**, 177401 (2008).
[233]S. J. Boyle, A. J. Ramsay, A. M. Fox, M. S. Skolnick, A. P. Heberle, and M. Hopkinson, Phys. Rev. Lett. **102**, 207401 (2009).
[234]L. Dusanowski, C. Gustin, S. Hughes, C. Schneider, and S. Höfling, Nano Lett. **22**, 3562 (2022).
[235]A. Ulhaq, S. Weiler, S. M. Ulrich, R. Roßbach, M. Jetter, and P. Michler, Nat. Photonics **6**, 238 (2012).
[236]S. M. Ulrich, S. Ates, S. Reitzenstein, A. Löffler, A. Forchel, and P. Michler, Phys. Rev. Lett. **106**, 247402 (2011).
[237]C. Roy and S. Hughes, Phys. Rev. Lett. **106**, 247403 (2011).
[238]Y.-J. Wei, Y. He, Y.-M. He, C.-Y. Lu, J.-W. Pan, C. Schneider, M. Kamp, S. Höfling, D. P. S. McCutcheon, and A. Nazir, Phys. Rev. Lett. **113**, 097401 (2014).
[239]Y. He, Y.-M. He, J. Liu, Y.-J. Wei, H. Ramírez, M. Atatüre, C. Schneider, M. Kamp, S. Höfling, C.-Y. Lu, and J.-W. Pan, Phys. Rev. Lett. **114**, 097402 (2015).
[240]F. Hargart, M. Müller, K. Roy-Choudhury, S. L. Portalupi, C. Schneider, S. Höfling, M. Kamp, S. Hughes, and P. Michler, Phys. Rev. B **93**, 115308 (2016).
[241]K. G. Lagoudakis, K. A. Fischer, T. Sarmiento, P. L. McMahon, M. Radulaski, J. L. Zhang, Y. Kelaita, C. Dory, K. Müller, and J. Vučković, Phys. Rev. Lett. **118**, 013602 (2017).
[242]B. Wu, X.-J. Wang, L. Liu, G. Huang, W. Wang, H. Liu, H. Ni, Z. Niu, and Z. Yuan, Optica **10**, 1118 (2023).
[243]A. Moelbjerg, P. Kaer, M. Lorke, and J. Mørk, Phys. Rev. Lett. **108**, 017401 (2012).
[244]K. A. Fischer, K. Müller, A. Rundquist, T. Sarmiento, A. Y. Piggott, Y. Kelaita, C. Dory, K. G. Lagoudakis, and J. Vučković, Nat. Photonics **10**, 163 (2016).
[245]K. Boos, S. K. Kim, T. Bracht, F. Sbresny, J. M. Kaspari, M. Cygorek, H. Riedl, F. W. Bopp, W. Rauhaus, C. Calcagno, J. J. Finley, D. E. Reiter, and K. Müller, Phys. Rev. Lett. **132**, 053602 (2024).
[246]M. O. Scully and M. S. Zubairy, *Quantum Optics* (Cambridge University Press, 1997).
[247]R. Melet, V. Voliotis, A. Enderlin, D. Roditchev, X. L. Wang, T. Guillet, and R. Grousson, Phys. Rev. B **78**, 073301 (2008).

[248]T. H. Stievater, X. Li, D. G. Steel, D. Gammon, D. S. Katzer, D. Park, C. Piermarocchi, and L. J. Sham, Phys. Rev. Lett. **87**, 133603 (2001).
[249]X. Li, Y. Wu, D. Steel, D. Gammon, T. H. Stievater, D. S. Katzer, D. Park, C. Piermarocchi, and L. J. Sham, Science **301**, 809 (2003).
[250]J. Förstner, C. Weber, J. Danckwerts, and A. Knorr, Phys. Rev. Lett. **91**, 127401 (2003).
[251]A. J. Ramsay, T. M. Godden, S. J. Boyle, E. M. Gauger, A. Nazir, B. W. Lovett, A. M. Fox, and M. S. Skolnick, Phys. Rev. Lett. **105**, 177402 (2010).
[252]L. Monniello, C. Tonin, R. Hostein, A. Lemaitre, A. Martinez, V. Voliotis, and R. Grousson, Phys. Rev. Lett. **111**, 026403 (2013).
[253]Y.-M. He, Y. He, Y.-J. Wei, D. Wu, M. Atatüre, C. Schneider, S. Höfling, M. Kamp, C.-Y. Lu, and J.-W. Pan, Nat. Nanotechnol. **8**, 213 (2013).
[254]E. Schöll, L. Hanschke, L. Schweickert, K. D. Zeuner, M. Reindl, S. F. Covre da Silva, T. Lettner, R. Trotta, J. J. Finley, K. Müller, A. Rastelli, V. Zwiller, and K. D. Jöns, Nano Lett. **19**, 2404 (2019).
[255]C. H. H. Schulte, J. Hansom, A. E. Jones, C. Matthiesen, C. Le Gall, and M. Atatüre, Nature **525**, 222 (2015).
[256]H. Wang, J. Qin, S. Chen, M.-C. Chen, X. You, X. Ding, Y.-H. Huo, Y. Yu, C. Schneider, S. Höfling, M. Scully, C.-Y. Lu, and J.-W. Pan, Phys. Rev. Lett. **125**, 153601 (2020).
[257]K. A. Fischer, L. Hanschke, J. Wierzbowski, T. Simmet, C. Dory, J. J. Finley, J. Vučković, and K. Müller, Nat. Phys. **13**, 649 (2017).
[258]J. C. Loredo, C. Antón, B. Reznychenko, P. Hilaire, A. Harouri, C. Millet, H. Ollivier, N. Somaschi, L. De Santis, A. Lemaître, I. Sagnes, L. Lanco, A. Auffèves, O. Krebs, and P. Senellart, Nat. Photonics **13**, 803 (2019).
[259]S. C. Wein, J. C. Loredo, M. Maffei, P. Hilaire, A. Harouri, N. Somaschi, A. Lemaître, I. Sagnes, L. Lanco, O. Krebs, A. Auffèves, C. Simon, P. Senellart, and C. Antón-Solanas, Nat. Photonics **16**, 374 (2022).
[260]C. Matthiesen, M. J. Stanley, M. Hugues, E. Clarke, and M. Atatüre, Sci. Rep. **4**, 4911 (2014).
[261]Y.-M. He, H. Wang, C. Wang, M.-C. Chen, X. Ding, J. Qin, Z.-C. Duan, S. Chen, J.-P. Li, R.-Z. Liu, C. Schneider, M. Atatüre, S. Höfling, C.-Y. Lu, and J.-W. Pan, Nat. Phys. **15**, 941 (2019).
[262]S. Wu, K. Peng, X. Xie, J. Yang, S. Xiao, F. Song, J. Dang, S. Sun, L. Yang, Y. Wang, S. Shi, J. He, Z. Zuo, and X. Xu, Phys. Rev. Appl. **14**, 014049 (2020).
[263]K. Peng, S. Wu, J. Tang, F. Song, C. Qian, S. Sun, S. Xiao, M. Wang, H. Ali, D. A. Williams, and X. Xu, Phys. Rev. Appl. **8**, 064018 (2017).
[264]Y. Zhang, Y. Chen, M. Mietschke, L. Zhang, F. Yuan, S. Abel, R. Hühne, K. Nielsch, J. Fompeyrine, F. Ding, and O. G. Schmidt, Nano Lett. **16**, 5785 (2016).
[265]R. A. DeCrescent, Z. Wang, J. T. Bush, P. Imany, A. Kwiatkowski, D. V. Reddy, S. W. Nam, R. P. Mirin, and K. L. Silverman, Optica **11**, 1526 (2024).
[266]C.-M. Simon, T. Belhadj, B. Chatel, T. Amand, P. Renucci, A. Lemaitre, O. Krebs, P. A. Dalgarno, R. J. Warburton, X. Marie, and B. Urbaszek, Phys. Rev. Lett. **106**, 166801 (2011).
[267]Y.-J. Wei, Y.-M. He, M.-C. Chen, Y.-N. Hu, Y. He, D. Wu, C. Schneider, M. Kamp, S. Höfling, C.-Y. Lu, and J.-W. Pan, Nano Lett. **14**, 6515 (2014).
[268]R. Mathew, E. Dilcher, A. Gamouras, A. Ramachandran, H. Y. S. Yang, S. Freisem, D. Deppe, and K. C. Hall, Phys. Rev. B **90**, 035316 (2014).
[269]T. Kaldewey, S. Lüker, A. V. Kuhlmann, S. R. Valentin, A. Ludwig, A. D. Wieck, D. E. Reiter, T. Kuhn, and R. J. Warburton, Phys. Rev. B **95**, 161302 (2017).
[270]T. Kaldewey, S. Lüker, A. V. Kuhlmann, S. R. Valentin, J.-M. Chauveau, A. Ludwig, A. D. Wieck, D. E. Reiter, T. Kuhn, and R. J. Warburton, Phys. Rev. B **95**, 241306 (2017).
[271]A. Debnath, C. Meier, B. Chatel, and T. Amand, Phys. Rev. B **86**, 161304 (2012).
[272]E. R. Schmidgall, P. R. Eastham, and R. T. Phillips, Phys. Rev. B **81**, 195306 (2010).
[273]A. Ramachandran, G. R. Wilbur, R. Mathew, A. Mason, S. O'Neal, D. G. Deppe, and K. C. Hall, Sci. Rep. **14**, 5356 (2024).
[274]T. Kaldewey, A. V. Kuhlmann, S. R. Valentin, A. Ludwig, A. D. Wieck, and R. J. Warburton, Nat. Photonics **12**, 68 (2018).
[275]G. R. Wilbur, A. Binai-Motlagh, A. Clarke, A. Ramachandran, N. Milson, J. P. Healey, S. O'Neal, D. G. Deppe, and K. C. Hall, APL Photonics **7**, 111302 (2022).
[276]Y. Karli, R. Schwarz, F. Kappe, D. A. Vajner, R. G. Krämer, T. K. Bracht, S. F. Covre da Silva, D. Richter, S. Nolte, A. Rastelli, D. E. Reiter, G. Weihs, T. Heindel, and V. Remesh, Appl. Phys. Lett. **125**, 254002 (2024).
[277]F. Kappe, Y. Karli, G. Wilbur, R. G. Krämer, S. Ghosh, R. Schwarz, M. Kaiser, T. K. Bracht, D. E. Reiter, S. Nolte, K. C. Hall, G. Weihs, and V. Remesh, Adv. Quantum Technol. **8**, 2300352 (2025).
[278]M. Glässl, A. M. Barth, and V. M. Axt, Phys. Rev. Lett. **110**, 147401 (2013).
[279]P.-L. Ardelt, L. Hanschke, K. A. Fischer, K. Müller, A. Kleinkauf, M. Koller, A. Bechtold, T. Simmet, J. Wierzbowski, H. Riedl, G. Abstreiter, and J. J. Finley, Phys. Rev. B **90**, 241404 (2014).
[280]S. Bounouar, M. Müller, A. M. Barth, M. Glässl, V. M. Axt, and P. Michler, Phys. Rev. B **91**, 161302 (2015).
[281]J. H. Quilter, A. J. Brash, F. Liu, M. Glässl, A. M. Barth, V. M. Axt, A. J. Ramsay, M. S. Skolnick, and A. M. Fox, Phys. Rev. Lett. **114**, 137401 (2015).
[282]F. Liu, L. M. P. Martins, A. J. Brash, A. M. Barth, J. H. Quilter, V. M. Axt, M. S. Skolnick, and A. M. Fox, Phys. Rev. B **93**, 161407 (2016).
[283]M. Reindl, K. D. Jöns, D. Huber, C. Schimpf, Y. Huo, V. Zwiller, A. Rastelli, and R. Trotta, Nano Lett. **17**, 4090 (2017).
[284]T. K. Bracht, M. Cosacchi, T. Seidelmann, M. Cygorek, A. Vagov, V. M. Axt, T. Heindel, and D. E. Reiter, PRX Quantum **2**, 040354 (2021).
[285]Y. Karli, F. Kappe, V. Remesh, T. K. Bracht, J. Münzberg, S. Covre da Silva, T. Seidelmann, V. M. Axt, A. Rastelli, D. E. Reiter, and G. Weihs, Nano Lett. **22**, 6567 (2022).
[286]A. Högele, S. Seidl, M. Kroner, K. Karrai, R. J. Warburton, B. D. Gerardot, and P. M. Petroff, Phys. Rev. Lett. **93**, 217401 (2004).
[287]A. J. Bennett, R. B. Patel, J. Skiba-Szymanska, C. A. Nicoll, I. Farrer, D. A. Ritchie, and A. J. Shields, Appl. Phys. Lett. **97**, 031104 (2010).
[288]A. J. Bennett, M. A. Pooley, R. M. Stevenson, M. B. Ward, R. B. Patel, A. B. de la Giroday, N. Sköld, I. Farrer, C. A. Nicoll, D. A. Ritchie, and A. J. Shields, Nat. Phys. **6**, 947 (2010).
[289]M. A. Pooley, A. J. Bennett, R. M. Stevenson, A. J. Shields, I. Farrer, and D. A. Ritchie, Phys. Rev. Appl. **1**, 024002 (2014).
[290]H. Ollivier, P. Priya, A. Harouri, I. Sagnes, A. Lemaître, O. Krebs, L. Lanco, N. D. Lanzillotti-Kimura, M. Esmann, and P. Senellart, Phys. Rev. Lett. **129**, 057401 (2022).
[291]B. D. Gerardot, S. Seidl, P. A. Dalgarno, R. J. Warburton, D. Granados, J. M. Garcia, K. Kowalik, O. Krebs, K. Karrai, A. Badolato, and P. M. Petroff, Appl. Phys. Lett. **90**, 041101 (2007).
[292]M. M. Vogel, S. M. Ulrich, R. Hafenbrak, P. Michler, L. Wang, A. Rastelli, and O. G. Schmidt, Appl. Phys. Lett. **91**, 051904 (2007).
[293]J. D. Mar, X. L. Xu, J. S. Sandhu, A. C. Irvine, M. Hopkinson, and D. A. Williams, Appl. Phys. Lett. **97**, 221108 (2010).
[294]L. Zhai, M. C. Löbl, G. N. Nguyen, J. Ritzmann, A. Javadi, C. Spinnler, A. D. Wieck, A. Ludwig, and R. J. Warburton, Nat. Commun. **11**, 4745 (2020).
[295]G. Undeutsch, M. Aigner, A. J. J. Garcia, J. Reindl, M. Peter, S. Mader, C. Weidinger, S. F. Covre da Silva, S. Manna, E. Schöll, and A. Rastelli, Nano Lett. **25**, 7121 (2025).
[296]R. B. Patel, A. J. Bennett, I. Farrer, C. A. Nicoll, D. A. Ritchie, and A. J. Shields, Nat. Photonics **4**, 632 (2010).
[297]L. Zhai, G. N. Nguyen, C. Spinnler, J. Ritzmann, M. C. Löbl, A. D. Wieck, A. Ludwig, A. Javadi, and R. J. Warburton, Nat. Nanotechnol. **17**, 829 (2022).
[298]T. Unold, K. Mueller, C. Lienau, T. Elsaesser, and A. D. Wieck, Phys. Rev. Lett. **92**, 157401 (2004).
[299]A. Muller, W. Fang, J. Lawall, and G. S. Solomon, Phys. Rev. Lett. **103**, 217402 (2009).
[300]J. Tang, S. Cao, Y. Gao, Y. Sun, W. Geng, D. A. Williams, K. Jin, and X. Xu, Appl. Phys. Lett. **105**, 041109 (2014).
[301]M. Bayer, A. Kuther, A. Forchel, A. Gorbunov, V. B. Timofeev, F. Schäfer, J. P. Reithmaier, T. L. Reinecke, and S. N. Walck, Phys. Rev. Lett. **82**, 1748 (1999).
[302]M.-F. Tsai, H. Lin, C.-H. Lin, S.-D. Lin, S.-Y. Wang, M.-C. Lo, S.-J. Cheng, M.-C. Lee, and W.-H. Chang, Phys. Rev. Lett. **101**, 267402 (2008).
[303]S. Cao, J. Tang, Y. Sun, K. Peng, Y. Gao, Y. Zhao, C. Qian, S. Sun, H. Ali, Y. Shao, S. Wu, F. Song, D. A. Williams, W. Sheng, K. Jin, and X. Xu, Nano Res. **9**, 306 (2016).
[304]R. M. Stevenson, R. J. Young, P. Atkinson, K. Cooper, D. A. Ritchie, and A. J. Shields, Nature **439**, 179 (2006).
[305]X. Xu, Y. Wu, B. Sun, Q. Huang, J. Cheng, D. G. Steel, A. S. Bracker, D. Gammon, C. Emary, and L. J. Sham, Phys. Rev. Lett. **99**, 097401 (2007).
[306]J. Berezovsky, M. H. Mikkelsen, N. G. Stoltz, L. A. Coldren, and D. D. Awschalom, Science **320**, 349 (2008).

[307]A. Greilich, S. E. Economou, S. Spatzek, D. R. Yakovlev, D. Reuter, A. D. Wieck, T. L. Reinecke, and M. Bayer, Nat. Phys. **5**, 262 (2009).
[308]W. B. Gao, P. Fallahi, E. Togan, J. Miguel-Sanchez, and A. Imamoglu, Nature **491**, 426 (2012).
[309]K. De Greve, L. Yu, P. L. McMahon, J. S. Pelc, C. M. Natarajan, N. Y. Kim, E. Abe, S. Maier, C. Schneider, M. Kamp, S. Höfling, R. H. Hadfield, A. Forchel, M. M. Fejer, and Y. Yamamoto, Nature **491**, 421 (2012).
[310]J. R. Schaibley, A. P. Burgers, G. A. McCracken, L.-M. Duan, P. R. Berman, D. G. Steel, A. S. Bracker, D. Gammon, and L. J. Sham, Phys. Rev. Lett. **110**, 167401 (2013).
[311]Y. He, Y.-M. He, Y.-J. Wei, X. Jiang, K. Chen, C.-Y. Lu, J.-W. Pan, C. Schneider, M. Kamp, and S. Höfling, Phys. Rev. Lett. **119**, 060501 (2017).
[312]N. Coste, D. A. Fioretto, N. Belabas, S. C. Wein, P. Hilaire, R. Frantzeskakis, M. Gundin, B. Goes, N. Somaschi, M. Morassi, A. Lemaître, I. Sagnes, A. Harouri, S. E. Economou, A. Auffeves, O. Krebs, L. Lanco, and P. Senellart, Nat. Photonics **17**, 582 (2023).
[313]E. B. Flagg, A. Muller, S. V. Polyakov, A. Ling, A. Migdall, and G. S. Solomon, Phys. Rev. Lett. **104**, 137401 (2010).
[314]K. D. Jöns, R. Hafenbrak, R. Singh, F. Ding, J. D. Plumhof, A. Rastelli, O. G. Schmidt, G. Bester, and P. Michler, Phys. Rev. Lett. **107**, 217402 (2011).
[315]C. E. Kuklewicz, R. N. E. Malein, P. M. Petroff, and B. D. Gerardot, Nano Lett. **12**, 3761 (2012).
[316]F. Ding, R. Singh, J. D. Plumhof, T. Zander, V. Křápek, Y. H. Chen, M. Benyoucef, V. Zwiller, K. Dörr, G. Bester, A. Rastelli, and O. G. Schmidt, Phys. Rev. Lett. **104**, 067405 (2010).
[317]R. Trotta, E. Zallo, C. Ortix, P. Atkinson, J. D. Plumhof, J. van den Brink, A. Rastelli, and O. G. Schmidt, Phys. Rev. Lett. **109**, 147401 (2012).
[318]J. Zhang, F. Ding, E. Zallo, R. Trotta, B. Höfer, L. Han, S. Kumar, Y. Huo, A. Rastelli, and O. G. Schmidt, Nano Lett. **13**, 5808 (2013).
[319]J. Wang, M. Gong, G.-C. Guo, and L. He, Phys. Rev. Lett. **115**, 067401 (2015).
[320]R. Trotta, J. Martín-Sánchez, I. Daruka, C. Ortix, and A. Rastelli, Phys. Rev. Lett. **114**, 150502 (2015).
[321]D. Huber, M. Reindl, S. F. Covre da Silva, C. Schimpf, J. Martín-Sánchez, H. Huang, G. Piredda, J. Edlinger, A. Rastelli, and R. Trotta, Phys. Rev. Lett. **121**, 033902 (2018).
[322]T. Lettner, S. Gyger, K. D. Zeuner, L. Schweickert, S. Steinhauer, C. Reuterskiöld Hedlund, S. Stroj, A. Rastelli, M. Hammar, R. Trotta, K. D. Jöns, and V. Zwiller, Nano Lett. **21**, 10501 (2021).
[323]M. Metcalfe, S. M. Carr, A. Muller, G. S. Solomon, and J. Lawall, Phys. Rev. Lett. **105**, 037401 (2010).
[324]R. Zhu, J. Yang, X. Chen, W. Dai, H. Li, L. Yang, S. Yan, H. Liu, Z. Ma, Y. Yuan, B. Fu, Z. Zuo, H. Ni, Z. Niu, C. Wang, K. Jin, Q. Gong, and X. Xu, Phys. Rev. Appl. **24**, 054051 (2025).
[325]M. Weiß and H. J. Krenner, J. Phys. D Appl. Phys. **51**, 373001 (2018).
[326]M. Weiß, D. Wigger, M. Nägele, K. Müller, J. J. Finley, T. Kuhn, P. Machnikowski, and H. J. Krenner, Optica **8**, 291 (2021).
[327]D. D. Bühler, M. Weiß, A. Crespo-Poveda, E. D. S. Nysten, J. J. Finley, K. Müller, P. V. Santos, M. M. de Lima, and H. J. Krenner, Nat. Commun. **13**, 6998 (2022).
[328]R. A. DeCrescent, Z. Wang, P. Imany, R. C. Boutelle, C. A. McDonald, T. Autry, J. D. Teufel, S. W. Nam, R. P. Mirin, and K. L. Silverman, Phys. Rev. Appl. **18**, 034067 (2022).
[329]C. Santori, D. Fattal, J. Vučković, G. S. Solomon, and Y. Yamamoto, Nature **419**, 594–597 (2002).
[330]D. Loss and D. P. DiVincenzo, Phys. Rev. A **57**, 120 (1998).
[331]T. Gerster, A. Müller, L. Freise, D. Reifert, D. Maradan, P. Hinze, T. Weimann, H. Marx, K. Pierz, and H. W. Schumacher, Metrologia **56**, 014002 (2019).
[332]X.-L. Wang, L.-K. Chen, W. Li, H.-L. Huang, C. Liu, C. Chen, Y.-H. Luo, Z.-E. Su, D. Wu, Z.-D. Li, H. Lu, Y. Hu, X. Jiang, C.-Z. Peng, L. Li, N.-L. Liu, Y.-A. Chen, C.-Y. Lu, and J.-W. Pan, Phys. Rev. Lett. **117**, 210502 (2016).
[333]R. H. Brown and R. Q. Twiss, Nature **177**, 27–29 (1956).
[334]R. Uppu, F. T. Pedersen, Y. Wang, C. T. Olesen, C. Papon, X. Zhou, L. Midolo, S. Scholz, A. D. Wieck, A. Ludwig, and P. Lodahl, Sci. Adv. **6**, eabc8268 (2020).
[335]C. K. Hong, Z. Y. Ou, and L. Mandel, Phys. Rev. Lett. **59**, 2044 (1987).
[336]N. Tomm, A. Javadi, N. O. Antoniadis, D. Najer, M. C. Löbl, A. R. Korsch, R. Schott, S. R. Valentin, A. D. Wieck, A. Ludwig, and R. J. Warburton, Nat. Nanotechnol. **16**, 399 (2021).
[337]X. Ding, Y.-P. Guo, M.-C. Xu, R.-Z. Liu, G.-Y. Zou, J.-Y. Zhao, Z.-X. Ge, Q.-H. Zhang, H.-L. Liu, L.-J. Wang, M.-C. Chen, H. Wang, Y.-M. He, Y.-H. Huo, C.-Y. Lu, and J.-W. Pan, Nat. Photonics **19**, 387 (2025).
[338]D. J. Brod, E. F. Galvão, A. Crespi, R. Osellame, N. Spagnolo, and F. Sciarrino, Adv. Photonics **1**, 034001 (2019).
[339]M. Varnava, D. E. Browne, and T. Rudolph, Phys. Rev. Lett. **100**, 060502 (2008).
[340]Y. Li, P. C. Humphreys, G. J. Mendoza, and S. C. Benjamin, Phys. Rev. X **5**, 041007 (2015).
[341]M. Müller, S. Bounouar, K. D. Jöns, M. Glässl, and P. Michler, Nat. Photonics **8**, 224 (2014).
[342]Y. Chen, J. Zhang, M. Zopf, K. Jung, Y. Zhang, R. Keil, F. Ding, and O. G. Schmidt, Nat. Commun. **7**, 10387 (2016).
[343]S. Liu, Y. Wang, Y. Saleem, X. Li, H. Liu, C.-A. Yang, J. Yang, H. Ni, Z. Niu, Y. Meng, X. Hu, Y. Yu, X. Wang, M. Cygorek, and J. Liu, Nature **643**, 1234 (2025).
[344]H. Wang, Y.-M. He, T.-H. Chung, H. Hu, Y. Yu, S. Chen, X. Ding, M.-C. Chen, J. Qin, X. Yang, R.-Z. Liu, Z.-C. Duan, J.-P. Li, S. Gerhardt, K. Winkler, J. Jurkat, L.-J. Wang, N. Gregersen, Y.-H. Huo, Q. Dai, S. Yu, S. Höfling, C.-Y. Lu, and J.-W. Pan, Nat. Photonics **13**, 770 (2019).
[345]Y. Wei, S. Liu, X. Li, Y. Yu, X. Su, S. Li, X. Shang, H. Liu, H. Hao, H. Ni, S. Yu, Z. Niu, J. Iles-Smith, J. Liu, and X. Wang, Nat. Nanotechnol. **17**, 470 (2022).
[346]J. Yan, S. Liu, X. Lin, Y. Ye, J. Yu, L. Wang, Y. Yu, Y. Zhao, Y. Meng, X. Hu, D.-W. Wang, C. Jin, and F. Liu, Nano Lett. **22**, 1483 (2022).
[347]F. Sbresny, L. Hanschke, E. Schöll, W. Rauhaus, B. Scaparra, K. Boos, E. Zubizarreta Casalengua, H. Riedl, E. del Valle, J. J. Finley, K. D. Jöns, and K. Müller, Phys. Rev. Lett. **128**, 093603 (2022).
[348]O. Benson, C. Santori, M. Pelton, and Y. Yamamoto, Phys. Rev. Lett. **84**, 2513 (2000).
[349]N. Akopian, N. H. Lindner, E. Poem, Y. Berlatzky, J. Avron, D. Gershoni, B. D. Gerardot, and P. M. Petroff, Phys. Rev. Lett. **96**, 130501 (2006).
[350]L. Hanschke, K. A. Fischer, S. Appel, D. Lukin, J. Wierzbowski, S. Sun, R. Trivedi, J. Vučković, J. J. Finley, and K. Müller, npj Quantum Inf. **4**, 43 (2018).
[351]M. Gong, W. Zhang, G.-C. Guo, and L. He, Phys. Rev. Lett. **106**, 227401 (2011).
[352]R. Trotta, J. Martín-Sánchez, J. S. Wildmann, G. Piredda, M. Reindl, C. Schimpf, E. Zallo, S. Stroj, J. Edlinger, and A. Rastelli, Nat. Commun. **7**, 10375 (2016).
[353]D. Huber, M. Reindl, Y. Huo, H. Huang, J. S. Wildmann, O. G. Schmidt, A. Rastelli, and R. Trotta, Nat. Commun. **8**, 15506 (2017).
[354]M. Zopf, R. Keil, Y. Chen, J. Yang, D. Chen, F. Ding, and O. G. Schmidt, Phys. Rev. Lett. **123**, 160502 (2019).
[355]F. Basso Basset, M. B. Rota, C. Schimpf, D. Tedeschi, K. D. Zeuner, S. F. Covre da Silva, M. Reindl, V. Zwiller, K. D. Jöns, A. Rastelli, and R. Trotta, Phys. Rev. Lett. **123**, 160501 (2019).
[356]F. B. Basset, M. Valeri, E. Roccia, V. Muredda, D. Poderini, J. Neuwirth, N. Spagnolo, M. B. Rota, G. Carvacho, F. Sciarrino, and R. Trotta, Sci. Adv. **7**, eabe6379 (2021).
[357]D. Press, T. D. Ladd, B. Zhang, and Y. Yamamoto, Nature **456**, 218 (2008).
[358]M. H. Appel, A. Ghorbal, N. Shofer, L. Zaporski, S. Manna, S. F. C. da Silva, U. Haeusler, C. L. Gall, A. Rastelli, D. A. Gangloff, and M. Atatüre, Nat. Phys. **21**, 368–373 (2025).
[359]P. Laccotripes, T. Müller, R. M. Stevenson, J. Skiba-Szymanska, D. A. Ritchie, and A. J. Shields, Nat. Commun. **15**, 9740 (2024).
[360]I. Schwartz, D. Cogan, E. R. Schmidgall, Y. Don, L. Gantz, O. Kenneth, N. H. Lindner, and D. Gershoni, Science **354**, 434 (2016).
[361]D. Cogan, Z.-E. Su, O. Kenneth, and D. Gershoni, Nat. Photonics **17**, 324 (2023).
[362]K. Tiurev, M. H. Appel, P. L. Mirambell, M. B. Lauritzen, A. Tiranov, P. Lodahl, and A. S. Sørensen, Phys. Rev. A **105**, L030601 (2022).
[363]M. N. Makhonin, K. V. Kavokin, P. Senellart, A. Lemaître, A. J. Ramsay, M. S. Skolnick, and A. I. Tartakovskii, Nat. Mater. **10**, 844–848 (2011).
[364]D. M. Jackson, U. Haeusler, L. Zaporski, J. H. Bodey, N. Shofer, E. Clarke, M. Hugues, M. Atatüre, C. Le Gall, and D. A. Gangloff, Phys. Rev. X **12**, 031014 (2022).

[365]G. Éthier-Majcher, D. Gangloff, R. Stockill, E. Clarke, M. Hugues, C. Le Gall, and M. Atatüre, Phys. Rev. Lett. **119**, 130503 (2017).
[366]L. Zaporski, N. Shofer, J. H. Bodey, S. Manna, G. Gillard, M. H. Appel, C. Schimpf, S. F. Covre da Silva, J. Jarman, G. Delamare, G. Park, U. Haeusler, E. A. Chekhovich, A. Rastelli, D. A. Gangloff, M. Atatüre, and C. Le Gall, Nat. Nanotechnol. **18**, 257 (2023).
[367]J. H. Prechtel, A. V. Kuhlmann, J. Houel, A. Ludwig, S. R. Valentin, A. D. Wieck, and R. J. Warburton, Nat. Mater. **15**, 981–986 (2016).
[368]D. A. Gangloff, G. Éthier Majcher, C. Lang, E. V. Denning, J. H. Bodey, D. M. Jackson, E. Clarke, M. Hugues, and M. Atatüre, Science **364**, 62 (2019).
[369]D. M. Jackson, D. A. Gangloff, J. H. Bodey, L. Zaporski, C. Bachorz, E. Clarke, M. Hugues, C. Le Gall, and M. Atatüre, Nat. Phys. **17**, 585 (2021).
[370]E. A. Chekhovich, S. F. C. da Silva, and A. Rastelli, Nat. Nanotechnol. **15**, 999 (2020).
[371]J. Gérard, B. Sermage, B. Gayral, B. Legrand, E. Costard, and V. Thierry-Mieg, Phys. Rev. Lett. **81**, 1110 (1998).
[372]J. P. Reithmaier, G. Sek, A. Löffler, C. Hofmann, S. Kuhn, S. Reitzenstein, L. V. Keldysh, V. D. Kulakovskii, T. L. Reinecke, and A. Forchel, Nature **432**, 197 (2004).
[373]L. Novotny, Am. J. Phys. **78**, 1199 (2010).
[374]S. R.-K. Rodriguez, Eur. J. Phys. **37**, 025802 (2016).
[375]J.-M. Gerard and B. Gayral, J. Lightwave Technol. **17**, 2089 (1999).
[376]Anonymous. Phys. Rev. **69**, 674 (1946).
[377]T. Yoshie, A. Scherer, J. Hendrickson, G. Khitrova, H. M. Gibbs, G. Rupper, C. Ell, O. B. Shchekin, and D. G. Deppe, Nature **432**, 200 (2004).
[378]F. S. F. Brossard, X. L. Xu, D. A. Williams, M. Hadjipanayi, M. Hugues, M. Hopkinson, X. Wang, and R. A. Taylor, Appl. Phys. Lett. **97**, 111101 (2010).
[379]C. Schneider, P. Gold, S. Reitzenstein, S. Höfling, and M. Kamp, Appl. Phys. B **122**, 19 (2016).
[380]Y. Ota, D. Takamiya, R. Ohta, H. Takagi, N. Kumagai, S. Iwamoto, and Y. Arakawa, Appl. Phys. Lett. **112**, 093101 (2018).
[381]S. Yan, H. Li, J. Yang, X. Chen, H. Liu, D. Dai, R. Zhu, Z. Ma, S. Shi, L. Yang, Y. Yuan, W. Dai, D. Dai, B. Fu, Z. Zuo, H. Ni, Z. Niu, C. Wang, K. Jin, Q. Gong, and X. Xu, Nat. Commun. **16**, 4634 (2025).
[382]X. Xie, W. Zhang, X. He, S. Wu, J. Dang, K. Peng, F. Song, L. Yang, H. Ni, Z. Niu, C. Wang, K. Jin, X. Zhang, and X. Xu, Laser Photonics Rev. **14**, 1900425 (2020).
[383]P. Holewa, D. A. Vajner, E. Zieba-Ostój, M. Wasiluk, B. Gaál, A. Sakanas, M. G. Mikulicz, P. Mrowiński, B. Krajnik, M. Xiong, K. Yvind, N. Gregersen, A. Musiał, A. Huck, T. Heindel, M. Syperek, and E. Semenova, Nat. Commun. **15**, 3358 (2024).
[384]J. Yang, S. Shi, S. Yan, R. Zhu, X. Zhao, Y. Qin, B. Fu, X. Chen, H. Li, Z. Zuo, K. Jin, Q. Gong, and X. Xu, Commun. Phys. **7**, 13 (2024).
[385]R. Zhu, C. Qian, S. Xiao, J. Yang, S. Yan, H. Liu, D. Dai, H. Li, L. Yang, X. Chen, Y. Yuan, D. Dai, Z. Zuo, H. Ni, Z. Niu, C. Wang, K. Jin, Q. Gong, and X. Xu, Light Sci. Appl. **14**, 114 (2025).
[386]J. M. Gérard, D. Barrier, J. Y. Marzin, R. Kuszelewicz, L. Manin, E. Costard, V. Thierry-Mieg, and T. Rivera, Appl. Phys. Lett. **69**, 449 (1996).
[387]S. Liu, X. Li, H. Liu, G. Qiu, J. Ma, L. Nie, Y. Meng, X. Hu, H. Ni, Z. Niu, C.-W. Qiu, X. Wang, and J. Liu, Nat. Photonics **18**, 967 (2024).
[388]Y. Akahane, T. Asano, B.-S. Song, and S. Noda, Nature **425**, 944 (2003).
[389]O. Painter, R. K. Lee, A. Scherer, A. Yariv, J. D. O'Brien, P. D. Dapkus, and I. Kim, Science **284**, 1819 (1999).
[390]M. Minkov, V. Savona, and D. Gerace, Appl. Phys. Lett. **111**, 131104 (2017).
[391]M. Minkov and V. Savona, Sci. Rep. **4**, 5124 (2014).
[392]Y.-H. Ouyang, H.-Y. Luan, Z.-W. Zhao, W.-Z. Mao, and R.-M. Ma, Nature **632**, 287 (2024).
[393]Y.-T. Wang, Q.-H. Ye, J.-Y. Yan, Y. Qiao, Y.-X. Liu, Y.-Z. Ye, C. Chen, X.-T. Cheng, C.-H. Li, Z.-J. Zhang, C.-N. Huang, Y. Meng, K. Zou, W.-K. Zhan, C. Zhao, X. Hu, C. A. T. H. Tee, W. E. I. Sha, Z. Huang, H. Liu, C.-Y. Jin, L. Ying, and F. Liu, Sci. Adv. **11**, eadv8115 (2025).
[394]Y. Ota, F. Liu, R. Katsumi, K. Watanabe, K. Wakabayashi, Y. Arakawa, and S. Iwamoto, Optica **6**, 786 (2019).
[395]C. F. Fong, Y. Ota, Y. Arakawa, S. Iwamoto, and Y. K. Kato, Phys. Rev. Res. **3**, 043096 (2021).
[396]A. R. A. Chalcraft, S. Lam, B. D. Jones, D. Szymanski, R. Oulton, A. C. T. Thijssen, M. S. Skolnick, D. M. Whittaker, T. F. Krauss, and A. M. Fox, Opt. Express **19**, 5670 (2011).
[397]H. Choi, M. Heuck, and D. Englund, Phys. Rev. Lett. **118**, 223605 (2017).
[398]M. Albrechtsen, B. Vosoughi Lahijani, R. E. Christiansen, V. T. H. Nguyen, L. N. Casses, S. E. Hansen, N. Stenger, O. Sigmund, H. Jansen, J. Mørk, and S. Stobbe, Nat. Commun. **13**, 6281 (2022).
[399]A. N. Babar, T. A. S. Weis, K. Tsoukalas, S. Kadkhodazadeh, G. Arregui, B. Vosoughi Lahijani, and S. Stobbe, Nature **624**, 57 (2023).
[400]N. Granchi, F. Intonti, M. Florescu, P. D. García, M. Gurioli, and G. Arregui, ACS Photonics **10**, 2808 (2023).
[401]J. Sweet, B. Richards, J. Olitzky, J. Hendrickson, G. Khitrova, H. Gibbs, D. Litvinov, D. Gerthsen, D. Hu, D. Schaadt, M. Wegener, U. Khankhoje, and A. Scherer, Photonic. Nanostruct. **8**, 1 (2010).
[402]K. Kuruma, Y. Ota, M. Kakuda, S. Iwamoto, and Y. Arakawa, APL Photonics **5**, 046106 (2020).
[403]L. Sapienza, M. Davanço, A. Badolato, and K. Srinivasan, Nat. Commun. **6**, 7833 (2015).
[404]A. Dousse, L. Lanco, J. Suffczyński, E. Semenova, A. Miard, A. Lemaître, I. Sagnes, C. Roblin, J. Bloch, and P. Senellart, Phys. Rev. Lett. **101**, 267404 (2008).
[405]M. Gschrey, A. Thoma, P. Schnauber, M. Seifried, R. Schmidt, B. Wohlfeil, L. Krüger, J. H. Schulze, T. Heindel, S. Burger, F. Schmidt, A. Strittmatter, S. Rodt, and S. Reitzenstein, Nat. Commun. **6**, 7662 (2015).
[406]P. Schnauber, J. Schall, S. Bounouar, T. Höhne, S.-I. Park, G.-H. Ryu, T. Heindel, S. Burger, J.-D. Song, S. Rodt, and S. Reitzenstein, Nano Lett. **18**, 2336 (2018).
[407]R. Uppu, H. T. Eriksen, H. Thyrrestrup, A. D. Uğurlu, Y. Wang, S. Scholz, A. D. Wieck, A. Ludwig, M. C. Löbl, R. J. Warburton, P. Lodahl, and L. Midolo, Nat. Commun. **11**, 3782 (2020).
[408]M. B. Rota, T. M. Krieger, Q. Buchinger, M. Beccaceci, J. Neuwirth, H. Huet, N. Horová, G. Lovicu, G. Ronco, S. F. Covre Da Silva, G. Pettinari, M. Moczala-Dusanowska, C. Kohlberger, S. Manna, S. Stroj, J. Freund, X. Yuan, C. Schneider, M. Ježek, S. Höfling, F. Basso Basset, T. Huber-Loyola, A. Rastelli, and R. Trotta, eLight **4**, 13 (2024).
[409]T. Huber, M. Davanco, M. Müller, Y. Shuai, O. Gazzano, and G. S. Solomon, Optica **7**, 380 (2020).
[410]A. Javadi, N. Tomm, N. O. Antoniadis, A. J. Brash, R. Schott, S. R. Valentin, A. D. Wieck, A. Ludwig, and R. J. Warburton, New J. Phys. **25**, 093027 (2023).
[411]G. Kiršanskė, H. Thyrrestrup, R. S. Daveau, C. L. Dreeßen, T. Pregnolato, L. Midolo, P. Tighineanu, A. Javadi, S. Stobbe, R. Schott, A. Ludwig, A. D. Wieck, S. I. Park, J. D. Song, A. V. Kuhlmann, I. Söllner, M. C. Löbl, R. J. Warburton, and P. Lodahl, Phys. Rev. B **96**, 165306 (2017).
[412]R. S. Daveau, K. C. Balram, T. Pregnolato, J. Liu, E. H. Lee, J. D. Song, V. Verma, R. Mirin, S. W. Nam, L. Midolo, S. Stobbe, K. Srinivasan, and P. Lodahl, Optica **4**, 178 (2017).
[413]C.-M. Lee, M. A. Buyukkaya, S. Harper, S. Aghaeimeibodi, C. J. K. Richardson, and E. Waks, Nano Lett. **21**, 323 (2021).
[414]L. Schweickert, K. D. Jöns, K. D. Zeuner, S. F. Covre da Silva, H. Huang, T. Lettner, M. Reindl, J. Zichi, R. Trotta, A. Rastelli, and V. Zwiller, Appl. Phys. Lett. **112**, 093106 (2018).
[415]Z. X. Koong, E. Scerri, M. Rambach, M. Cygorek, M. Brotons-Gisbert, R. Picard, Y. Ma, S. I. Park, J. D. Song, E. M. Gauger, and B. D. Gerardot, Phys. Rev. Lett. **126**, 047403 (2021).
[416]J. Yang, Y. Chen, Z. Rao, Z. Zheng, C. Song, Y. Chen, K. Xiong, P. Chen, C. Zhang, W. Wu, Y. Yu, and S. Yu, Light Sci. Appl. **13**, 33 (2024).
[417]J. Kaupp, Y. Reum, F. Kohr, J. Michl, Q. Buchinger, A. Wolf, G. Peniakov, T. Huber-Loyola, A. Pfenning, and S. Höfling, Adv. Quantum Technol. **6**, 2300242 (2023).
[418]S. E. Thomas, M. Billard, N. Coste, S. C. Wein, Priya, H. Ollivier, O. Krebs, L. Tazaïrt, A. Harouri, A. Lemaitre, I. Sagnes, C. Anton, L. Lanco, N. Somaschi, J. C. Loredo, and P. Senellart, Phys. Rev. Lett. **126**, 233601 (2021).
[419]B. Chen, Y. Wei, T. Zhao, S. Liu, R. Su, B. Yao, Y. Yu, J. Liu, and X. Wang, Nat. Nanotechnol. **16**, 302 (2021).
[420]S. Kolatschek, C. Nawrath, S. Bauer, J. Huang, J. Fischer, R. Sittig, M. Jetter, S. L. Portalupi, and P. Michler, Nano Lett. **21**, 7740 (2021).
[421]X. Ding, Y. He, Z.-C. Duan, N. Gregersen, M.-C. Chen, S. Unsleber, S. Maier, C. Schneider, M. Kamp, S. Höfling, C.-Y. Lu, and J.-W. Pan, Phys. Rev. Lett. **116**, 020401 (2016).
[422]N. Srocka, P. Mrowiński, J. Große, M. Von Helversen, T. Heindel, S. Rodt, and S. Reitzenstein, Appl. Phys. Lett. **116**, 231104 (2020).

[423]J.-H. Kim, T. Cai, C. J. K. Richardson, R. P. Leavitt, and E. Waks, Optica **3**, 577 (2016).
[424]T. Mano, M. Abbarchi, T. Kuroda, C. A. Mastrandrea, A. Vinattieri, S. Sanguinetti, K. Sakoda, and M. Gurioli, Nanotechnology **20**, 395601 (2009).
[425]Y. Ota, S. Iwamoto, N. Kumagai, and Y. Arakawa, Phys. Rev. Lett. **107**, 233602 (2011).
[426]A. Dousse, J. Suffczyński, A. Beveratos, O. Krebs, A. Lemaître, I. Sagnes, J. Bloch, P. Voisin, and P. Senellart, Nature **466**, 217 (2010).
[427]L. Ginés, M. Moczała-Dusanowska, D. Dlaka, R. Hošák, J. R. Gonzales-Ureta, J. Lee, M. Ježek, E. Harbord, R. Oulton, S. Höfling, A. B. Young, C. Schneider, and A. Predojević, Phys. Rev. Lett. **129**, 033601 (2022).
[428]H. Wang, H. Hu, T.-H. Chung, J. Qin, X. Yang, J.-P. Li, R.-Z. Liu, H.-S. Zhong, Y.-M. He, X. Ding, Y.-H. Deng, Q. Dai, Y.-H. Huo, S. Höfling, C.-Y. Lu, and J.-W. Pan, Phys. Rev. Lett. **122**, 113602 (2019).
[429]F. Basso Basset, M. Rota, M. Beccaceci, T. Krieger, Q. Buchinger, J. Neuwirth, H. Huet, S. Stroj, S. Covre Da Silva, G. Ronco, C. Schimpf, S. Höfling, T. Huber-Loyola, A. Rastelli, and R. Trotta, Phys. Rev. Lett. **131**, 166901 (2023).
[430]S. G. Carter, T. M. Sweeney, M. Kim, C. S. Kim, D. Solenov, S. E. Economou, T. L. Reinecke, L. Yang, A. S. Bracker, and D. Gammon, Nat. Photonics **7**, 329 (2013).
[431]N. O. Antoniadis, M. R. Hogg, W. F. Stehl, A. Javadi, N. Tomm, R. Schott, S. R. Valentin, A. D. Wieck, A. Ludwig, and R. J. Warburton, Nat. Commun. **14**, 3977 (2023).
[432]E. Mehdi, M. Gundín, C. Millet, N. Somaschi, A. Lemaître, I. Sagnes, L. Le Gratiet, D. A. Fioretto, N. Belabas, O. Krebs, P. Senellart, and L. Lanco, Nat. Commun. **15**, 598 (2024).
[433]J. Ma, J. Yang, S. Liu, B. Chen, X. Li, C. Song, G. Qiu, K. Zou, X. Hu, F. Li, Y. Yu, and J. Liu, Nat. Phys. **21**, 1462 (2025).
[434]K. Hennessy, A. Badolato, M. Winger, D. Gerace, M. Atatüre, S. Gulde, S. Fält, E. L. Hu, and A. Imamoğlu, Nature **445**, 896 (2007).
[435]C. Qian, X. Xie, J. Yang, K. Peng, S. Wu, F. Song, S. Sun, J. Dang, Y. Yu, M. J. Steer, I. G. Thayne, K. Jin, C. Gu, and X. Xu, Phys. Rev. Lett. **122**, 087401 (2019).
[436]H. Kim, R. Bose, T. C. Shen, G. S. Solomon, and E. Waks, Nat. Photonics **7**, 373 (2013).
[437]S. Sun, H. Kim, Z. Luo, G. S. Solomon, and E. Waks, Science **361**, 57 (2018).
[438]Z. Luo, S. Sun, A. Karasahin, A. S. Bracker, S. G. Carter, M. K. Yakes, D. Gammon, and E. Waks, Nano Lett. **19**, 7072 (2019).
[439]K. Srinivasan and O. Painter, Nature **450**, 862 (2007).
[440]J. Kasprzak, S. Reitzenstein, E. A. Muljarov, C. Kistner, C. Schneider, M. Strauss, S. Höfling, A. Forchel, and W. Langbein, Nat. Mater. **9**, 304 (2010).
[441]D. Najer, I. Söllner, P. Sekatski, V. Dolique, M. C. Löbl, D. Riedel, R. Schott, S. Starosielec, S. R. Valentin, A. D. Wieck, N. Sangouard, A. Ludwig, and R. J. Warburton, Nature **575**, 622 (2019).
[442]M. Nomura, N. Kumagai, S. Iwamoto, Y. Ota, and Y. Arakawa, Nat. Phys. **6**, 279 (2010).
[443]R. Ohta, Y. Ota, M. Nomura, N. Kumagai, S. Ishida, S. Iwamoto, and Y. Arakawa, Appl. Phys. Lett. **98**, 173104 (2011).
[444]K. Müller, K. A. Fischer, A. Rundquist, C. Dory, K. G. Lagoudakis, T. Sarmiento, Y. A. Kelaita, V. Borish, and J. Vučković, Phys. Rev. X **5**, 031006 (2015).
[445]K. Kuruma, Y. Ota, M. Kakuda, S. Iwamoto, and Y. Arakawa, Phys. Rev. B **97**, 235448 (2018).
[446]S. Reitzenstein, S. Münch, P. Franeck, A. Rahimi-Iman, A. Löffler, S. Höfling, L. Worschech, and A. Forchel, Phys. Rev. Lett. **103**, 127401 (2009).
[447]A. Faraon, A. Majumdar, H. Kim, P. Petroff, and J. Vučković, Phys. Rev. Lett. **104**, 047402 (2010).
[448]O. Stier, M. Grundmann, and D. Bimberg, Phys. Rev. B **59**, 5688 (1999).
[449]S. Stobbe, P. T. Kristensen, J. E. Mortensen, J. M. Hvam, J. Mørk, and P. Lodahl, Phys. Rev. B **86**, 085304 (2012).
[450]C. Arnold, J. Demory, V. Loo, A. Lemaître, I. Sagnes, M. Glazov, O. Krebs, P. Voisin, P. Senellart, and L. Lanco, Nat. Commun. **6**, 6236 (2015).
[451]J. Miguel-Sánchez, A. Reinhard, E. Togan, T. Volz, A. Imamoglu, B. Besga, J. Reichel, and J. Estève, New J. Phys. **15**, 045002 (2013).
[452]S. Sun, H. Kim, G. S. Solomon, and E. Waks, Nat. Nanotechnol. **11**, 539 (2016).
[453]A. Faraon, I. Fushman, D. Englund, N. Stoltz, P. Petroff, and J. Vučković, Nat. Phys. **4**, 859 (2008).
[454]A. Reinhard, T. Volz, M. Winger, A. Badolato, K. J. Hennessy, E. L. Hu, and A. Imamoğlu, Nat. Photonics **6**, 93 (2012).
[455]K. Müller, A. Rundquist, K. A. Fischer, T. Sarmiento, K. G. Lagoudakis, Y. A. Kelaita, C. Sánchez Muñoz, E. del Valle, F. P. Laussy, and J. Vučković, Phys. Rev. Lett. **114**, 233601 (2015).
[456]T. Volz, A. Reinhard, M. Winger, A. Badolato, K. J. Hennessy, E. L. Hu, and A. Imamoğlu, Nat. Photonics **6**, 605 (2012).
[457]J. Wang, F. Sciarrino, A. Laing, and M. G. Thompson, Nat. Photonics **14**, 273 (2020).
[458]S. Hepp, M. Jetter, S. L. Portalupi, and P. Michler, Adv. Quantum Technol. **2**, 1900020 (2019).
[459]W. Luo, L. Cao, Y. Shi, L. Wan, H. Zhang, S. Li, G. Chen, Y. Li, S. Li, Y. Wang, S. Sun, M. F. Karim, H. Cai, L. C. Kwek, and A. Q. Liu, Light Sci. Appl. **12**, 175 (2023).
[460]R. J. Coles, D. M. Price, J. E. Dixon, B. Royall, E. Clarke, P. Kok, M. S. Skolnick, A. M. Fox, and M. N. Makhonin, Nat. Commun. **7**, 11183 (2016).
[461]S. Xiao, S. Wu, X. Xie, J. Yang, W. Wei, S. Shi, F. Song, J. Dang, S. Sun, L. Yang, Y. Wang, S. Yan, Z. Zuo, T. Wang, J. Zhang, K. Jin, and X. Xu, Laser Photonics Rev. **15**, 2100009 (2021).
[462]B. Lang, D. P. S. McCutcheon, E. Harbord, A. B. Young, and R. Oulton, Phys. Rev. Lett. **128**, 073602 (2022).
[463]M. Jalali Mehrabad, A. P. Foster, R. Dost, E. Clarke, P. K. Patil, A. M. Fox, M. S. Skolnick, and L. R. Wilson, Optica **7**, 1690 (2020).
[464]R. Faggiani, J. Yang, R. Hostein, and P. Lalanne, Optica **4**, 393 (2017).
[465]H. Siampour, C. O'Rourke, A. J. Brash, M. N. Makhonin, R. Dost, D. J. Hallett, E. Clarke, P. K. Patil, M. S. Skolnick, and A. M. Fox, npj Quantum Inf. **9**, 15 (2023).
[466]R. Uppu, L. Midolo, X. Zhou, J. Carolan, and P. Lodahl, Nat. Nanotechnol. **16**, 1308 (2021).
[467]M. Arcari, I. Söllner, A. Javadi, S. Lindskov Hansen, S. Mahmoodian, J. Liu, H. Thyrrestrup, E. H. Lee, J. D. Song, S. Stobbe, and P. Lodahl, Phys. Rev. Lett. **113**, 093603 (2014).
[468]L. Scarpelli, B. Lang, F. Masia, D. M. Beggs, E. A. Muljarov, A. B. Young, R. Oulton, M. Kamp, S. Höfling, C. Schneider, and W. Langbein, Phys. Rev. B **100**, 035311 (2019).
[469]S. Mahmoodian, P. Lodahl, and A. S. Sørensen, Phys. Rev. Lett. **117**, 240501 (2016).
[470]F. T. Østfeldt, E. M. González-Ruiz, N. Hauff, Y. Wang, A. D. Wieck, A. Ludwig, R. Schott, L. Midolo, A. S. Sørensen, R. Uppu, and P. Lodahl, PRX Quantum **3**, 020363 (2022).
[471]I. J. Luxmoore, N. A. Wasley, A. J. Ramsay, A. C. T. Thijssen, R. Oulton, M. Hugues, A. M. Fox, and M. S. Skolnick, Appl. Phys. Lett. **103**, 241102 (2013).
[472]I. Söllner, S. Mahmoodian, S. L. Hansen, L. Midolo, A. Javadi, G. Kiršanskė, T. Pregnolato, H. El-Ella, E. H. Lee, J. D. Song, S. Stobbe, and P. Lodahl, Nat. Nanotechnol. **10**, 775 (2015).
[473]P. Mrowiński, P. Schnauber, P. Gutsche, A. Kaganskiy, J. Schall, S. Burger, S. Rodt, and S. Reitzenstein, ACS Photonics **6**, 2231 (2019).
[474]S. Xiao, S. Wu, X. Xie, J. Yang, W. Wei, S. Shi, F. Song, S. Sun, J. Dang, L. Yang, Y. Wang, Z. Zuo, T. Wang, J. Zhang, and X. Xu, Appl. Phys. Lett. **118**, 091106 (2021).
[475]S. Barik, A. Karasahin, C. Flower, T. Cai, H. Miyake, W. DeGottardi, M. Hafezi, and E. Waks, Science **359**, 666 (2018).
[476]S. Barik, A. Karasahin, S. Mittal, E. Waks, and M. Hafezi, Phys. Rev. B **101**, 205303 (2020).
[477]X. Xie, S. Yan, J. Dang, J. Yang, S. Xiao, Y. Wang, S. Shi, L. Yang, D. Dai, Y. Yuan, N. Luo, T. Cui, G. Chi, Z. Zuo, B.-B. Li, C. Wang, and X. Xu, Phys. Rev. Appl. **16**, 014036 (2021).
[478]K. Kuruma, H. Yoshimi, Y. Ota, R. Katsumi, M. Kakuda, Y. Arakawa, and S. Iwamoto, Laser Photonics Rev. **16**, 2200077 (2022).
[479]N. J. Martin, M. Jalali Mehrabad, X. Chen, R. Dost, E. Nussbaum, D. Hallett, L. Hallacy, A. Foster, E. Clarke, P. K. Patil, S. Hughes, M. Hafezi, A. M. Fox, M. S. Skolnick, and L. R. Wilson, Phys. Rev. Res. **6**, L022065 (2024).
[480]E. Viasnoff-Schwoob, C. Weisbuch, H. Benisty, S. Olivier, S. Varoutsis, I. Robert-Philip, R. Houdré, and C. J. M. Smith, Phys. Rev. Lett. **95**, 183901 (2005).
[481]V. S. C. Manga Rao and S. Hughes, Phys. Rev. B **75**, 205437 (2007).
[482]A. Javadi, I. Söllner, M. Arcari, S. L. Hansen, L. Midolo, S. Mahmoodian, G. Kiršanskė, T. Pregnolato, E. H. Lee, J. D. Song, S. Stobbe, and P. Lodahl, Nat. Commun. **6**, 8655 (2015).

[483]L. Hallacy, N. J. Martin, M. J. Mehrabad, D. Hallett, X. Chen, R. Dost, A. Foster, L. Brunswick, A. Fenzl, E. Clarke, P. K. Patil, A. M. Fox, M. S. Skolnick, and L. R. Wilson, npj Nanophotonics **2**(1), 9 (2025).
[484]A. Kala, D. Sharp, M. Choi, A. Manna, P. Deshmukh, V. Kizhake Veetil, V. Menon, M. Pelton, E. Waks, and A. Majumdar, ACS Nano **19**, 14557 (2025).
[485]L. Dusanowski, D. Köck, E. Shin, S.-H. Kwon, C. Schneider, and S. Höfling, Nano Lett. **20**, 6357 (2020).
[486]S. Li, Y. Yang, J. Schall, M. Von Helversen, C. Palekar, H. Liu, L. Roche, S. Rodt, H. Ni, Y. Zhang, Z. Niu, and S. Reitzenstein, ACS Photonics **10**, 2846 (2023).
[487]L. Dusanowski, D. Köck, C. Schneider, and S. Höfling, ACS Photonics **10**, 2941 (2023).
[488]M. Davanco, J. Liu, L. Sapienza, C.-Z. Zhang, J. V. De Miranda Cardoso, V. Verma, R. Mirin, S. W. Nam, L. Liu, and K. Srinivasan, Nat. Commun. **8**, 889 (2017).
[489]R. Katsumi, Y. Ota, M. Kakuda, S. Iwamoto, and Y. Arakawa, Optica **5**, 691 (2018).
[490]M. Schwartz, E. Schmidt, U. Rengstl, F. Hornung, S. Hepp, S. L. Portalupi, K. Llin, M. Jetter, M. Siegel, and P. Michler, Nano Lett. **18**, 6892 (2018).
[491]C. P. Dietrich, A. Fiore, M. G. Thompson, M. Kamp, and S. Höfling, Laser Photonics Rev. **10**, 870 (2016).
[492]F. Hornung, U. Pfister, S. Bauer, D. R. Cyrlyson's, D. Wang, P. Vijayan, A. J. Garcia, S. F. Covre Da Silva, M. Jetter, S. L. Portalupi, A. Rastelli, and P. Michler, Nano Lett. **24**, 1184 (2024).
[493]A. Peruzzo, A. Laing, A. Politi, T. Rudolph, and J. L. O'Brien, Nat. Commun. **2**, 224 (2011).
[494]G. F. R. Chen, J. R. Ong, T. Y. L. Ang, S. T. Lim, C. E. Png, and D. T. H. Tan, Sci. Rep. **7**, 7246 (2017).
[495]H. Yamada, T. Chu, S. Ishida, and Y. Arakawa, IEEE Photonics Technol. Lett. **17**, 585 (2005).
[496]N. Prtljaga, R. J. Coles, J. O'Hara, B. Royall, E. Clarke, A. M. Fox, and M. S. Skolnick, Appl. Phys. Lett. **104**, 231107 (2014).
[497]K. D. Jöns, U. Rengstl, M. Oster, F. Hargart, M. Heldmaier, S. Bounouar, S. M. Ulrich, M. Jetter, and P. Michler, J. Phys. D Appl. Phys. **48**, 085101 (2015).
[498]J. W. Silverstone, D. Bonneau, J. L. O'Brien, and M. G. Thompson, IEEE J. Sel. Top. Quant. **22**, 390 (2016).
[499]U. Pfister, D. Wendland, F. Hornung, L. Engel, H. Hüging, E. Herzog, P. Vijayan, R. Joos, E. Jung, M. Jetter, S. L. Portalupi, W. H. P. Pernice, and P. Michler, npj Nanophotonics **2**, 11 (2025).
[500]P. Schnauber, A. Singh, J. Schall, S. I. Park, J. D. Song, S. Rodt, K. Srinivasan, S. Reitzenstein, and M. Davanco, Nano Lett. **19**, 7164 (2019).
[501]K. Mnaymneh, D. Dalacu, J. McKee, J. Lapointe, S. Haffouz, J. F. Weber, D. B. Northeast, P. J. Poole, G. C. Aers, and R. L. Williams, Adv. Quantum Technol. **3**, 1900021 (2020).
[502]I. E. Zadeh, A. W. Elshaari, K. D. Jöns, A. Fognini, D. Dalacu, P. J. Poole, M. E. Reimer, and V. Zwiller, Nano Lett. **16**, 2289 (2016).
[503]C. Carlson, D. Dalacu, C. Gustin, S. Haffouz, X. Wu, J. Lapointe, R. L. Williams, P. J. Poole, and S. Hughes, Phys. Rev. B **99**, 085311 (2019).
[504]S. Bauer, D. Wang, N. Hoppe, C. Nawrath, J. Fischer, N. Witz, M. Kaschel, C. Schweikert, M. Jetter, S. L. Portalupi, M. Berroth, and P. Michler, Appl. Phys. Lett. **119**, 211101 (2021).
[505]Y. Wan, C. Xiang, J. Guo, R. Koscica, M. Kennedy, J. Selvidge, Z. Zhang, L. Chang, W. Xie, D. Huang, A. C. Gossard, and J. E. Bowers, Laser Photonics Rev. **15**, 2100057 (2021).
[506]J. Kwoen, J. Lee, K. Watanabe, and Y. Arakawa, Jpn. J. Appl. Phys. **58**, SBBE07 (2019).
[507]T. Wang, H. Liu, A. Lee, F. Pozzi, and A. Seeds, Opt. Express **19**, 11381 (2011).
[508]Z. Wang, R. Yao, S. F. Preble, C.-S. Lee, L. F. Lester, and W. Guo, Appl. Phys. Lett. **107**, 261107 (2015).
[509]K. Tanabe, K. Watanabe, and Y. Arakawa, Sci. Rep. **2**, 349 (2012).
[510]X. Wang, X. Zhang, B. Chen, Y. Zhu, Y. Qin, L. Dong, J. Cai, D. Sui, J. Wu, Q. Zhang, R. Liu, Y. Huo, J. Liu, X. Ou, and J. Zhang, Nat. Mater. **24**, 1898 (2025).
[511]N. Pholsen, A. Fujita, M. Kakuda, Y. Arakawa, K. Ikeda, N. Kobayashi, Y. Ota, and S. Iwamoto, Opt. Mater. Express **15**, 290 (2025).
[512]J. Yoo, K. Lee, U. J. Yang, H. H. Song, J. H. Jang, G. H. Lee, M. S. Bootharaju, J. H. Kim, K. Kim, S. I. Park, J. D. Seo, S. Li, W. S. Yu, J. I. Kwon, M. H. Song, T. Hyeon, J. Yang, and M. K. Choi, Nat. Photonics **18**, 1105 (2024).
[513]R. Katsumi, Y. Ota, T. Tajiri, S. Iwamoto, K. Ranbir, J. P. Reithmaier, M. Benyoucef, and Y. Arakawa, Appl. Phys. Express **16**, 012004 (2023).
[514]A. Osada, Y. Ota, R. Katsumi, M. Kakuda, S. Iwamoto, and Y. Arakawa, Phys. Rev. Appl. **11**, 024071 (2019).
[515]R. Katsumi, Y. Ota, A. Osada, T. Yamaguchi, T. Tajiri, M. Kakuda, S. Iwamoto, H. Akiyama, and Y. Arakawa, APL Photonics **4**, 036105 (2019).
[516]H. Larocque, M. A. Buyukkaya, C. Errando-Herranz, C. Papon, S. Harper, M. Tao, J. Carolan, C.-M. Lee, C. J. K. Richardson, G. L. Leake, D. J. Coleman, M. L. Fanto, E. Waks, and D. Englund, Nat. Commun. **15**, 5781 (2024).
[517]S. L. Mouradian, T. Schröder, C. B. Poitras, L. Li, J. Goldstein, E. H. Chen, M. Walsh, J. Cardenas, M. L. Markham, D. J. Twitchen, M. Lipson, and D. Englund, Phys. Rev. X **5**, 031009 (2015).
[518]R. Katsumi, Y. Ota, A. Osada, T. Tajiri, T. Yamaguchi, M. Kakuda, S. Iwamoto, H. Akiyama, and Y. Arakawa, Appl. Phys. Lett. **116**, 041103 (2020).
[519]A. Chanana, H. Larocque, R. Moreira, J. Carolan, B. Guha, E. G. Melo, V. Anant, J. Song, D. Englund, D. J. Blumenthal, K. Srinivasan, and M. Davanco, Nat. Commun. **13**, 7693 (2022).
[520]J. Schuhmann, L. Lazzari, M. Morassi, A. Lemaître, I. Sagnes, G. Beaudoin, M. Amanti, F. Boeuf, F. Raineri, F. Baboux, and S. Ducci, PRX Quantum **5**, 040321 (2024).
[521]P. Holewa, A. Sakanas, U. M. Gür, P. Mrowiński, A. Huck, B.-Y. Wang, A. Musiał, K. Yvind, N. Gregersen, M. Syperek, and E. Semenova, ACS Photonics **9**, 2273 (2022).
[522]M. De Gregorio, S. Yu, D. Witt, B. Lin, M. Mitchell, L. Dusanowski, C. Schneider, L. Chrostowski, T. Huber-Loyola, S. Höfling, J. F. Young, and A. Pfenning, Adv. Quantum Technol. **7**, 2300227 (2024).
[523]M. R. Billah, M. Blaicher, T. Hoose, P.-I. Dietrich, P. Marin-Palomo, N. Lindenmann, A. Nesic, A. Hofmann, U. Troppenz, M. Moehrle, S. Randel, W. Freude, and C. Koos, Optica **5**, 876 (2018).
[524]N. Lindenmann, G. Balthasar, D. Hillerkuss, R. Schmogrow, M. Jordan, J. Leuthold, W. Freude, and C. Koos, Opt. Express **20**, 17667 (2012).
[525]F. Najafi, J. Mower, N. C. Harris, F. Bellei, A. Dane, C. Lee, X. Hu, P. Kharel, F. Marsili, S. Assefa, K. K. Berggren, and D. Englund, Nat. Commun. **6**, 5873 (2015).
[526]R. W. Heeres, L. P. Kouwenhoven, and V. Zwiller, Nat. Nanotechnol. **8**, 719 (2013).
[527]D. Sahin, A. Gaggero, T. B. Hoang, G. Frucci, F. Mattioli, R. Leoni, J. Beetz, M. Lermer, M. Kamp, S. Höfling, and A. Fiore, Opt. Express **21**, 11162 (2013).
[528]A. Gaggero, S. J. Nejad, F. Marsili, F. Mattioli, R. Leoni, D. Bitauld, D. Sahin, G. J. Hamhuis, R. Nötzel, R. Sanjines, and A. Fiore, Appl. Phys. Lett. **97**, 151108 (2010).
[529]G. Reithmaier, M. Kaniber, F. Flassig, S. Lichtmannecker, K. Müller, A. Andrejew, J. Vučković, R. Gross, and J. J. Finley, Nano Lett. **15**, 5208 (2015).
[530]E. Schmidt, K. Ilin, and M. Siegel, IEEE Trans. Appl. Supercon. **27**, 1 (2017).
[531]J. R. Clem and K. K. Berggren, Phys. Rev. B **84**, 174510 (2011).
[532]M. Anderson, T. Müller, J. Huwer, J. Skiba-Szymanska, A. B. Krysa, R. M. Stevenson, J. Heffernan, D. A. Ritchie, and A. J. Shields, npj Quantum Inf. **6**, 14 (2020).
[533]H. McCabe, S. M. Koziol, G. L. Snider, and E. P. Blair, IEEE Trans. Nanotechnol. **19**, 292 (2020).
[534]S. Gyger, K. D. Zeuner, T. Lettner, S. Bensoussan, M. Carlnäs, L. Ekemar, L. Schweickert, C. R. Hedlund, M. Hammar, T. Nilsson, J. Almlöf, S. Steinhauer, G. V. Llosera, and V. Zwiller, Appl. Phys. Lett. **121**, 194003 (2022).
[535]D. Buterakos, E. Barnes, and S. E. Economou, Phys. Rev. X **7**, 041023 (2017).
[536]C. Schimpf, M. Reindl, D. Huber, B. Lehner, S. F. Covre Da Silva, S. Manna, M. Vyvlecka, P. Walther, and A. Rastelli, Sci. Adv. **7**, eabe8905 (2021).
[537]C. L. Morrison, R. G. Pousa, F. Graffitti, Z. X. Koong, P. Barrow, N. G. Stoltz, D. Bouwmeester, J. Jeffers, D. K. L. Oi, B. D. Gerardot, and A. Fedrizzi, Nat. Commun. **14**, 3573 (2023).
[538]J. Yang, Z. Jiang, F. Benthin, J. Hanel, T. Fandrich, R. Joos, S. Bauer, S. Kolatschek, A. Hreibi, E. P. Rugeramigabo, M. Jetter, S. L. Portalupi, M. Zopf, P. Michler, S. Kück, and F. Ding, Light Sci. Appl. **13**, 150 (2024).
[539]M. Zahidy, M. T. Mikkelsen, R. Müller, B. Da Lio, M. Krehbiel, Y. Wang, N. Bart, A. D. Wieck, A. Ludwig, M. Galili, S. Forchhammer, P. Lodahl, L. K. Oxenløwe, D. Bacco, and L. Midolo, npj Quantum Inf. **10**, 2 (2024).
[540]Y. Zhang, X. Ding, Y. Li, L. Zhang, Y.-P. Guo, G.-Q. Wang, Z. Ning, M.-C. Xu, R.-Z. Liu, J.-Y. Zhao, G.-Y. Zou, H. Wang, Y. Cao, Y.-M. He, C.-Z. Peng, Y.-H. Huo, S.-K. Liao, C.-Y. Lu, F. Xu, and J.-W. Pan, Phys. Rev. Lett. **134**, 210801 (2025).

[541]H. Wang, J. Qin, X. Ding, M.-C. Chen, S. Chen, X. You, Y.-M. He, X. Jiang, L. You, Z. Wang, C. Schneider, J. J. Renema, S. Höfling, C.-Y. Lu, and J.-W. Pan, Phys. Rev. Lett. **123**, 250503 (2019).
[542]X. Xu, I. Toft, R. T. Phillips, J. Mar, K. Hammura, and D. A. Williams, Appl. Phys. Lett. **90**, 061103 (2007).
[543]X. Xu, F. Brossard, K. Hammura, D. A. Williams, B. Alloing, L. H. Li, and A. Fiore, Appl. Phys. Lett. **93**, 021124 (2008).
[544]W. B. Jeon, J. S. Moon, K. Kim, Y. Ko, C. J. K. Richardson, E. Waks, and J. Kim, Adv. Quantum Technol. **5**, 2200022 (2022).
[545]C.-M. Lee, M. A. Buyukkaya, S. Aghaeimeibodi, A. Karasahin, C. J. K. Richardson, and E. Waks, Appl. Phys. Lett. **114**, 171101 (2019).
[546]C. Qian, M. Troue, J. Figueiredo, P. Soubelet, V. Villafañe, J. Beierlein, S. Klembt, A. V. Stier, S. Höfling, A. W. Holleitner, and J. J. Finley, Sci. Adv. **10**, eadk6359 (2024).
[547]Z. Dai, L. Liu, and Z. Zhang, Adv. Mater. **31**, 1805417 (2019).
[548]R. Peng, A. Ripin, Y. Ye, J. Zhu, C. Wu, S. Lee, H. Li, T. Taniguchi, K. Watanabe, T. Cao, X. Xu, and M. Li, Nat. Commun. **13**, 1334 (2022).
[549]X. Nie, X. Wu, Y. Wang, S. Ban, Z. Lei, J. Yi, Y. Liu, and Y. Liu, Nanoscale Horiz. **8**, 158 (2023).
[550]C. Qian, V. Villafañe, M. M. Petrić, P. Soubelet, A. V. Stier, and J. J. Finley, Phys. Rev. Lett. **130**, 126901 (2023).
[551]Y. Yuan, C. Qian, S. Sun, Y. Lei, J. Yang, L. Yang, B. Fu, S. Yan, R. Zhu, H. Li, X. Chen, Z. Zuo, B.-B. Li, Y.-F. Xiao, H. Zhong, C. Wang, K. Jin, Q. Gong, and X. Xu, J. Phys. Chem. Lett. **16**, 1095 (2025).
[552]C. Qian, V. Villafañe, P. Soubelet, A. Hötger, T. Taniguchi, K. Watanabe, N. P. Wilson, A. V. Stier, A. W. Holleitner, and J. J. Finley, Phys. Rev. Lett. **128**, 237403 (2022).